Order Number 9432346

Flow of a sediment layer on an inclined plate

Kapoor, Bir, Ph.D.

City University of New York, 1994

U·M·I
300 N. Zeeb Rd.
Ann Arbor, MI 48106

FLOW OF A SEDIMENT LAYER ON AN INCLINED PLATE

by

BIR KAPOOR

A dissertation submitted to the Graduate Faculty in
Engineering in partial fulfillment of the
requirements for the degree of Doctor of Philosophy,
The City University of New York

1994

This manuscript has been read and accepted by the Graduate Faculty in Engineering in satisfaction of the dissertation requirement for the degree of Doctor of Philosophy.

4/5/94
Date

Professor Andreas Acrivos
Chair of Examining Committee

4/5/94
Date

Dean Gerard Lowen
Executive Officer

Professor Yiannis Andreopoulos

Dr. Eric Herbolzheimer

Professor Charles Maldarelli

Professor Herbert Weinstein

Supervisory Committee

The City University of New York

Abstract

FLOW OF A SEDIMENT LAYER ON AN INCLINED PLANE

by

Bir Kapoor

Advisor: Professor Andreas Acrivos

The flow of a sediment layer that forms on an inclined plate as a consequence of the steady sedimentation of spherical particles was investigated theoretically as well as experimentally. The theoretical analysis was based on the model proposed by Nir & Acrivos (1990), modified to include shear induced diffusion due to gradients in the shear stress as well as the effects of slip at the wall due to the finite size of the particles. The resulting set of partial differential equations, which is amenable to a similarity type solution both near the leading edge as well as far downstream, was solved numerically using a finite difference scheme thereby yielding theoretical predictions for the particle concentration and velocity profiles, plus the local sediment layer thickness, all along the plate. A new experimental technique based on Laser Doppler Anemometry was developed and was used to measure the particle velocity profile in the highly concentrated sediment layer as well as the corresponding slip coefficient adjacent to a wall. The thickness profile of the sediment layer was also measured experimentally by means of video imaging. It was found that the experimental results thus obtained for the particle velocity profile and for the local sediment layer thickness were in very good agreement with the corresponding theoretical predictions especially considering that the latter did not make use of any adjustable parameters.

Dedicated

to

my parents.

Acknowledgements

I wish to express a deep sense of gratitude to Professor Andreas Acrivos whose teaching, guidance and lucid lectures on fluid mechanics have been of immeasurable value to this dissertation and, more importantly, to my education. Furthermore, I appreciate his efforts in helping me develop skills in the various aspects of research, especially in the written parts of my work.

I am grateful to Professor Yiannis Andreopolous and Bob Suhoke Jr. for the loan of various equipment including the Laser Doppler Anemometer used in this study. I am also indebted to Bob Suhoke Jr. for providing not only much needed technical expertise during the experimental part of this study, but also support as a friend throughout this work. I would like to thank Dr. Eric Herbolzheimer for acting as an external examiner and providing valuable comments during the course of this work.

Special thanks are due to Ivan and Xu for machining the various parts of the experimental setup. I would also like to thank the members (past and present) of the Levich Institute for providing a pleasant and supportive atmosphere. I am especially grateful to Mary Wright for providing administrative support in setting up the experiments.

There are of course several friends who contributed directly or indirectly in making my sojourn at New York City a memorable one and I am grateful to them all. In reference to this work, I would like to thank: Anant, Anurag, Fan, Kai, Nicky,

Sadhan, Said, Sanjeev and Tammy. Finally, I would like to thank my parents for their love, support and sacrifice.

This research was supported in part by the National Science Foundation under grants CTS-8896170 and CTS-9012546 and by the Department of Energy under grant DE-FG02-90-ER14139.

Contents

List of Tables

List of Figures

Chapter 1

Introduction

The separation of solid particles from liquids by means of gravity settling constitutes an important physical step in many chemical industries. This process is often slow and requires large vessels especially when the particles are small and the fluid is viscous. It has been shown, however, that the settling process can be enhanced by employing vessels with inclined walls which, for an equivalent rate of production of sediment or of clear fluid, typically occupy considerably less space than their vertical counterparts. These settlers, often called super settlers, consist of a series of closely spaced parallel plates. Using kinematic arguments, a simple expression for the settling rate in such vessels was derived by Ponder (1925) and, independently, by Nakamura and Kuroda (1937) and is referred to as the PNK theory.

According to this theory, the instantaneous settling rate of a monodisperse suspension for the parallel plate geometry shown in figure 1.1 takes the following form

$$S(t) = u_0 \left\{ b \sec\left(\frac{\pi}{2} - \theta\right) + H(t) \tan\left(\frac{\pi}{2} - \theta\right) \right\} \tag{1.1}$$

where $S(t)$ is the volumetric flow rate of production of clear fluid per unit depth in the third direction, u_0 is the vertical settling velocity of the particles in the suspension, b is spacing between the plates, θ is the angle of inclination relative to the horizontal and H is the height of the suspension in the vessel at any time t. Qualitatively,

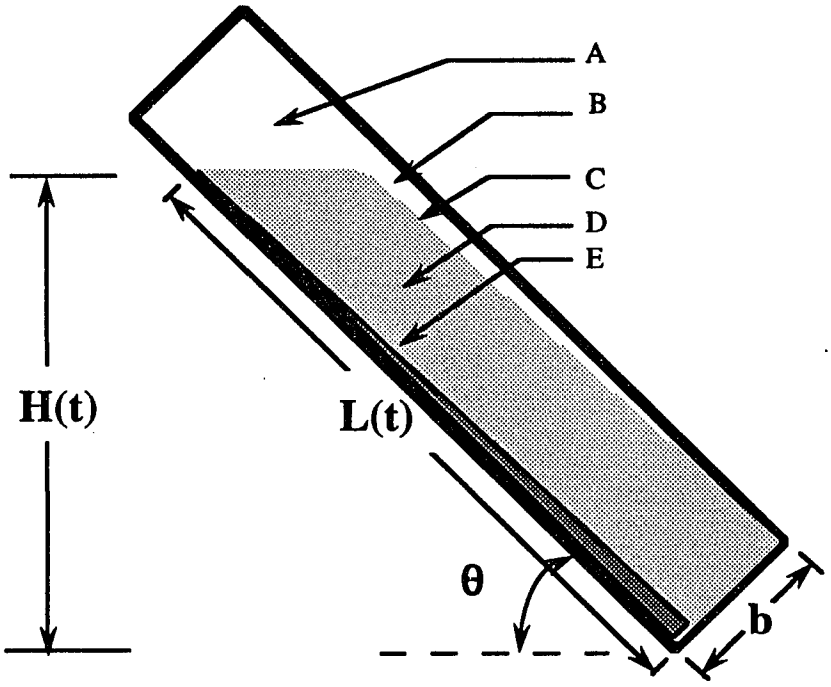

A: Clear fluid reservoir
B: Clear fluid layer
C: Suspension-clear fluid interface
D: Suspension
E: Sediment layer

Figure 1.1: A schematic description of an inclined settler

the enhancement in the settling rate can then be simply explained by the fact that, whereas in a vertical settler, particles must travel a distance of $O(H)$ to be removed, this distance becomes $O(b)$ when the plates are inclined. Thus, for a given angle of inclination, the enhancement to the settling rate is linear in the aspect ratio $O(H/b)$ and, therefore, can be made arbitrarily large in principle by decreasing the spacing between the plates.

The different regions in the flow field of a typical parallel plate inclined settler are illustrated in figure 1.1. Region (B) depicts the clear fluid layer formed underneath the downward facing surface which, under the action of buoyancy, is convected rapidly towards the top of the vessel into the clear fluid reservoir (A). The interface (C) separates the clear fluid layer from the adjoining suspension region (D), in which the particle concentration remains constant throughout the sedimentation process. In addition, since both the clear fluid and the particles are incompressible, the production of clarified fluid must be accompanied by the removal of an equivalent amount of particles from the suspension. This occurs along the upward facing surface, where a thin layer of sediment, shown as region (E) in figure 1.1, is formed which flows down the inclined plate.

The first theoretical analysis of this phenomenon using the principles of continuum mechanics was presented by Hill *et al.* (1977), for the case of a dilute suspension of spherical particles. Since then a number of studies (e.g. Acrivos & Herbolzheimer 1979; Herbolzheimer & Acrivos 1981; Schneider 1982; Rubinstein 1980; Probstein *et al.* 1981; Leung & Probstein 1983; Shaqfeh and Acrivos 1986) were performed which examined theoretically the flow fields within the various regions of the inclined settlers. In particular, most of these investigators developed analytic expressions for the velocity profiles within the clear fluid layer underneath the downward facing wall and within the adjoining suspension for a wide range of parameters, and showed that, as long as the interface between the particle free layer and the suspension

remains stable, the augmentation in the settling rate is the same as that predicted by the PNK theory. Under certain conditions, however, the buoyancy driven flow within the clear fluid region (B) has been observed to be unstable and to result in the formation of waves at the suspension-clear fluid interface, which grow as they travel up the vessel and often break before reaching the clear fluid reservoir (A). This phenomenon of wave breakup and the resulting remixing of the adjoining suspension with the clarified fluid reduces the efficiency of the inclined settler because the rate of production of clarified fluid falls below the value predicted by the PNK theory. This wave formation was first investigated by Herbolzheimer (1983) who, by means of a linear stability analysis, examined the response to small disturbances of the base-state velocity profile derived earlier by Herbolzheimer & Acrivos (1979) for the case of "low aspect ratio" settlers and in the absence of inertia effects. Although this study led to the conclusion that the flow field in such settlers is always unstable, the wave growth rate under normal operating condition was predicted to be small. Therefore, when the inertia terms in the base flow equations are of secondary importance, the existence of such waves has little effect on the the efficiency of inclined settlers. In subsequent publications, Shaqfeh and Acrivos (1986) extended the base-flow model of Herbolzheimer and Acrivos to include the effects of inertia and then performed the corresponding linear stability analysis (Shaqfeh and Acrivos,1987) for the case of dilute suspensions. These authors showed that the presence of inertia exerts a strong destabilizing influence.

Another important feature of inclined settlers involves the formation and flow of the sediment layer on the upward facing surface, which can play a significant role in their operation especially when, θ, the angle of inclination, is small or when the thickness of the sediment layer is comparable to the spacing between the walls. The latter may occur for vessels which are long and narrow. Until recently, however, this facet of the problem did not receive much attention the only exception being the

two studies by Probstein *et al.* (1981) and by Leung & Probstein (1983), who treated the sediment as an effective Newtonian fluid of a priori specified composition. Thus, these authors viewed the domain within the settler as consisting of three stratified layers i.e. a clear fluid, the bulk of the suspension and the concentrated sediment layer flowing along the upward facing plate. Unfortunately, since no theory was available at that time for determining the particle concentration within the flowing concentrated sediment, such a model required the use of an adjustable parameter.

Recently, this limitation was overcome by Nir and Acrivos (1990) who, using again a continuum description, proposed a model to describe the flow of the sediment layer that forms as a result of steady sedimentation on an inclined plate. This also corresponds to the flow which develops on the upward facing surface of a "low aspect ratio" inclined settler. The key feature of this model, which does not require any adjustable parameters, is the introduction of an equation for the particle concentration distribution which involves a balance between particle convection due to the bulk flow, gravitational sedimentation, and shear induced particle migration. The latter, which arises as a consequence of irreversible interparticle interactions, has been found recently to play a major role in creating the nonuniform particle concentration distributions observed experimentally in suspensions undergoing shear (Leighton & Acrivos 1986, 1987; Phillips *et al.* 1992; Koh *et al.* 1993) as well as in the corresponding computer simulation studies (Brady and Bossis 1988; Durlofsky and Brady 1989). Thus, according to Nir and Acrivos (1990), the nonuniform particle concentration resulting from this particle migration within the flowing sediment layer, influences the local bulk properties such as the effective viscosity and density of the suspension which in turn affect the bulk flow within the sediment. This particle convective diffusion equation together with the momentum balance leads then to a coupled system of equations, the solution of which determines the bulk velocity and particle concentration profiles within the sediment layer and within the adjoining

suspension. In addition, by invoking a standard lubrication approximation, Nir and Acrivos (1990) first simplified these equations and then showed that the resulting system was amenable to a similarity solution. A key feature of this model is that the particle concentration suffers a jump across an interface separating the suspension from a thin highly concentrated sediment layer, of finite thickness δ, flowing along the inclined plate. An additional conclusion resulting from this analysis was that the highest particle volume fraction within the sediment layer for a given angle of inclination will approach the maximum possible value ϕ_m, above which the sediment is unable to flow, when the particle volume fraction in the sedimenting suspension (ϕ_s) is either very high or very low. Consequently, a large sediment layer thickness (δ) was predicted under these conditions. But since it is natural to expect that δ should vanish as $\phi_s \rightarrow 0$, the theoretically predicted large values of δ for dilute sedimenting suspensions is clearly very puzzling. As was pointed out by these authors this may well reflect the limitations of their model.

It is clear, therefore, that the theoretical predictions referred to above had to be tested experimentally. To this end, several qualitative experiments were performed in a "low aspect ratio" inclined settler, which did not show the predicted increase in δ with decreasing values of ϕ_s for dilute sedimenting suspensions. It was noted, however, that adjacent to the inclined plate, particles did not adhere to the surface as was assumed by Nir and Acrivos (1990) who, in their analysis imposed the no slip boundary condition at the plate, but rather were observed to move with a velocity comparable to that along the sediment-suspension interface. This observation is consistent with the well accepted notion regarding the existence of a slip velocity in flowing concentrated suspensions which arises from the fact that, next to a solid surface, there exists a thin film of liquid having a thickness comparable to the particle diameter within which the particles may roll. Thus, in order to effect a meaningful comparison between the theoretical predictions and the experimental results, it was

felt desirable to modify the analysis of Nir and Acrivos (1990) by replacing the no-slip boundary condition with one involving a slip velocity proportional to the local shear rate at the inclined plate. Also incorporated in the modified analysis was the addition of a term in the expression for the shear induced particle diffusion which accounts for the migration of particles due to a shear stress gradient. This is in addition to the term contributing to the particle diffusive flux due to a concentration gradient already accounted for by Nir and Acrivos (1990) in their analysis. A similarity solution to the governing equations was then constructed the validity of which is, however, restricted to a region close to the leading edge of the sediment layer. The details of the modified theory along with the derivation of this similarity solution are presented in chapter two, which also contains some typical numerical results obtained using a theoretically estimated slip coefficient. In addition to this leading edge solution, chapter two also describes briefly the no-slip solution of Nir & Acrivos (1990), modified to account for the shear induced particle diffusion to gradients in the shear stress, which essentially represents the asymptotic solution far downstream. As will be seen, the theoretical results for low values of the sedimenting suspension concentration ϕ_s are greatly affected by the introduction of a slip velocity and by diffusion due to a shear stress gradient in that, as expected on physical grounds and in contrast to the result arrived at by Nir and Acrivos (1990), δ is now found to vanish as $\phi_s \rightarrow 0$.

Since the similarity solutions presented in chapter two are valid only in the region close to the leading edge or far downstream, it was felt necessary to construct a solution valid over the entire length of the plate before a meaningful comparison between the experimental results and the theoretical predictions could be made. The governing equations presented in chapter two were therefore solved numerically by a finite difference technique the details of which, along with some typical results, are given in chapter three. As will be seen in this chapter, the exact solution thus obtained, which was constrained to conform to the slip similarity solution in the

immediate neighborhood of the leading edge, approaches asymptotically the no-slip similarity solution far downstream.

The reliability of the modified theory can be tested experimentally by measuring certain key features of the flow, e.g. the local thickness of the sediment layer plus the corresponding particle velocity and concentration profiles. Of these, the sediment thickness δ is of course relatively easy to determine either directly using a cathetometer or via a video imaging technique. On the other hand, due to the small layer thicknesses and the high particle volume fractions usually encountered within the sediment, particle velocity and concentration measurements are extremely difficult to perform. Nevertheless, several successful attempts (e.g. Karnis *et al.* 1966; McMahon & Parker 1975; Kowalewski 1980; Koh *et al.* 1993) have been made in the past to develop convenient techniques for determining the velocity profiles in flowing concentrated suspensions, of which, as will be discussed briefly in chapter four, the method described by Koh *et al.*(1993) was found to be most suitable for present purposes. These investigators have shown recently that the well known Laser Doppler Anemometry (LDA) technique can be easily adapted to measure the velocity and concentration profiles in flowing suspensions by matching the refractive indices of the particles with that of the suspending fluid. Although the proposed measurement system yields a relatively good spatial resolution and is relatively easy to implement, its applicability to highly concentrated suspensions which are usually encountered in sediment layers had not been demonstrated. It will be presently shown, however, that, with a few modifications, this technique can be extended to measure the velocity of particles even for particle concentrations close to the maximum. Unfortunately, this technique could not be extended to measure the particle concentrations under the present conditions, due to attenuation of the signal at these concentrations. The details of the experimental set up and of the technique that was used are presented in the fourth chapter. In addition, this new method was also employed to estimate

the slip coefficient by measuring the particle velocity within a sheared concentrated suspension in a narrow gap Couette device. The details of this experimental setup along with the results are presented in appendix A

Finally, in chapter five, the experimentally obtained sediment layer thicknesses and velocity profiles will be compared with the corresponding theoretical predictions presented in chapter three. It will be seen that there is surprisingly close agreement between the experiments and the theory especially considering that the latter did not entail the use of adjustable parameters. Unfortunately, a method for measuring the particle concentration under the present conditions is as yet unavailable and, therefore, the theoretically predicted particle concentration profiles could not be tested during the course of this study.

Chapter 2

Formulation

2.1 Basic Equations

To begin with, the suspension is modeled as an effective Newtonian fluid with effective physical properties which, relative to the corresponding properties of the suspending liquid, are functions only of the local volume fraction of the particles. Thus, the density is expressed as

$$\tilde{\rho}(\phi) = \tilde{\rho}_f \gamma(\phi) \tag{2.1}$$

and the viscosity as

$$\tilde{\mu}(\phi) = \tilde{\mu}_f \lambda(\phi) \tag{2.2}$$

where ϕ denotes the local volume fraction of the particles, the tilde indicates that the variable in question has dimensions and the subscript f refers to the corresponding property of the clear fluid. Consequently, the equations of motion and of continuity take the familiar form

$$\tilde{\rho}(\phi)\underline{\tilde{u}} \cdot \tilde{\nabla}\underline{\tilde{u}} = \tilde{\nabla} \cdot \underline{\tilde{\sigma}} + \left(\tilde{\rho}(\phi) - \tilde{\rho}_f\right)\underline{\tilde{g}} \qquad \text{and} \qquad \tilde{\nabla} \cdot \underline{\tilde{u}} = 0 \tag{2.3}$$

$$\text{with } \underline{\underline{\tilde{\sigma}}} = -\tilde{p}\underline{\underline{I}} + \tilde{\mu}(\phi)\left(\tilde{\nabla}\underline{\tilde{u}} + \tilde{\nabla}\underline{\tilde{u}}^{\dagger}\right) \tag{2.4}$$

where $\underline{\tilde{u}}$, $\underline{\underline{\tilde{\sigma}}}$ and $\tilde{p}$ are the bulk velocity, stress and the pressure fields respectively. The last term in equation (2.3) denotes the buoyancy body force which arises due to the difference in the density of the particles and that of the fluid. In addition, the presence of shear in a concentrated suspension induces a migration of particles within the suspension, which along with the sedimentation flux and the bulk flow leads to a non-uniform distribution of particles within the flowing sediment. To determine this particle concentration it is necessary, however, to examine the equation for the steady state particle balance

$$\underline{\tilde{u}} \cdot \tilde{\nabla}\phi = -\left(\tilde{\nabla} \cdot \underline{\tilde{J}}\right) \tag{2.5}$$

$$\text{with} \qquad \underline{\tilde{J}} = \underline{\tilde{N}_g} + \underline{\tilde{N}_d} \tag{2.6}$$

where $\underline{\tilde{N}_g}$ and $\underline{\tilde{N}_d}$ denote, respectively, the flux of particles due to gravity settling and that due to shear induced diffusion. For the case of a monodisperse suspension of heavy spheres of radius $\tilde{a}$, the former takes on the familiar form

$$\underline{\tilde{N}_g} = \frac{2}{9}\phi\tilde{a}^2\frac{(\tilde{\rho}_s - \tilde{\rho}_f)}{\tilde{\mu}_f}f(\phi)\underline{\tilde{g}} = \tilde{u}_t\phi f(\phi)\underline{e_g} \tag{2.7}$$

where $\tilde{u}_t$ is the Stokes sedimentation speed of a single sphere of density $\tilde{\rho}_s$ in the clear fluid, $\underline{e_g}$ denotes a unit vector along the direction of gravity and $f(\phi)$ is the so called hindrance function which accounts for the effect of the other particles on the sedimentation velocity.

In general, this set of equations would be expected to model accurately the flow of concentrated suspensions, as long as the length scale of the flow is much

larger than the particle size in order to conform to the requirements of the continuum description. Nevertheless, due to the lack of an appropriate model for the shear induced diffusion in two dimensions, this approach has been applied to-date only to flows which were either unidirectional or quasi-unidirectional (Leighton and Acrivos,1986; Schaflinger,Acrivos and Zhang, 1990). Specifically, on the basis of such a model, Leighton and Acrivos (1986) studied the resuspension of particles in a plate of constant shear, while Schaflinger, Acrivos and Zhang (1990) considered the corresponding case of a fully-developed stably stratified flow in a channel and the gravity driven film flow of a suspension of settling particles. Also, as mentioned earlier, Nir and Acrivos (1990) examined, on the basis of these equations, the flow of a sediment layer that forms on the top side of an inclined plate which is placed within a suspension of sedimenting particles (c.f. figure 1.1). Although, in general, the latter is a two dimensional problem, the fact that the flowing sediment layer is very thin relative to its length allows one to simplify the equations by applying the lubrication approximation and thereby treat the system as quasi-one dimensional. In view of its relevance to the present work, the analysis presented by Nir and Acrivos (1990) will now be discussed briefly in the following section.

2.2 Sedimentation on an Inclined Plate

Consider a simple two dimensional system shown in figure 2.1, consisting of a surface of length $\tilde{L}$ and arbitrary width, inclined at an angle θ from the horizontal and placed in a infinite suspension of heavy spheres of radius $\tilde{a}$. The volume fraction of the particles far from the plate, also referred to as the feed particle concentration, will be denoted by ϕ_*. For this system, a thin layer of a flowing sediment has been observed to form on the inclined plate with most of the flow occurring close to the wall. Thus, the standard lubrication approximation can be invoked according to which the velocity component along the inclined plate is much larger than that perpendicular

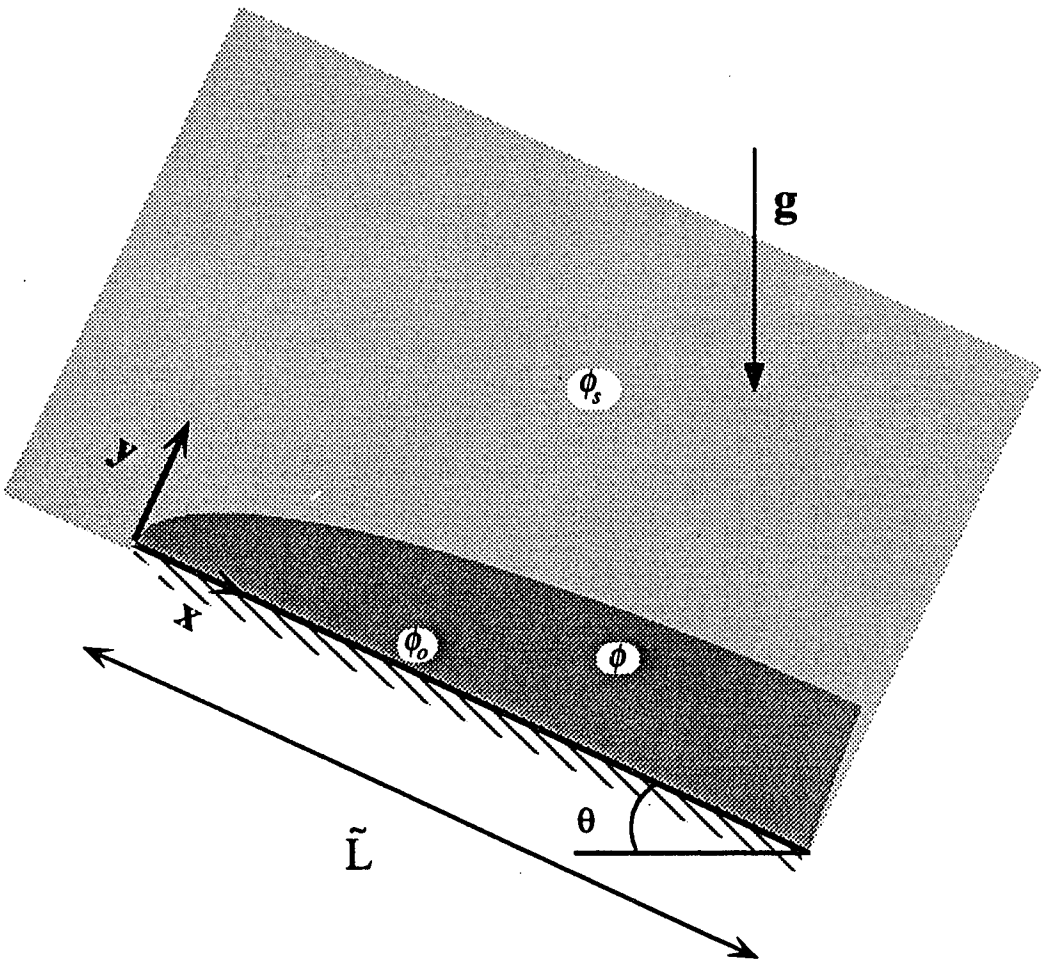

Figure 2.1: A schematic description of sediment flow on an inclined plate

to it and, also, that any variations across the sediment layer are substantially greater than those along the longitudinal direction. In addition, any changes normal to the x-y plate shown in figure 2.1 are neglected. With these approximations, the momentum equation (2.3) along the x direction, when nondimensionalized using $\tilde{L}$ and $\tilde{u}_t$ as the characteristic length and velocity scales of the flow, reduces in the vicinity of the plate to

$$\frac{\partial}{\partial \mathcal{Y}}\left[\lambda(\phi)\frac{\partial u_x}{\partial \mathcal{Y}}\right] + \frac{9}{2}\epsilon^{-2}(\phi - \phi_*)\sin\theta = R\gamma(\phi)\left(u_x\frac{\partial u_x}{\partial \mathcal{X}} + u_y\frac{\partial u_x}{\partial \mathcal{Y}}\right) \tag{2.8}$$

$$\frac{\partial u_x}{\partial \mathcal{X}} + \frac{\partial u_y}{\partial \mathcal{Y}} = 0 \tag{2.9}$$

where $R = \tilde{\rho}_f \tilde{u}_t \tilde{L}/\tilde{\mu}_f$ is the macroscopic Reynolds number and

$$\epsilon^2 = \frac{\tilde{a}^2}{\tilde{L}^2} = \frac{9\tilde{\mu}_f \tilde{u}_t}{2\tilde{g}\tilde{L}^2(\tilde{\rho}_* - \tilde{\rho}_f)} \tag{2.10}$$

Clearly, ϵ is very small in most practical cases and hence, as can be seen from equation (2.8), a large buoyancy force is expected to exist in the region close to the wall which is driving the flow and which must be balanced in general by viscous and inertial forces. In addition, wherever this lubrication type approximation applies, the term $\frac{\partial u_x}{\partial \mathcal{Y}}$ becomes the dominant component in the velocity gradient tensor and thus, the expression for the diffusive flux proposed by Leighton and Acrivos (1986a), which accounts for shear-induced diffusion due to both concentration and shear stress gradients, reduces, in terms of dimensionless variables, to

$$\underline{N_d} = -\left[\beta(\phi)\frac{\partial \phi}{\partial \mathcal{Y}} + \frac{\alpha(\phi)}{\lambda(\phi)\,|\frac{\partial u_x}{\partial \mathcal{Y}}|}\frac{\partial}{\partial \mathcal{Y}}\left(\lambda(\phi)\,|\frac{\partial u_x}{\partial \mathcal{Y}}|\right)\right]\epsilon^2\,|\frac{\partial u_x}{\partial \mathcal{Y}}|\;\underline{e_y} \tag{2.11}$$

where $\underline{e_y}$ denotes the unit vector along the y-direction. The explicit form of α and β used in the present analysis, which are assumed to be functions of ϕ only, will be discussed in section 2.3. Hence, in view of the above expression for the diffusive flux

and (2.7) for the sedimentation flux, the particle balance equation (2.5) reduces, in terms of dimensionless variables, to

$$u_x\frac{\partial\phi}{\partial\mathcal{X}}+u_y\frac{\partial\phi}{\partial\mathcal{Y}}-\frac{\partial}{\partial\mathcal{Y}}\{f(\phi)\phi\cos\theta\}=\epsilon^2\frac{\partial}{\partial\mathcal{Y}}\left(\beta(\phi)\frac{\partial u_x}{\partial\mathcal{Y}}\frac{\partial\phi}{\partial\mathcal{Y}}+\frac{\alpha(\phi)}{\lambda(\phi)}\frac{\partial}{\partial\mathcal{Y}}\left(\lambda(\phi)\frac{\partial u_x}{\partial\mathcal{Y}}\right)\right) \tag{2.12}$$

where again the boundary layer or lubrication type approximation has been invoked. Equations (2.8), (2.9) and (2.12) were analyzed by Nir and Acrivos (1990) for the case $\alpha\equiv 0$, i.e. in the absence of shear-induced diffusion due to gradients in the shear stress, subject to the no slip boundary condition at $\mathcal{Y}=0$, i.e.

$$u_x,\ u_y=0 \tag{2.13}$$

and the condition of zero particle flux

$$\epsilon^2\left[\beta(\phi)\frac{\partial u_x}{\partial\mathcal{Y}}\frac{\partial\phi}{\partial\mathcal{Y}}+\frac{\alpha(\phi)}{\lambda(\phi)}\frac{\partial}{\partial\mathcal{Y}}\left(\lambda(\phi)\frac{\partial u_x}{\partial\mathcal{Y}}\right)\right]+\phi f(\phi)\cos\theta=0 \tag{2.14}$$

on the inclined plate. Note that (2.14) reflects the fact that, at $\mathcal{Y}=0$, the settling flux of the particles must be balanced by a corresponding shear induced diffusive flux if the net particle flux into the wall is to vanish. Thus, according to this model, the existence of the shear induced particle diffusion prevents the concentration of particles at the wall from reaching its maximum possible value and thereby plays a crucial role in maintaining the flow of the sediment layer.

Clearly, within this sediment layer, the diffusion and convective terms in the particle balance equation are of comparable magnitude while, in the vicinity of the inclined plate, the viscous forces are important and must balance the driving force of the flow i.e. the buoyancy term in equation (2.8). Then, as shown by Nir and Acrivos (1990), this leads to the transformation

$$Y=\epsilon^{-2/3}\mathcal{Y},\ u=\epsilon^{2/3}u_x,\ v=u_y,\ X=\mathcal{X}\ \text{with}\ \epsilon=\tilde{a}/\tilde{L}\ll 1 \tag{2.15}$$

according to which the thickness of the viscous layer close to the inclined plate relative to its length $\tilde{L}$ is of order $\epsilon^{2/3}$. Since, the latter is very small, the use of the lubrication approximation in reducing (2.3) and (2.5) into (2.8) and (2.11) is justified. In addition, though, since the thickness of this viscous layer relative to the particle radius $\tilde{a}$ is of order $\epsilon^{-1/3}$, and therefore very large, one of the main conditions for the validity of the continuum approximation throughout the present formulation is satisfied as $\epsilon \to 0$. Finally, when $R \approx O(1)$, the inertial terms in (2.8) are of order $R\epsilon^{2/3}$ relative to the viscous and buoyancy terms and may therefore be neglected to leading order. Thus, the momentum, continuity and particle balance equations become, respectively, in terms of the transformed variables of (2.15)

$$\frac{\partial}{\partial Y}\left[\lambda(\phi)\frac{\partial u}{\partial Y}\right] + \frac{9}{2}(\phi - \phi_*)\sin\theta = O\left(R\epsilon^{2/3}\right), \quad \frac{\partial u}{\partial X} + \frac{\partial v}{\partial Y} = 0 \tag{2.16}$$

and

$$\begin{aligned} u\frac{\partial \phi}{\partial X} \; + \; & v\frac{\partial \phi}{\partial Y} - \cos\theta \frac{\partial \phi}{\partial Y}\frac{d}{d\phi}\left[\phi f(\phi)\right] = \\ & \beta(\phi)\frac{\partial u}{\partial Y}\frac{\partial^2 \phi}{\partial Y^2} + \frac{\partial \phi}{\partial Y}\left[\left\{\lambda(\phi)\frac{\partial u}{\partial Y}\frac{\partial \phi}{\partial Y}\frac{d}{d\phi}\left(\frac{\beta(\phi)}{\lambda(\phi)}\right)\right\}\right. \\ - \; & \left.\frac{9}{2}\sin\theta\left\{\frac{\beta(\phi)}{\lambda(\phi)})(\phi - \phi_*) + \frac{d}{d\phi}\left(\frac{\alpha(\phi)}{\lambda(\phi)}(\phi - \phi_*)\right)\right\}\right] + O\left(\epsilon^{2/3}\right) \end{aligned} \tag{2.17}$$

where, in arriving at (2.17) from (2.12), use has been made of (2.16). Finally, equation (2.14) becomes

$$\beta(\phi)\frac{\partial u}{\partial Y}\frac{\partial \phi}{\partial Y} - \frac{9}{2}\frac{\alpha(\phi)}{\lambda(\phi)}(\phi - \phi_*)\sin\theta + \phi f(\phi)\cos\theta = 0 \quad \text{at} \quad Y = 0 \tag{2.18}$$

where again use has been made of (2.16).

Unlike the previous work of Nir and Acrivos (1990) which, as noted earlier, imposed the no-slip boundary condition and was also restricted to the case $\alpha \equiv 0$, the analysis to be presented below will examine the consequences of having both a slip

velocity at the wall, proportional to the local rate of shear, as well as $\alpha \neq 0$. Hence the boundary condition (2.13) will be replaced by

$$u = \zeta \left(\frac{\partial u}{\partial Y} \right)_{Y=0} \quad \text{and} \quad v = 0 \quad \text{at} \quad Y = 0 \tag{2.19}$$

where ζ is the slip coefficient. In general, the latter will depend on the microstructure of the suspension close to the wall; however, to a first approximation it will be taken to be a function only of the particle volume fraction at the wall and of the size of the particles. Recall that, as was mentioned in the introduction, the existence of an effective slip velocity is due to the fact that, since the particles are of finite size, the continuum approximation fails within an order $\tilde{a}$ distance from the wall. Clearly, in the limit $\tilde{a} \rightarrow 0$, the slip coefficient should vanish since, in that case, the continuum hypothesis will be satisfied everywhere and the no slip condition will apply at the wall.

To complete the mathematical formulation of the problem, it is necessary to specify the remaining boundary conditions far from the plate. Before this can be done, however, it is important to take into account the fact that the boundary layer along the inclined plate can actually be viewed as consisting of two overlapping sublayers. Specifically, as pointed out above, in the region adjacent to the inclined plate, termed the viscous sublayer, the viscous terms in (2.8) balance the force due to buoyancy and inertia effects are negligible to first order. Consequently, within this domain, the appropriate scaling transformations are as shown in (2.15), and the momentum and particle balance equations reduce to (2.16) & (2.17) respectively. Far away from the plate, however, the particle concentration approaches ϕ_* and, since the buoyancy term in the momentum balance equation will therefore vanish, the viscous forces in (2.8) can only be balanced by the inertial terms. Hence, the thickness of this inertial sublayer relative to $\tilde{L}$ is of order $(Ru_x)^{-1/2}$ or $O(\epsilon^{1/3}R^{-1/2})$ since continuity of u_x across both layers requires that $u_x \sim O(\epsilon^{-2/3})$ in view of (2.15). The ratio of the

two length scales - viscous to inertial - is therefore $O(R^{1/2}\epsilon^{1/3})$, so that the matching condition between the two solutions in their region of overlap reduces to

$$\frac{\partial u}{\partial Y} = O\left(R^{1/2}\epsilon^{1/3}\right) \to 0 \quad \text{for} \quad \epsilon \to 0 \quad \text{and} \quad R \sim O(1) \tag{2.20}$$

as the edge of the viscous layer is approached from below. Consequently, the longitudinal velocity component would be expected to increase monotonically from the wall to its maximum value at the edge of the viscous sublayer.

It was also reported by Nir and Acrivos (1990) that the set of equations which apply within the viscous sublayer do not have a solution if the particle volume fraction is set equal to ϕ_* at the edge of this layer. As a result, Nir and Acrivos (1990) were led to conclude that the particle concentration would change discontinuously across the interface separating the concentrated sediment from the bulk of the suspension and that the entire variation of the particle volume fraction would be confined within a viscous layer of finite thickness, beyond which the buoyancy term in (2.16) would vanish. The boundary condition at the interface follows then from the requirement that the particle flux be continuous across it. Therefore, if the edge of the viscous sublayer is denoted by $Y = \delta(X)$, and taking into account that diffusion due to concentration gradients vanishes in view of (2.11) and (2.20), this condition becomes

$$\left[-u_\delta \frac{d\delta}{dX} + v_\delta - f(\phi_\delta)\cos\theta\right]\phi_\delta + \frac{9\alpha(\phi_\delta)}{2\lambda(\phi_\delta)}(\phi_\delta - \phi_*)\sin\theta = \left[-u_\delta \frac{d\delta}{dX} + v_\delta - f(\phi_*)\cos\theta\right]\phi_* \tag{2.21}$$

where ϕ_δ denotes the particle concentration as the interface is approached from below and u_δ & v_δ are the corresponding velocity components evaluated at $Y = \delta(X)$. Although (2.21) is obviously satisfied when $\phi_\delta = \phi_*$, it was mentioned earlier that the governing equations within the viscous layer subject to this boundary condition do not have a solution for any choice of δ and therefore, some additional physical

information or another boundary condition is needed if both ϕ_δ and $\delta(X)$ are to be determined. This is provided by the fact that (2.17) becomes singular at the edge of the viscous layer since $(\partial u/\partial Y)$, which is also proportional to the coefficient of the highest derivative in that equation, vanishes as $Y \rightarrow \delta(X)$ in view of (2.20). Hence, following Nir and Acrivos (1990), another condition is that ϕ be regular for $Y \leq \delta(X)$ or, more generally, that

$$\lim_{Y \rightarrow \delta(X)} \left(\frac{\partial u}{\partial Y} \frac{\partial^2 \phi}{\partial Y^2} \right) = 0 \tag{2.22}$$

which when substituted into the limit of (2.17) as $Y \rightarrow \delta(X)$ leads to

$$u_\delta \frac{d\phi_\delta}{dX} + \left(\frac{\partial \phi}{\partial Y} \right)_{Y=\delta} \left\{ -u_\delta \frac{d\delta}{dX} + v_\delta - \frac{d}{d\phi_\delta} \left(\phi_\delta f(\phi_\delta) \cos\theta - \frac{9\alpha(\phi_\delta)}{2\lambda(\phi_\delta)} (\phi_\delta - \phi_*) \sin\theta \right) + \frac{9\beta(\phi_\delta)}{2\lambda(\phi_\delta)} (\phi_\delta - \phi_*) \sin\theta \right\} = 0 \tag{2.23}$$

when the terms containing $\partial u/\partial Y$ are set equal to zero. In view of the flux matching condition across the interface (2.21), the above equation can be rewritten as

$$u_\delta \frac{d\phi_\delta}{dX} + \left(\frac{\partial \phi}{\partial Y} \right)_{Y=\delta} \mathcal{F}(\phi_\delta, \phi_*, \theta) = 0 \tag{2.24}$$

with

$$\mathcal{F}(\phi_\delta, \phi_*, \theta) = \frac{9}{2\lambda(\phi_\delta)} (\phi_\delta - \phi_*) \left(\beta(\phi_\delta) - \frac{\alpha(\phi_\delta)}{(\phi_\delta - \phi_*)} \right) \sin\theta + \frac{(\phi_\delta f(\phi_\delta) - \phi_* f(\phi_*))}{(\phi_\delta - \phi_*)} \cos\theta - \frac{d}{d\phi_\delta} \left(\phi_\delta f(\phi_\delta) \cos\theta - \frac{9\alpha(\phi_\delta)}{2\lambda(\phi_\delta)} (\phi_\delta - \phi_*) \sin\theta \right) \tag{2.25}$$

which, in general, appears to be a part of a system of coupled set of PDEs plus boundary conditions that need to be solved numerically before the jump across the interface $(\phi_\delta - \phi_*)$ could be determined. In the limit of large X, however, it was shown by Nir and Acrivos (1990) that the particle concentration ϕ within the sediment layer follows a self similar profile, which in turn reduces the differential equation (2.24) to

a simple non-linear algebraic equation

$$\mathcal{F}(\phi_\delta, \phi_s, \theta) = 0 \tag{2.26}$$

with the only unknown being ϕ_δ, since the derivative of ϕ_δ with recpect to X vanishes for this case. In fact, as will be shown later in section 2.2.1, the condition, $\frac{d\phi_\delta}{dX} = 0$, turns out to be the only possibility consistent with the system of equations and boundary conditions given above, valid for the entire range of X. Thus, the jump in concentration $(\phi_\delta - \phi_s)$ can be determined from (2.25) and (2.26) once and for all for given values of ϕ_s and θ, provided the explicit forms of functions α, β, λ and f are known. Figures 2.2 & 2.3 in section 2.5 show a typical solution of this jump condition for the choice of functions reported in section 2.4.

Thus, the governing equations (2.16) & (2.17) along with the boundary conditions (2.19), (2.20), (2.21) and (2.26) form a complete set of PDE, which is valid within the viscous sublayer for the entire range of X except for a very small $O(\epsilon^{2/3})$ region close to the origin where the lubrication approximation no longer holds. Although, in general, this set of equations needs to be solved numerically, it will be seen presently that, as was the case with the problem studied by Nir and Acrivos (1990), a similarity solution applies here as well but only either for small or for large X.

To complete the first step of this analysis, it appears worthwhile to examine briefly the flow within the inertial region, where the viscous term of (2.8) is balanced by inertia and $\phi \equiv \phi_s$, even though this will not affect, to first order, the velocity and particle concentration profiles within the viscous layer considered above. Now since, as was mentioned earlier, the longitudinal velocity component must be of comparable magnitude in both regions, i.e. $O\left(\epsilon^{-2/3}\right)$, the transverse length scale in the inertial region must be $O\left(\overline{R}u_x\right)^{-1/2}$ or $O\left(\overline{R}\epsilon^{-2/3}\right)^{-1/2}$ if the viscous and inertia terms in (2.8) are to balance. Hence, the appropriate transformations within this layer are, in lieu

of (2.15),

$$u = \epsilon^{2/3} u_x, \quad \overline{y} = \left(\overline{R}\epsilon^{-2/3}\right)^{1/2} y, \quad \overline{v} = \epsilon^{2/3}\left(\overline{R}\epsilon^{-2/3}\right)^{1/2} v, \quad X = x \tag{2.27}$$

where $\overline{R} = R\gamma(\phi_*)/\lambda(\phi_*)$ is the Reynolds number based on the properties of the sedimenting suspension. Thus, in view of above scalings, equation (2.8) becomes

$$\frac{\partial^2 u}{\partial \overline{y}^2} = u\frac{\partial u}{\partial X} + \overline{v}\frac{\partial u}{\partial \overline{y}}; \quad \frac{\partial u}{\partial X} + \frac{\partial \overline{v}}{\partial \overline{y}} = 0 \tag{2.28}$$

subject to:

$$\begin{aligned} u = u_\delta,\ \overline{v} = \overline{R}^{1/2}\epsilon^{1/3} v_\delta \rightarrow\ & 0 \quad \text{as} \quad \overline{y} \rightarrow \overline{R}^{1/2}\epsilon^{1/3}\delta(X) \rightarrow 0 \\ \text{and} \quad u \rightarrow\ & 0 \quad \text{as} \quad \overline{y} \rightarrow \infty \end{aligned} \tag{2.29}$$

where u_δ and v_δ are the corresponding velocity profiles from the viscous solution evaluated at $Y = \delta(X)$.

2.2.1 Analysis with Partial Slip (Small X Solution)

Since equations (2.16) and (2.17) are identical to those studied by Nir and Acrivos (1990) for the case of no slip, except for one extra term in (2.17) which accounts for the shear-induced migration of particles due to shear stress gradients, the solutions of the two sets would be expected to have many features in common. However, on account of the partial slip boundary condition (2.19), the similarity solution derived by Nir and Acrivos (1990) no longer applies. Nevertheless, a closer examination of (2.16) and (2.17) suggests that, near the leading edge of the sediment layer, the velocity and particle concentration profiles should be of the form

$$u = AX^a \cos\theta + F'(\eta)X^b \cos\theta + \ldots \quad \text{and} \quad \phi = \phi(\eta) + \ldots \quad \text{with} \quad \eta = Y/X^c \tag{2.30}$$

where the prime denotes differentiation with respect to η and A is an unknown constant. The exponents a,b and c can be easily determined by substituting the above

expressions into the governing equations and the boundary conditions. Thus, the slip boundary condition (2.19) gives $b - c = a$, while matching of the viscous and the buoyancy terms in the momentum balance equation (2.16) leads to $b = 2c$. Finally, by balancing the leading order terms in the particle balance equation (2.17), one finds that $b - 3c = a - 2$. Consequently, $a = 1/2$, $b = 1$, $c = 1/2$ and therefore,

$$\begin{aligned} u &= AX^{1/2}\cos\theta + F'(\eta)X\cos\theta + O\left(X^{3/2}\right) \\ \phi &= \phi(\eta) + O\left(X^{1/2}\right) \end{aligned} \tag{2.31}$$

with $\eta = Y/X^{1/2}$. Then, on substituting the above plus the expression for v, as obtained from the continuity equation, into the momentum and particle balance equations, one obtains, respectively, with prime indicating differentiation with respect to η,

$$\left(\lambda(\phi)G(\eta)\right)' + \frac{9}{2}(\phi - \phi_*)\tan\theta = O\left(R\epsilon^{2/3}\right) \tag{2.32}$$

and

$$\left(\beta(\phi)G(\eta)\phi'\right)' - \left(\frac{9\alpha(\phi)}{2\lambda(\phi)}(\phi - \phi_*)\tan\theta\right)' + \phi'\left[A\eta + \frac{d}{d\phi}\left(\phi f(\phi)\right)\right] = 0 \tag{2.33}$$

where $G = F''$, subject to the boundary conditions along the inclined plate at $\eta = 0$

$$A = \zeta(\phi_0)G(0) \quad \text{(slip condition)} \tag{2.34}$$

and

$$\beta(\phi_0)G(0)\phi'\big|_{\text{at}\,\eta=0} - \frac{9\alpha(\phi_0)}{2\lambda(\phi_0)}(\phi_0 - \phi_*)\tan\theta + \phi_0 f(\phi_0) = 0 \text{ (no flux condition)} \tag{2.35}$$

where ϕ_0 denotes the particle volume fraction at the inclined plate. As mentioned earlier, the longitudinal velocity attains its maximum value at the sediment-suspension interface i.e. at the edge of the viscous layer of thickness $\delta(X) = \delta_0 X^{1/2}$. Therefore,

$$\text{at } \eta = \delta_0, \quad G(\delta_0) = 0 \tag{2.36}$$

Also, continuity of particle flux requires that the expression

$$\underbrace{-(A\delta_0)\phi\cos\theta}_{\text{convective}} \underbrace{-f(\phi)\phi\cos\theta}_{\text{gravity}} + \underbrace{(9\alpha/2\lambda)(\phi-\phi_*)\sin\theta}_{\text{diffusive}} \tag{2.37}$$

should remain the same on either side of the suspension-sediment interface $Y = \delta_0 X^{1/2}$. Thus, if once again the particle volume fraction in the sediment layer just below $\eta = \delta_0$ is denoted by ϕ_s, the flux matching condition at $\eta = \delta_0$ becomes, in view of (2.37),

$$A\delta_0\phi_* + f(\phi_*)\phi_* = (A\delta_0 + f(\phi_s))\,\phi_s - \frac{9\alpha(\phi_s)}{2\lambda(\phi_s)}(\phi_s - \phi_*)\tan\theta \tag{2.38}$$

which is clearly a special form of the general expression (2.21) derived earlier. Thus, the unknown term $(A\delta_0)$ can be computed, for given values of ϕ_* and θ, via the simultaneous solution of (2.26) and (2.38).

It is appropriate at this point to examine the validity of the solution proposed earlier for equation (2.24). In view of the expansion (2.31) in the limit as $X \to 0$, the longitudinal velocity and the transverse coordinate within the sediment layer scale as $u \sim X^{1/2}$ and $Y \sim X^{1/2}$, respectively, which in turn yields

$$X\frac{d\phi_s}{dX} = O(1) \tag{2.39}$$

from equation (2.24) since $\mathcal{F}$ is independent of X as the leading edge is approached. Clearly then, according to the above expression, the first order correction to ϕ_s should be $O(lnX)$ which does not vanish as $X \to 0$. Therefore, the only possiblity for small X, and in fact for any X in view of the parabolic nature of the governing equations, is equation (2.26).

The system of equations and boundary conditions thus obtained can be recast into a boundary value problem involving a single third order ordinary differential equation plus one unknown parameter, A or δ_0, and four boundary conditions. The latter are (2.34), (2.35), (2.36) together with the known values of $\phi = \phi_s$ at $\eta = \delta_0$ and $A\delta_0$, as determined from the simultaneous solution of (2.38) and (2.26). This system can be further simplified, however, by introducing the transformations

$$\xi = \frac{\eta}{\delta_0} \quad \text{and} \quad g = \frac{G}{\delta_0} \tag{2.40}$$

in terms of which the governing equations are as before except for the fact that the unknown parameter A in (2.33) has been replaced with the known term $A\delta_0$. Thus, with this change of notation, equations (2.32) and (2.33) subject to the boundary conditions (2.35), (2.36) and the known value of ϕ_s at $\xi = 1$ reduce to a simple third order boundary value problem within the domain of integration $0 \leq \xi \leq 1$. This was solved numerically by employing an IMSL subroutine DBVPFD which incorporates a variable order, variable step size finite difference method. Once such a solution is obtained, the sediment layer thickness δ_0 can then be easily determined from the slip boundary condition (2.34), which takes the following form

$$\delta_0 = \sqrt{\frac{A\delta_0}{\zeta(\phi_0)g(0)}} \tag{2.41}$$

in terms of the already known parameter $A\delta_0$ and the values of $g(0)$ and ϕ_0 as computed from the numerical integration.

It should be noted here that the solution referred to above only yields the leading order terms of the velocity and particle concentration profiles, which coincide with the exact profiles only in the limit as X approaches zero. In contrast, a complete solution requires the numerical integration of the governing particle concentration and

momentum equations derived in the previous section in the limit $R\epsilon^{2/3} \ll 1$. The details of such a numerical procedure along with some typical results are described in chapter three.

2.2.2 Analysis with No-slip (Large X Solution)

In this section we briefly outline the similarity solution given by Nir and Acrivos (1990) for the case of no slip. As was mentioned earlier, the governing equations analysed by these investigators were same as (2.16) and (2.17) except for an extra term in the latter which however does not alter the structure of the equation. In the absence of the partial slip boundary condition i.e. $\zeta = 0$, these investigators showed that the governing equations (2.16) and (2.17) along with the boundary conditions (2.18), (2.19), (2.20) and (2.21) are amenable to a similarity solution of the type

$$\begin{aligned} u &= X^{2/3} F'(\eta) \cos\theta \\ \phi &= \phi(\eta) \end{aligned} \tag{2.42}$$

where $\eta = Y/X^{1/3}$, and, as before, the prime denotes the differentiation with respect to η. In view of this transformations, the governing equations reduce to

$$\left(\lambda(\phi)F''(\eta)\right)' + \frac{9}{2}(\phi - \phi_*)\tan\theta = O\left(R\epsilon^{2/3}\right) \tag{2.43}$$

and

$$\left(\beta(\phi)F''(\eta)\phi'\right)' - \left(\frac{9\alpha(\phi)}{2\lambda(\phi)}(\phi - \phi_*)\tan\theta\right)' + \phi'\left[F + \frac{d}{d\phi}\left(\phi f(\phi)\right)\right] = 0 \tag{2.44}$$

where use has been made of the continuity equation in obtaining an expression for v. The boundary conditions at the inclined plate now become,

$$F = F' = 0 \qquad \text{at} \qquad \eta = 0 \tag{2.45}$$

and

$$\beta(\phi_0)F''(0)\phi'|_{\text{at}\,\eta=0} - \frac{9\alpha(\phi_0)}{2\lambda(\phi_0)}(\phi_0 - \phi_s)\tan\theta + \phi_0 f(\phi_0) = 0 \text{ (no flux condition)} \tag{2.46}$$

where ϕ_0 refers as before to the particle volume fraction next to the inclined plate. On the other hand, the conditions at the sediment-suspension interface $Y = \delta(X) = \delta^* X^{1/3}$ now reduce to

$$F'' = 0 \tag{2.47}$$

and

$$F_\delta \phi_s + f(\phi_s)\phi_s = (F_\delta + f(\phi_\delta))\,\phi_\delta - \frac{9\alpha(\phi_\delta)}{2\lambda(\phi_\delta)}(\phi_\delta - \phi_s)\tan\theta \tag{2.48}$$

where the latter, which is a special form of the general expression (2.21) derived earlier, refers to the continuity of particle flux across the interface $\eta = \delta^*$. This expression serves as a boundary condition for F at $\eta = \delta^*$ since the particle concentration ϕ_δ at this point is already known from the solution of (2.26), for given values of ϕ_s and θ.

In contrast to the case with partial slip described earlier, these equations require the solution of a fifth order boundary value problem along with a one parameter search because the sediment layer thickness δ^*, and therefore the domain of integration $(0, \delta^*)$ is not known *a priori*. Nir and Acrivos (1990) solved these equations approximately (for $\alpha = 0$) using the Karman-Pohlhausen technique. Here, the equations were solved numerically, for $\alpha \neq 0$, by employing the same IMSL subroutine as used before for the case with partial slip. The results thus obtained were then compared to the corresponding case with partial slip and are shown in section 2.5.

2.3 Specific Forms of the Various Functions

In order to solve numerically the non-linear set of ordinary differential equations described earlier in subsections 2.2.1 & 2.2.2, explicit forms for the functions α, β, λ and f are needed. Here, following Leighton and Acrivos (1986,1987), these functions will be chosen as

$$\lambda(\phi) = \left(1 + \frac{1.5\phi}{1 - \phi/\phi_m}\right)^2 \tag{2.49}$$

$$\alpha(\phi) = K_\sigma \phi^2 \tag{2.50}$$

$$\text{and} \quad \beta(\phi) = \frac{1}{3}\phi^2 \left(1 + \frac{1}{2}e^{8.8\phi}\right) \tag{2.51}$$

where ϕ_m taken here as 0.58, denotes the maximum possible concentration of the particles in a flowing suspension and K_σ is an order one weak function of ϕ. Due to the lack of experimental data for the system considered here, calculations were performed for values of K_σ ranging from 0.0 to 0.6, where 0.6 is close to the value of K_σ obtained experimentally by Leighton and Acrivos (1987) for a channel flow. Moreover, since the hindrance function f appropriate to this problem is unavailable in the literature, the settling velocity of a sphere in the suspension undergoing shear will be assumed to equal to its Stokes settling velocity in a fluid with viscosity $\mu(\phi)$ and density $\rho(\phi)$, thereby leading to the expression for the hindrance function

$$f(\phi) = \frac{(1 - \phi)}{\lambda(\phi)} \tag{2.52}$$

which, in view of (2.49), vanishes as $\phi \to \phi_m$. This expression for f has also been used by Leighton and Acrivos (1986) and by Schaflinger *et al* (1990). Unlike the functions described above, a simple form for the slip coefficient ζ as a function of ϕ_0 has not as yet been reported in the literature. Nevertheless, it will be shown in the next section

that for high concentrations, a simple expression for ζ can be obtained through the use of an effective continuum model due to Chang and Acrivos (1986, 1987).

2.4 Estimation of the Slip Coefficient

Any disperse system such as a suspension can be viewed as macroscopically homogeneous with well defined effective properties provided the particle dimensions are small in comparison with the macroscopic length scale i.e. the length over which the bulk properties vary. In the case of flowing suspensions, for example, the medium could then be modeled as an effective continuum fluid with an effective viscosity and density. Clearly, however, such a representation cannot be justified in the neighborhood of a bounding surface and more specifically over distances from this surface comparable to the particle dimensions. Nevertheless, for this case, it has been found possible to extend the applicability of the effective continuum model by introducing a slip velocity along a solid surface proportional to the local shear rate, as described in boundary condition (2.19). This apparent slip is caused by regions of higher velocity gradients adjacent to the wall, also termed slip regions, which arise owing to the fact that the local volume fraction of suspended particles (defined as the probability density that a given point within the medium will lie within a particle) is lower at the wall than in the bulk.

In the present work, the slip coefficient ζ appearing in (2.19) was determined by following the model proposed by Chang and Acrivos (1986, 1987) for estimating the transport parameters in two phase materials. According to this method, the suspension within the region close to the wall, where the macroscopic length scale is comparable to the size of the particles, can be viewed as an effective continuum fluid but with position dependent properties which approach the corresponding bulk values at a distance a few particle diameters away from the wall. Formally, this approach may be thought of as a matched asymptotic expansion where the region adjacent to

the wall, the lateral dimension of which is comparable to the particle radius $\tilde{a}$, plays the role of an inner region. According to this method , therefore, to account for the variable particle concentration within this region, the relative effective viscosity of the flowing suspension is expressed as

$$\lambda(\tilde{y}) = \lambda\left(p(\tilde{y})\right) \tag{2.53}$$

where $\tilde{y}$ denotes the distance from the wall and p is the probability density that any point lies within a particle. Clearly, p vanishes at $\tilde{y} = 0$ and equals ϕ_0 when $\epsilon \ll \tilde{y}/\tilde{L} \ll \epsilon^{2/3}$, i.e. when $\tilde{a} \ll \tilde{y} \ll \tilde{L}\epsilon^{2/3}$, where ϕ_0 refers, as before, to the bulk particle concentration as $Y \rightarrow 0$. For particle volume fractions less than 40 %, the expression for p can be obtained using the Percus-Yevick approximate solution to the Ornstein-Zernike equation (Lebowitz 1964, Henderson and Smith 1978), but, for higher concentrations, this becomes inaccurate and the experimental data reported by Benenati and Brosilow (1962) may be used to estimate $p(\tilde{y})$. In the present work, however, ϕ_0,the bulk particle concentration near the wall was always found to be close to ϕ_m, its value for random packing, and hence, in view of the experimental results of Benenati and Brosilow, $p(\tilde{y})$ can be approximated by the Heaviside function

$$p = \begin{cases} 0 & 0 \leq \tilde{y} \leq \tilde{a}/2 \text{ or } 0 \leq y \leq \epsilon/2 \\ \phi_0 & \tilde{y} > \tilde{a}/2 \quad \text{or } y \geq \epsilon/2 \end{cases} \tag{2.54}$$

where $y = \tilde{y}/\tilde{L}$ and $\epsilon = \tilde{a}/\tilde{L}$ as before.

Returning now to the momentum balance equation (2.8), it is seen that, within the inner region, the viscous term dominates and hence

$$\lambda(y)\frac{\partial u}{\partial y} = \text{constant} \tag{2.55}$$

In addition though, on account of the requirement that the shear stress be continuous within the region of overlap between the inner and the outer solutions, and in view of the transformations given by (2.15),

$$\lambda(y)\frac{\partial u}{\partial y} = \lambda(\phi_0)\epsilon^{-2/3}\left(\frac{\partial u}{\partial Y}\right)_{Y\to 0} \tag{2.56}$$

where the last term is to be obtained from the solution of (2.16) and (2.17). But, since according to (2.53) and (2.54), $\lambda = 1$ for $0 \leq y \leq \epsilon/2$ and $\lambda = \lambda(\phi_0)$ for $y > \epsilon/2$, integration of (2.56) leads to

$$u\left(y = \frac{\epsilon}{2}\right) = u\left(Y = \frac{\epsilon^{1/3}}{2} \to 0\right) = \frac{\lambda(\phi_0)}{2}\epsilon^{1/3}\left(\frac{\partial u}{\partial Y}\right)_{Y=0} \tag{2.57}$$

Hence, the appropriate expression for the slip coefficient used in (2.19) is, according to this approximate method,

$$\zeta = \left(\frac{\lambda(\phi_0)\epsilon^{1/3}}{2}\right) \tag{2.58}$$

In view of the uncertain accuracy of (2.58), however, it was felt desirable to determine an expression for the slip coefficient experimentally. The details of such an experiment along with some typical results are discussed in Appendix A. As shown in this appendix, most of the experimental data for $\phi_0 \leq 0.51$ follow the expression

$$\zeta = \left(\frac{\lambda(\phi_0)\epsilon^{1/3}}{6}\right) \tag{2.59}$$

which is identical to (2.58) except for a difference in the multiplying constant. For particle concentration higher than 52%, however, the slip coefficient was found to be a function of the shear rate at the wall due to the apparent shear thinning nature of our suspension at these concentrations.

2.5 Results and Discussion

The system of ordinary differential equations derived in section 2.2 for the case of partial slip as well as for no slip were solved using the numerical technique discussed earlier for the specific choice of the various coefficient functions given by (2.49)-(2.52) and (2.59). Figure 2.2 depicts the solution of the jump condition (2.26) as a function of ϕ_s, at $\theta = 45^0$, for various values of K_σ. Due to the fact that (2.26), is independent of X, the net jump across the interface $\phi_\delta - \phi_s$ is the same for the slip as well as for the no-slip case under identical conditions. However, as the degree of resuspension due to the presence of a shear stress gradient increases, ϕ_δ decreases to account for the excess diffusive particle flux from the sediment layer to the interface. It should be pointed out here that the curve for $K_\sigma = 0$ in this figure corresponds to the case treated by Nir and Acrivos (1990). Figure 2.3 shows the solution of the jump condition, at $K_\sigma = 0.6$, for varius angles of inclinations, as a function of feed particle concentration ϕ_s. As discussed earlier, the value of ϕ_δ thus obtained is then used as a boundary condition along with (2.35) and (2.36) to construct a solution of equations (2.32) and (2.33). The particle volume fraction at the wall, ϕ_0, thereby obtained is shown in figure 2.4 as a function of the feed particle concentration ϕ_s. The decrease in ϕ_0 as K_σ increases merely reflects the increase in the diffusive particle flux due to the gradient in the shear stress from the inclined plate towards the sediment-suspension interface. As shown in figure 2.5, for $K_\sigma = 0.6$, this decrease in ϕ_0 is also seen for higher angles of inclinations and becomes more significant at low feed particle concentrations when ϕ_s approaches ϕ_m. As shown in figures 2.6 & 2.7, the corresponding solutions for the case of no-slip also show a similar behavior.

As discussed in section 2.2.1 , once equations (2.32) and (2.33) have been solved, δ_0 can be determined using (2.41) which, however, includes the factor $\epsilon^{1/6}$ in view of (2.59). Thus, in order to present a general solution independent of ϵ, a modified sediment layer thickness $\delta_0\epsilon^{1/6}$ was calculated as a function of the feed

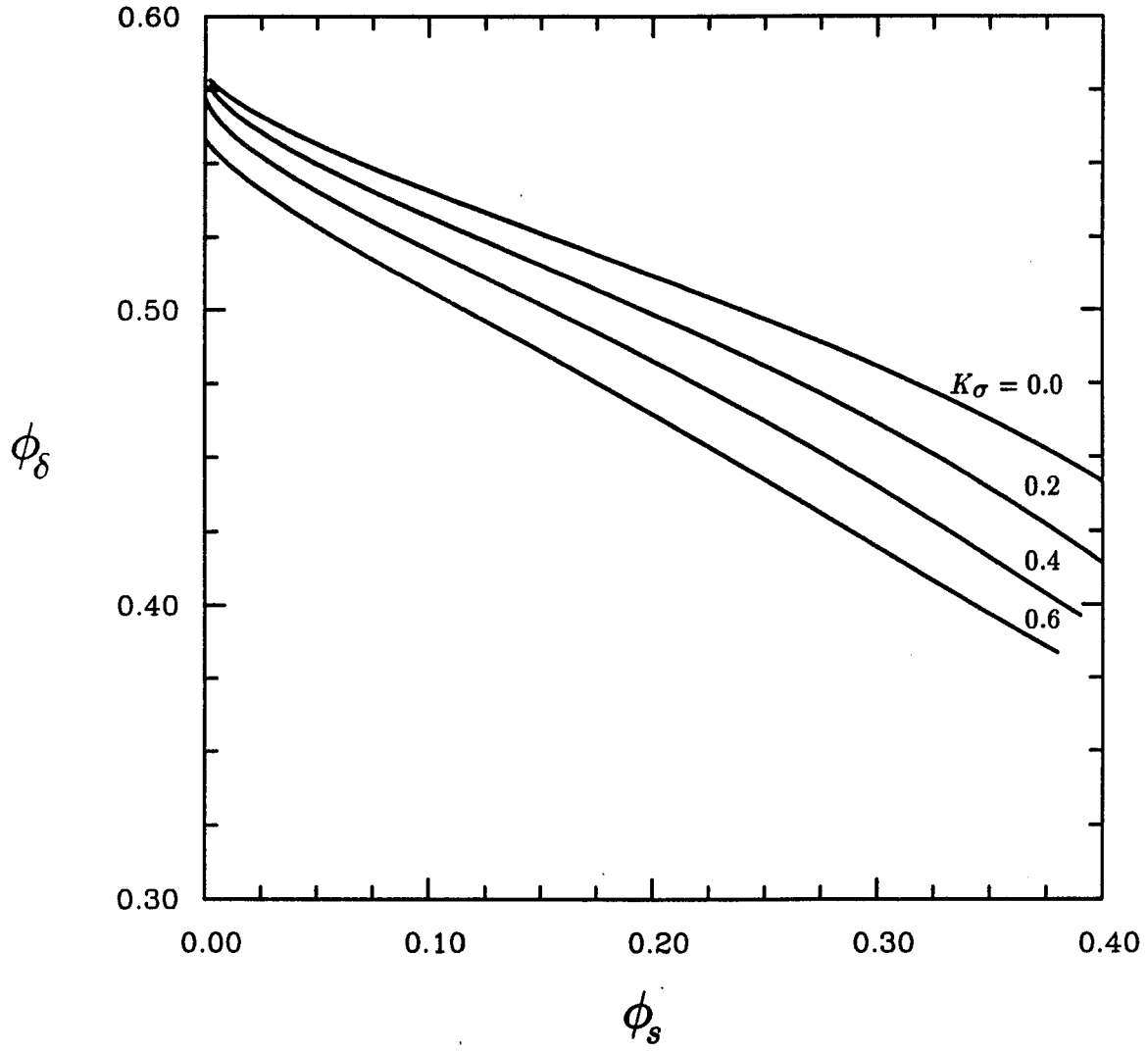

Figure 2.2: Particle volume fraction at the edge of the sediment layer, ϕ_δ, as a function of ϕ_s, for $\theta = 45°$.

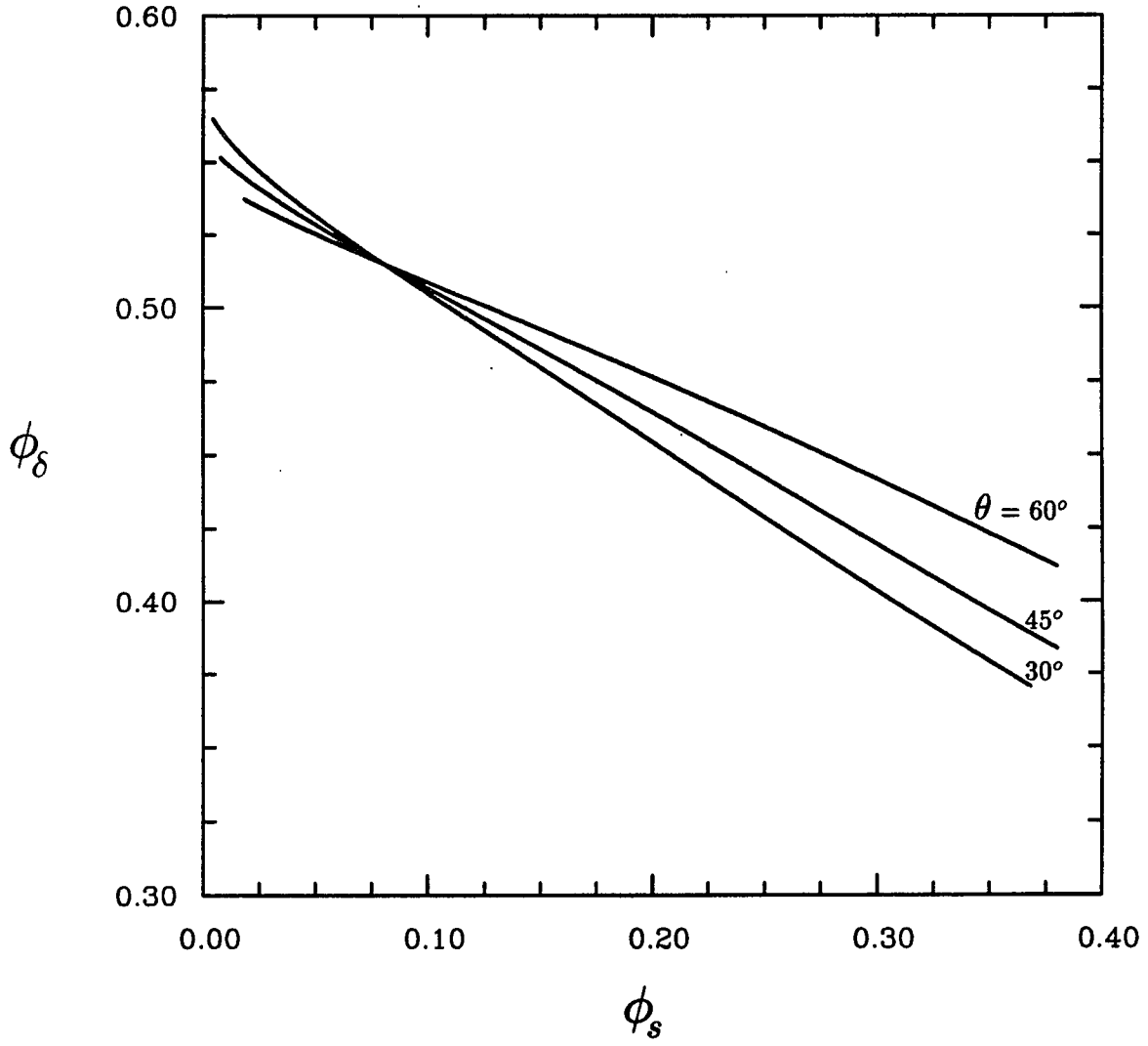

Figure 2.3: Particle volume fraction at the edge of the sediment layer, ϕ_δ, as a function of ϕ_s, for $K_\sigma = 0.6$ and for $\theta = 30°$, 45° and 60°.

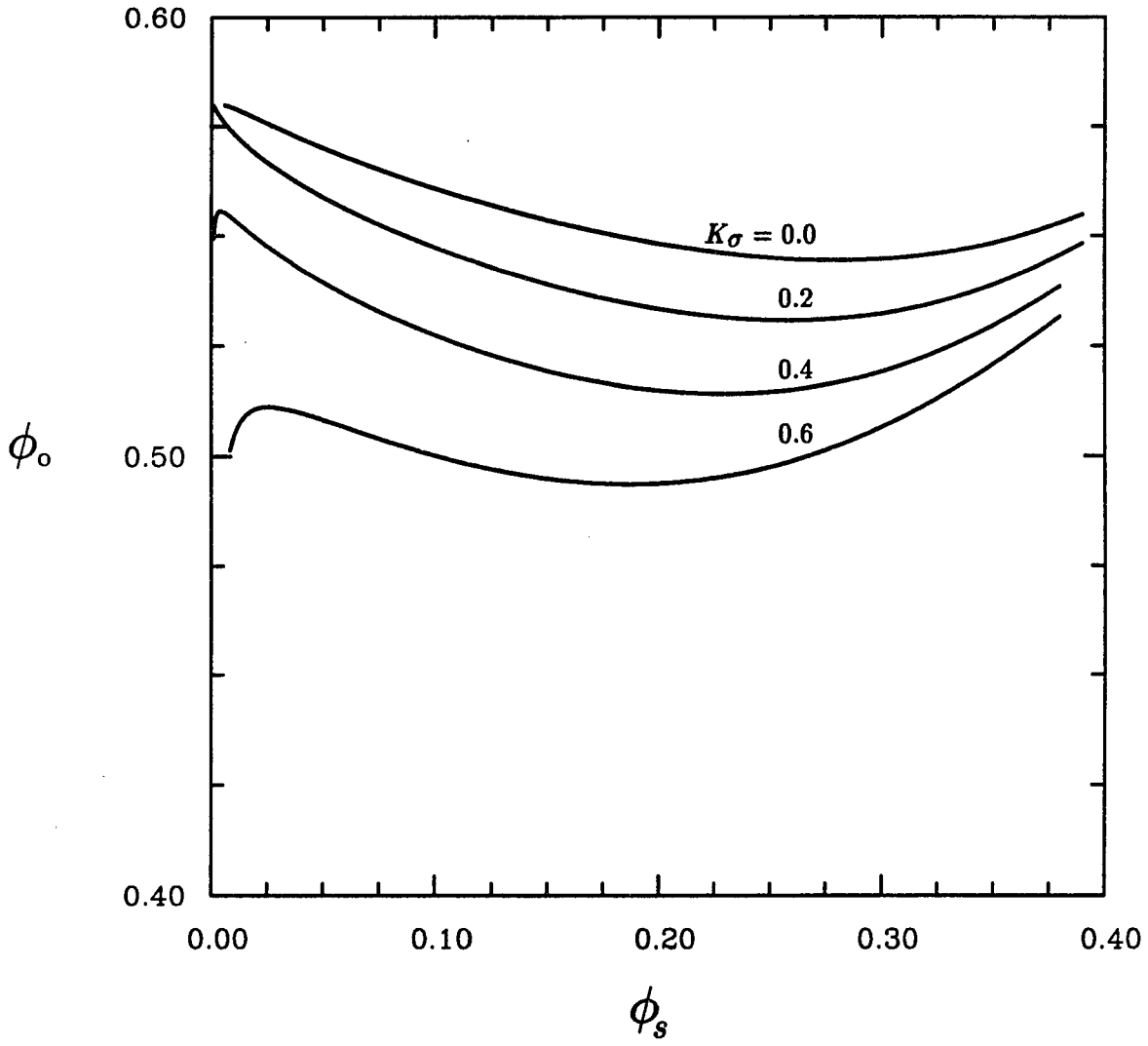

Figure 2.4: The particle volume fraction at the plate, ϕ_0, for the case with partial slip, as a function of ϕ_s, for $\theta = 45°$.

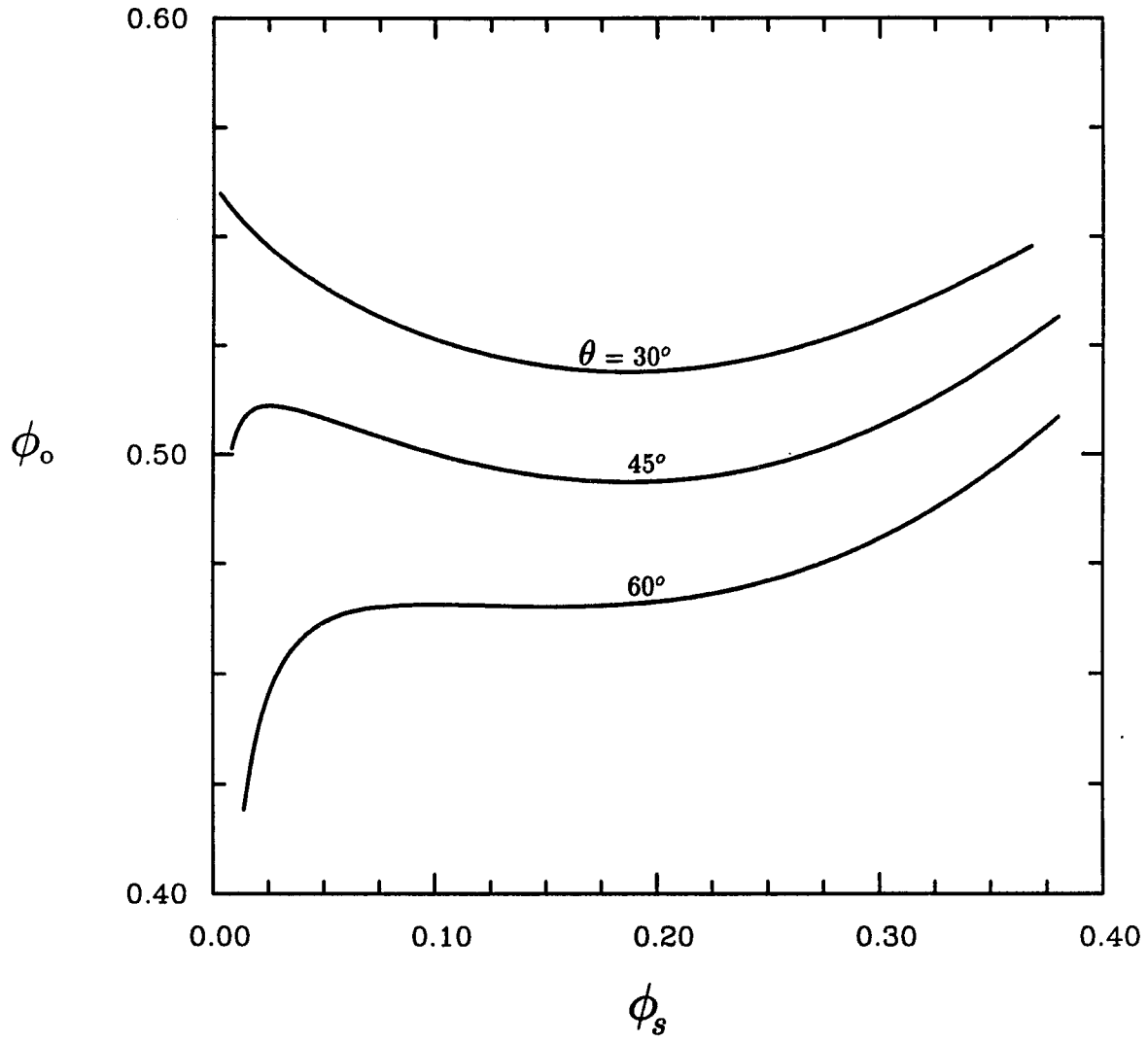

Figure 2.5: The particle volume fraction at the plate, ϕ_0, for the case with partial slip, as a function of ϕ_s, for $K_\sigma = 0.6$ and for $\theta = 30°$, 45° and 60°.

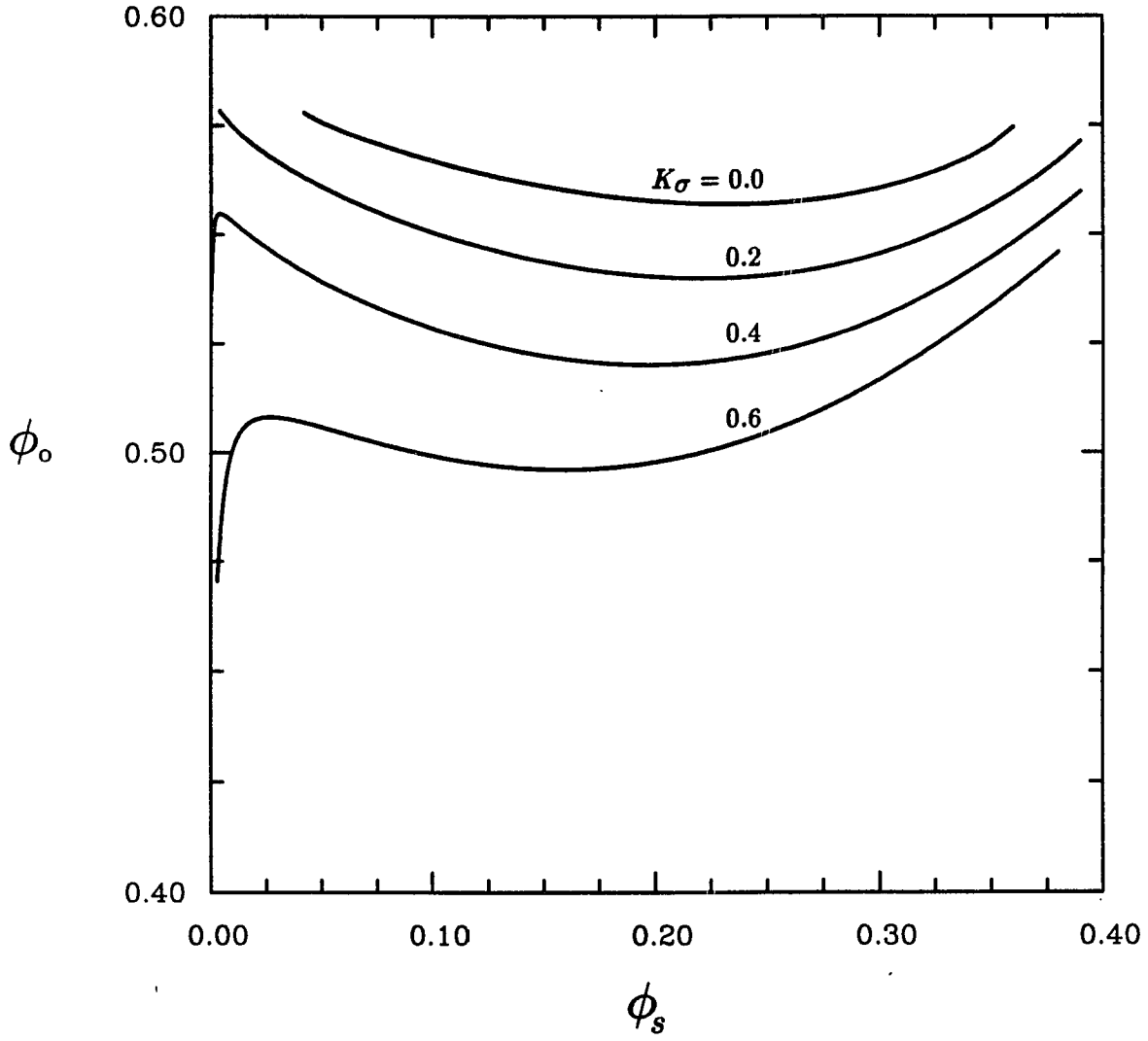

Figure 2.6: Particle volume fraction at the plate, ϕ_0, for the case of no-slip, as a function of ϕ_s, for $\theta = 45°$.

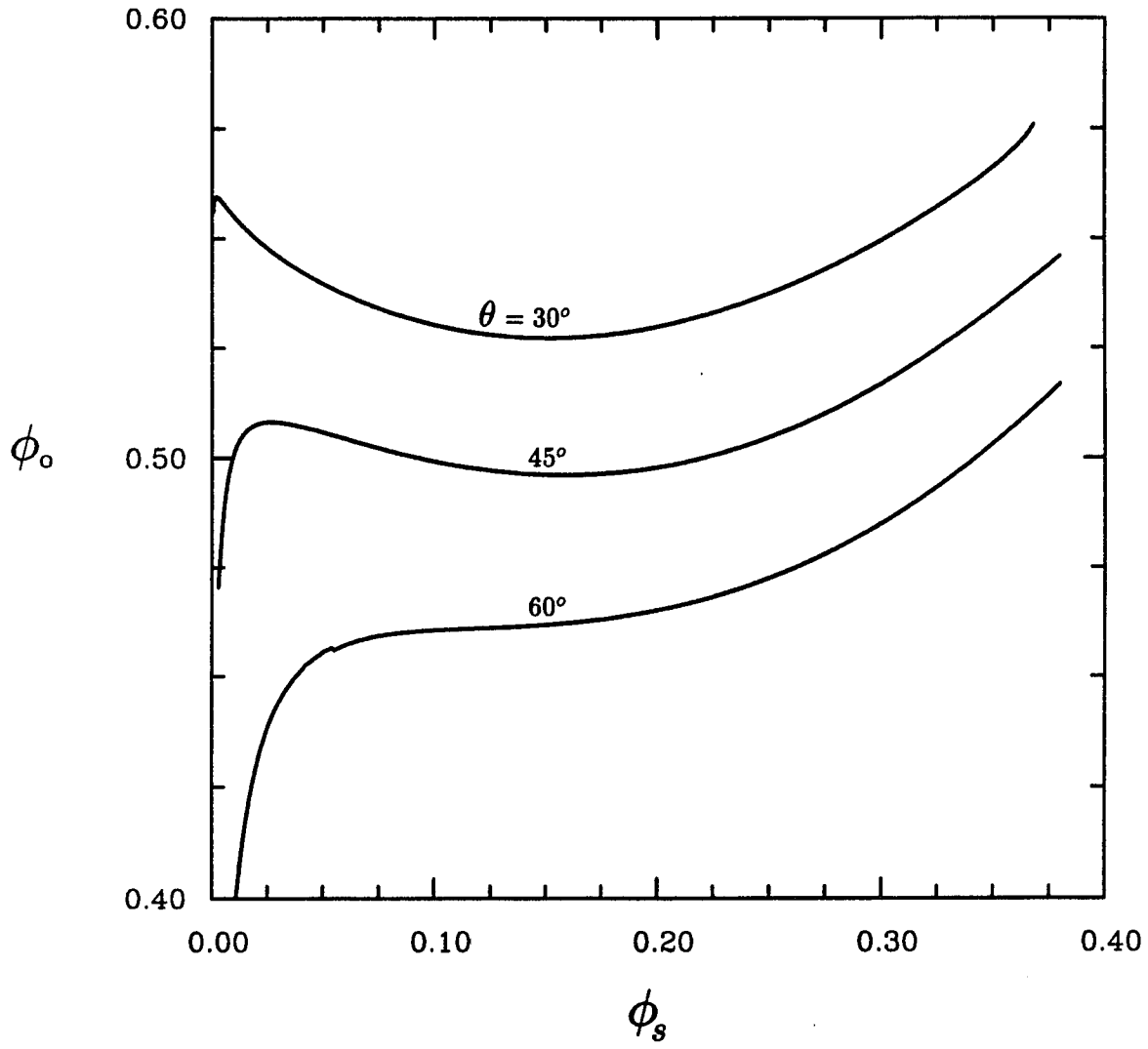

Figure 2.7: Particle volume fraction at the plate, ϕ_0, for the case of no-slip, as a function of ϕ_s, for $K_\sigma = 0.6$ and for $\theta = 30°$, 45° and 60°.

particle concentration and is shown in figure 2.8, again for $\theta = 45^0$, while the effect of change in angle of inclination on this modified thickness is depicted in figure 2.9. On comparing these figures with that for the case of no-slip (fig. 2.10 & 2.11), it is seen that the inclusion of slip as well as diffusion due to gradients in the shear stress alter the qualitative nature of the sediment layer thickness profile in a major way, and that the puzzling result reported by Nir and Acrivos (1990), for $K_\sigma = 0$, in which δ_0 was found to increase without bound as $\phi_s \rightarrow 0$, is thereby eliminated.

According to the effective continuum model adopted here, there exist two possible mechanisms by which the sediment layer thickness can approach zero in the limit $\phi_s \rightarrow 0$. The first possibility arises when the average concentration within the sediment layer remains close to ϕ_m and the slip velocity at the inclined plate is an O(1) quantity. Physically this represents a plug of constant concentration slipping along the inclined plate. The second possibility occurs when the particle concentration close to the wall remains less than the average particle concentration within the sediment layer. But, if the boundary condition (2.35) is examined closely, it is obvious that in the absence of shear induced diffusion due to a gradient in the shear stress, the particle volume fraction will always increase monotonically away from the wall to balance the gravitational particle flux. Therefore, within the framework of the model proposed by Nir and Acrivos (1990), resuspension due to a concentration gradient alone subject to the no-slip boundary condition at the wall, can never lead to a sediment layer thickness which approaches zero as $\phi_s \rightarrow 0$. However, when $K_\sigma > 0$, the contributions due to the shear stress gradient term enhances the resuspension process which in turn reduces the average particle concentration within the sediment and leads to a relatively thinner sediment layer. In fact, for higher values of K_σ, the gravitational flux and the diffusive flux due to a concentration gradient will act in the same direction in order to balance the diffusive flux due to the shear stress gradient. In turn, this reduces the particle volume fraction close to the wall (as

shown in figures 2.4-2.7) and consequently the sediment layer thickness decreases as the feed particle concentration approaches zero.

Figures 2.12 shows the domain within which a steady state solution of the boundary layer equations will exist for the case of small X as well as the large X asymptotic solutions. The solid line in this plot depicts the predictions based on the small X asymptotic solution, while the dashed line refers to the corresponding predictions due to the large X asymptotic solution. It is seen that partial slip along the inclined plate as well as resuspension due to a gradient in the shear stress both lead to a wider domain of steady solutions.

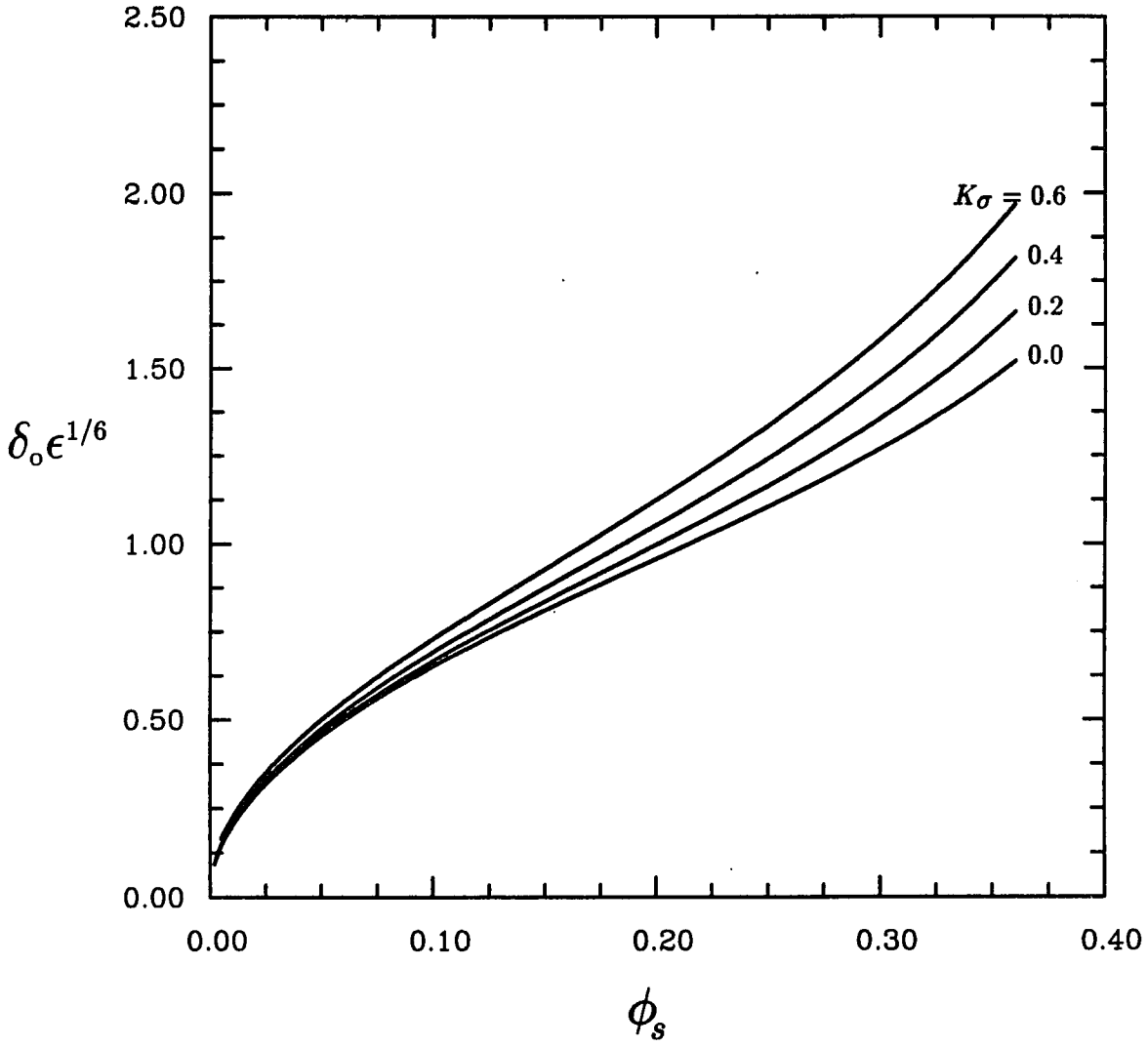

Figure 2.8: The sediment layer thickness parameter, $\delta_0 \epsilon^{1/6}$, for the small X solution, as a function of ϕ_s, for $\theta = 45°$.

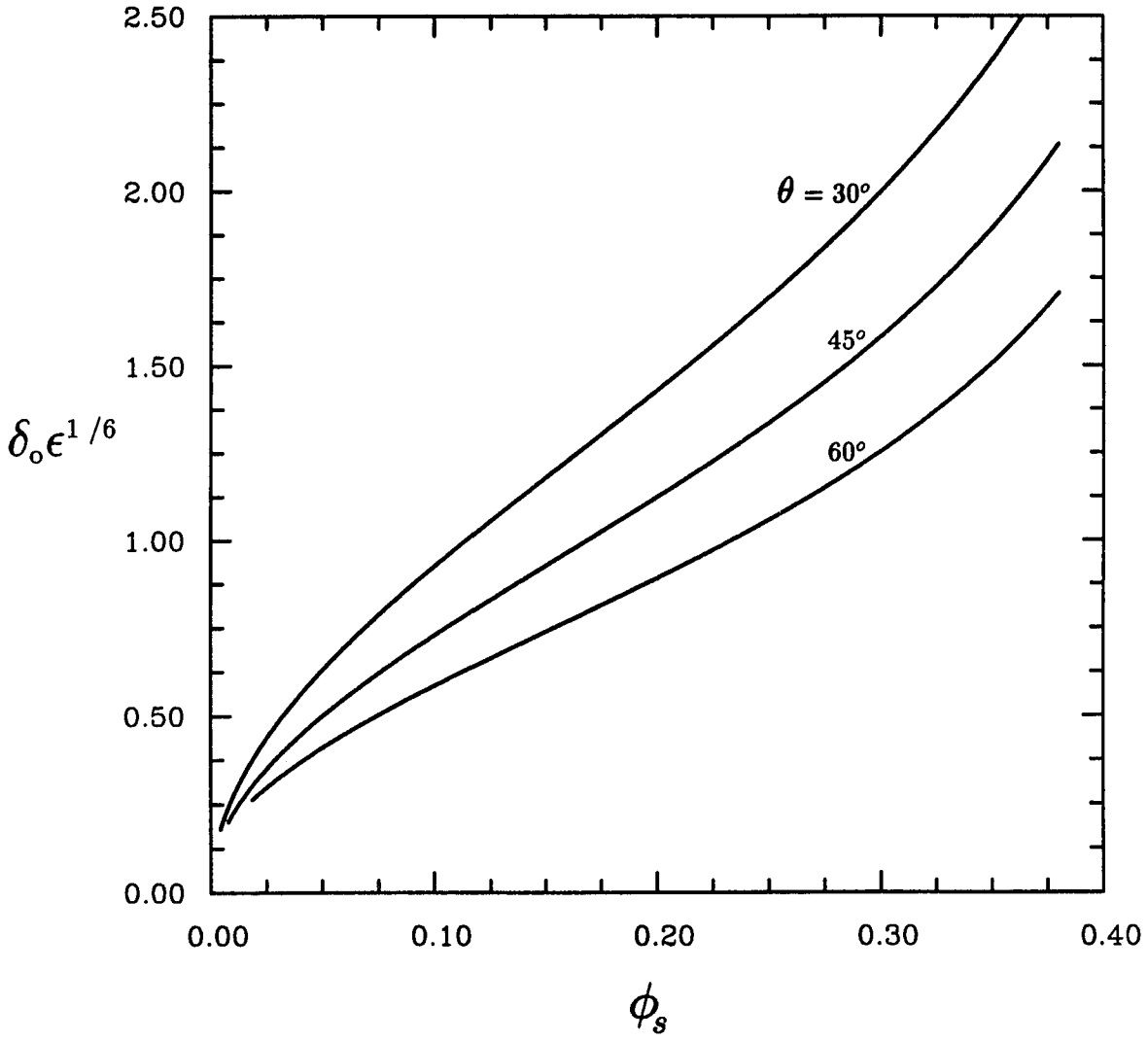

Figure 2.9: The sediment layer thickness parameter, $\delta_0 \epsilon^{1/6}$, for the small X solution, as a function of ϕ_s, for $K_\sigma = 0.6$ and for $\theta = 30°$, 45° and 60°.

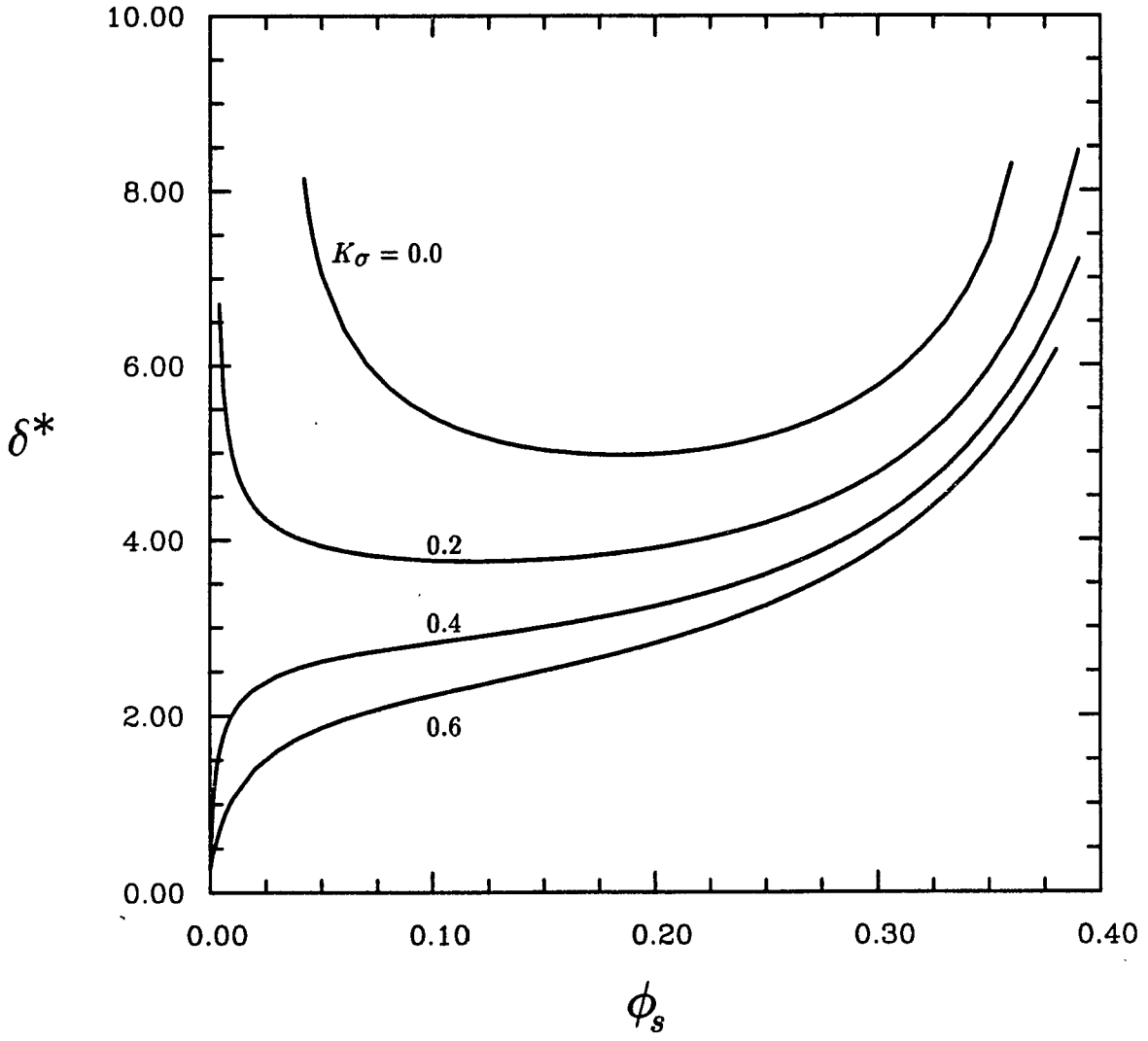

Figure 2.10: The sediment layer thickness parameter, δ^*, for the large X solution, as a function of ϕ_s, for $\theta = 45°$.

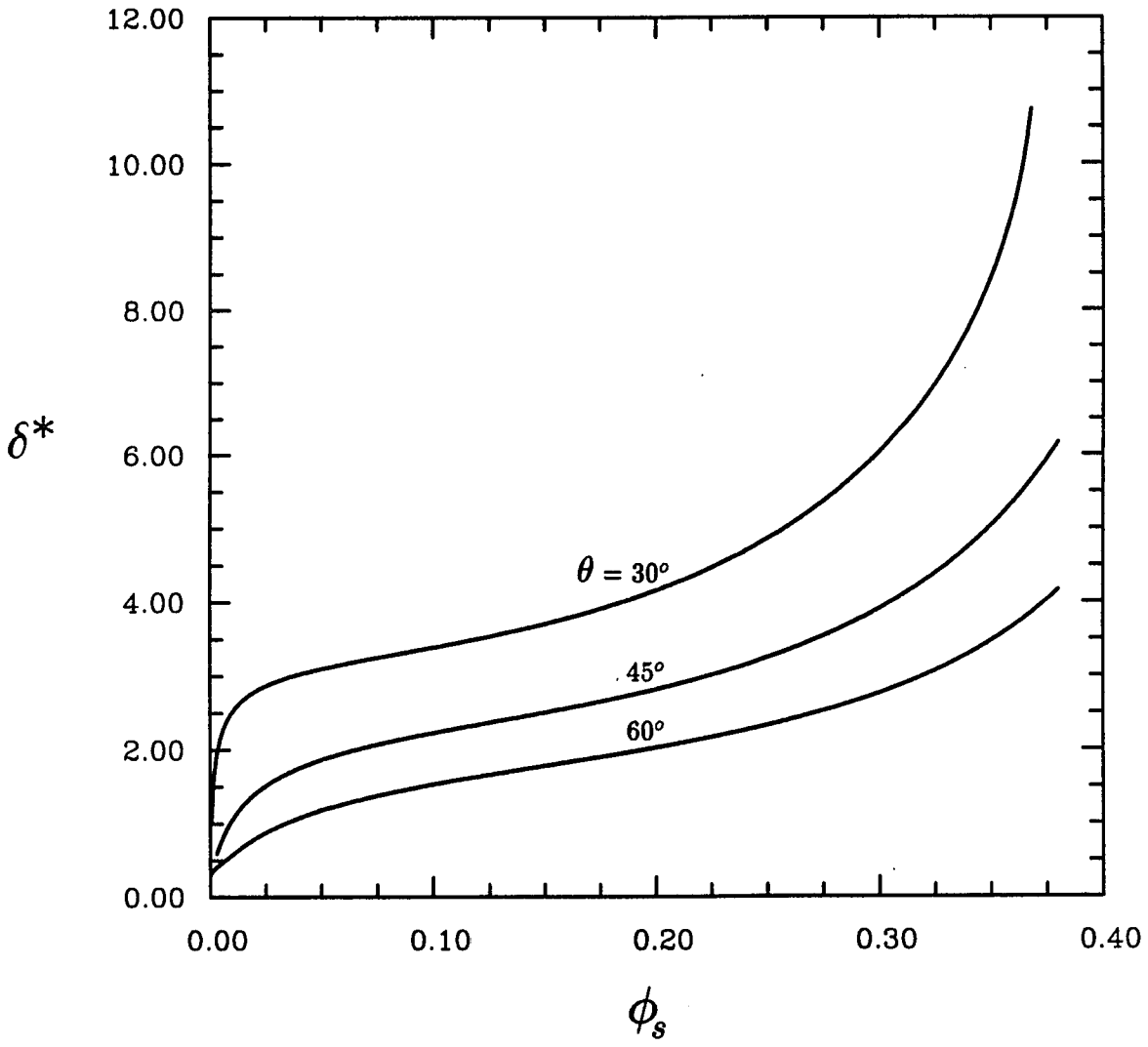

Figure 2.11: The sediment layer thickness parameter, δ^*, for the large X solution, as a function of ϕ_s, for $K_\sigma = 0.6$ and for $\theta = 30°$, $45°$ and $60°$.

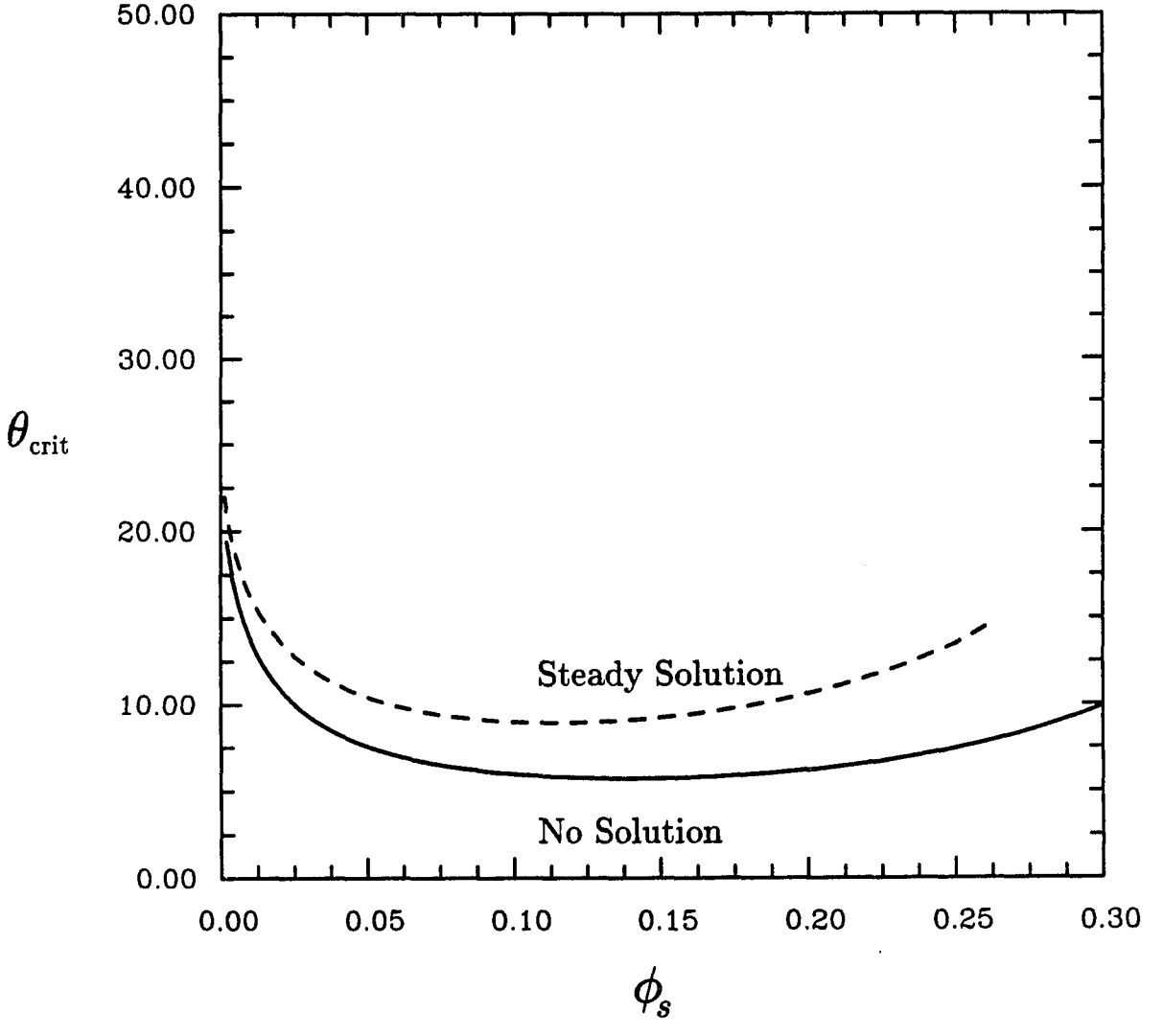

Figure 2.12: The critical angle of inclination below which a steady motion of the sediment layer cannot exist, as a function of ϕ_s. Solid curve —— theory with slip; dashed curve – – – theory without slip.

Chapter 3

Solution for all X

3.1 Introduction

As mentioned earlier, the theoretical predictions presented in the preceeding chapter describe the flowing sediment layer either at the leading edge of the inclined plate or at far downstream. In order to draw a meaningful comparison with the experiments and also to determine the range of applicability of these asymptotic solutions, it is necessary to obtain a complete numerical solution valid for all X. The purpose of this chapter, therefore, is to characterize the flowing sediment layer, based on the numerical solution of the equations presented earlier in chapter two, for the entire range of X.

The governing equations for this flow have already been described in detail in section 2.2, however, these can be rewritten in a form which is independent of the small parameter ϵ by choosing the particle radius $\tilde{a}$ as a characteristic length instead of $\tilde{L}$ as used before. Consequently, the corresponding forms of the momentum equation (2.8) along the x-direction and of the continuity equation (2.9) reduce now, in terms of new variables, $x \equiv \frac{\mathcal{X}}{\epsilon}$ and $y \equiv \frac{\mathcal{Y}}{\epsilon}$, to

$$\frac{\partial}{\partial y}\left[\lambda(\phi)\frac{\partial u}{\partial y}\right] + \frac{9}{2}(\phi - \phi_s)\sin\theta = R_p\gamma(\phi)\left(u\frac{\partial u}{\partial x} + v\frac{\partial u}{\partial y}\right) \tag{3.1}$$

$$\frac{\partial u}{\partial x} + \frac{\partial v}{\partial y} = 0 \tag{3.2}$$

where $R_p = \tilde{\rho}_f \tilde{u}_t \tilde{a}/\tilde{\mu}_f$ is the particle Reynolds number and u & v denote the dimensionless velocity components along the x & y directions respectively. In addition, in view of the small values of R_p in most practical situations, the terms on the right hand side may be neglected to leading order. Similarly, the particle particle balance equation (2.12) can be rewritten in terms of the dimensionless variables introduced earlier as

$$u\frac{\partial \phi}{\partial x} + v\frac{\partial \phi}{\partial y} - \frac{\partial}{\partial y}\{f(\phi)\phi\cos\theta\} = \frac{\partial}{\partial y}\left(\beta(\phi)\frac{\partial u}{\partial y}\frac{\partial \phi}{\partial y} + \frac{\alpha(\phi)}{\lambda(\phi)}\frac{\partial}{\partial y}\left(\lambda(\phi)\frac{\partial u}{\partial y}\right)\right) \tag{3.3}$$

Thus, (3.1), (3.2) and (3.3) constitute the set of governing equations which need to be solved numerically together with the by now familiar boundary conditions of no flux and partial slip at $y = 0$, i.e.

$$\beta(\phi)\frac{\partial u}{\partial y}\frac{\partial \phi}{\partial y} + \frac{\alpha(\phi)}{\lambda(\phi)}\frac{\partial}{\partial y}\left(\lambda(\phi)\frac{\partial u}{\partial y}\right) + \phi f(\phi)\cos\theta = 0 \tag{3.4}$$

and

$$u = \hat{\zeta}\left(\frac{\partial u}{\partial y}\right) \quad \text{and} \quad v = 0 \tag{3.5}$$

respectively, where $\hat{\zeta} \equiv \zeta\epsilon^{-1/3}$ denotes the slip coefficient, which is now independent of ϵ. Similarly, the conditions at the sediment- suspension interface remain the same as before, i.e. at $y = \delta(x)$,

$$\frac{\partial u}{\partial y} = 0 \tag{3.6}$$

$$\left[-u_\delta\frac{d\delta}{dx} + v_\delta - f(\phi_\delta)\cos\theta\right]\phi_\delta + \frac{9\alpha(\phi_\delta)}{2\lambda(\phi_\delta)}(\phi_\delta - \phi_s)\sin\theta = \left[-u_\delta\frac{d\delta}{dx} + v_\delta - f(\phi_s)\cos\theta\right]\phi_s \tag{3.7}$$

where, as before, ϕ_δ denotes the particle concentration as the interface is approached from below and u_δ and v_δ are the corresponding velocity components evaluated at sediment-suspension interface, $y = \delta(x)$.

Clearly, the momentum and particle balance equations (3.1) & (3.3) along with the continuity equation (3.2) are parabolic with x as a marching coordinate and can be solved by a number of numerical techniques. In the present case, however, we have chosen the method of finite differences, which is realtively easy to implement, and, in view of the one dimensional discretization required for the present system, is expected to give quite an accurate set of solutions.

3.2 Formulation

The method of finite differences essentially involves the discretization of the continuous domain into a finite difference mesh or grid. The governing equations, with the derivatives expressed in difference form are then satisfied at each of these grid points. Although there exist several possible ways of approximating the derivatives by finite differences, we shall choose here the central difference representation, according to which the first order derivatives along the y-direction can be expressed as

$$\left(\frac{\partial u}{\partial y}\right)_j = \frac{\Theta\left(u_{j+1}^{n+1} - u_{j-1}^{n+1}\right) + (1-\Theta)\left(u_{j+1}^{n} - u_{j-1}^{n}\right)}{2\Delta y} \tag{3.8}$$

with a truncation error of $O\left(\Delta y^2\right)$. The subscript j here refers to the j^{th} mesh point along the y-direction and the variation of the marching coordinate is indicated by a superscript. The expression (3.8) represents a general form of a finite difference equation, where the limits of the parameter $\Theta(0,1)$ correspond to a fully explicit or a fully implicit method respectively. The derivatives along the x-direction are discretized as

$$\frac{\partial u}{\partial x} = \frac{\left(u_j^{n+1} - u_j^n\right)}{\Delta x} \tag{3.9}$$

with a truncation error of $O(\Delta x)$, which in general can be controlled by choosing the size of the appropriate marching step. For any implicit method ($\Theta \neq 0$), the finite difference form of the momentum and particle balance equations give rise to a set of nonlinear algebraic equations due to the appearence of unknown quantities at the $(n+1)^{th}$ level. Thus, in order to simplify the procedure for solving this set, it is necessary to linearize this system, which in the present case is achieved by employing Newton's method of linearization to iteratively update the coefficients. According to this method, nonlinear terms like $u_j^{n+1}\phi_j^{n+1}$, which for example appear in the difference form of the particle balance equation (3.3), are treated as

$$u_j^{n+1}\phi_j^{n+1} = \hat{u}_j^{n+1}\phi_j^{n+1} + \hat{\phi}_j^{n+1}u_j^{n+1} - \hat{u}_j^{n+1}\hat{\phi}_j^{n+1} \tag{3.10}$$

where the variables with the hat are those obtained from the previous iteration. Therefore, for the first iteration, $\hat{u}_j^{n+1}$ & $\hat{\phi}_j^{n+1}$ is most conveniently evaluated as u_j^n & ϕ_j^n respectively.

Figure 3.1 shows the typical grid being adopted in the present case. As shown in this figure, the boundary $y = \delta(x)$, which represents the sediment-supension interface, is not parallel to the wall, however, for the sake of simplicity a rectangular mesh is chosen with constant Δy during each marching step. As a first approximation, the size of the marching step,Δx, is then chosen such that the condition $\Delta\delta \ll \Delta y$ is satisfied.

On linearizing the difference form of the governing equations, we then obtain a set of simple algebraic equations of the form,

$$A_j u_{j-1}^{n+1} + B_j \phi_{j-1}^{n+1} + C_j u_j^{n+1} + D_j \phi_j^{n+1} + E_j u_{j+1}^{n+1} + F_j \phi_{j+1}^{n+1} = G_j \tag{3.11}$$

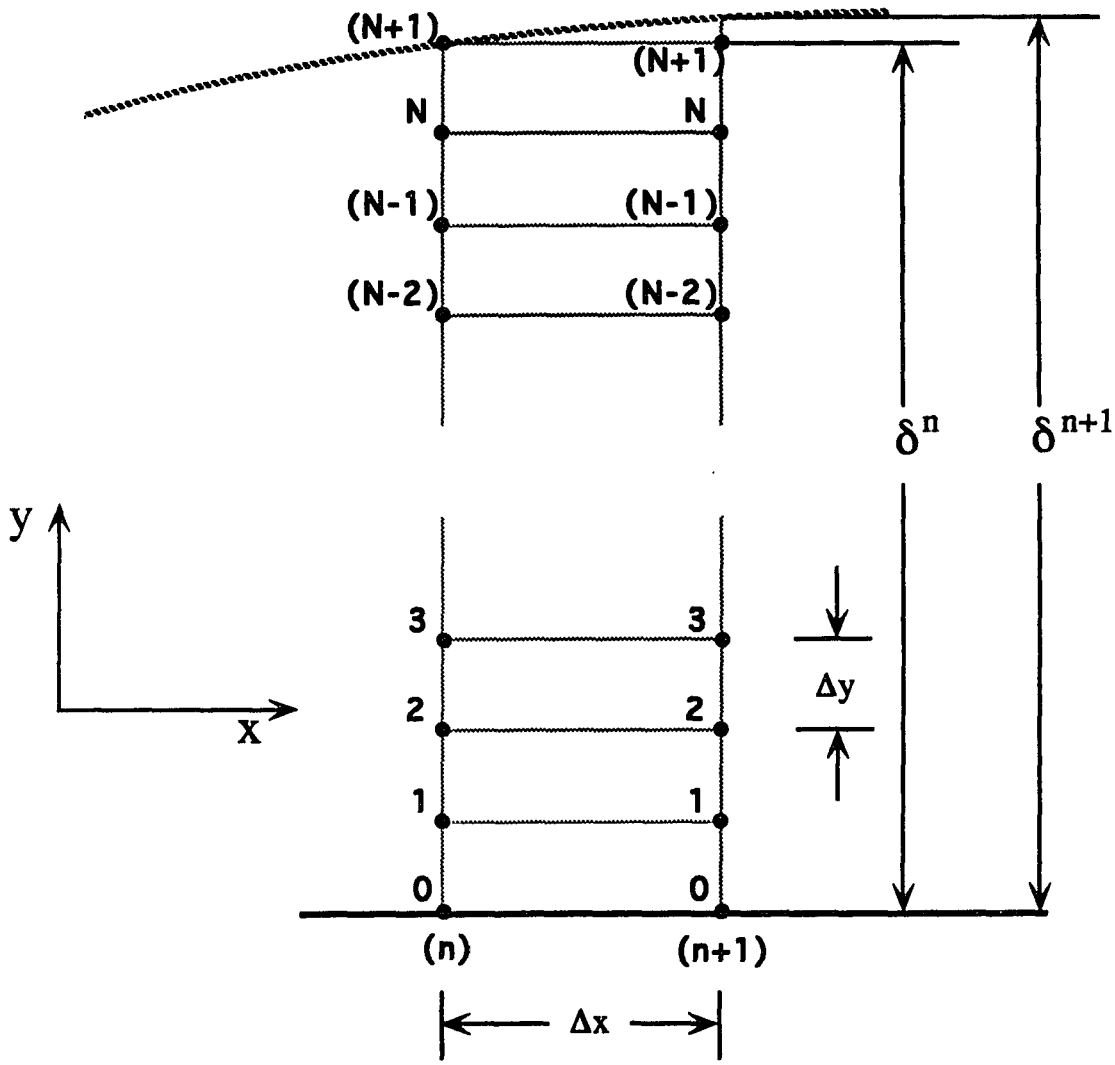

Figure 3.1: Schematic description of the finite difference grid used.

for the momentum balance,

$$H v_{j-1}^{n+1} + I u_j^{n+1} + J v_j^{n+1} = K_j \tag{3.12}$$

for the continuity equation; and

$$L_j u_{j-1}^{n+1} + M_j \phi_{j-1}^{n+1} + N_j u_j^{n+1} + O_j v_j^{n+1} + P_j \phi_j^{n+1} + Q_j u_{j+1}^{n+1} + R_j \phi_{j+1}^{n+1} = S_j \tag{3.13}$$

for the particle conservation equation, where j varies from 1 to N and the coefficients $(A_j - S_j)$ are functions of the variables at the n^{th} step as well as at the $(n+1)^{th}$ step evaluated from a previous iteration i.e. variables with a hat. Thus, equations (3.11), (3.12) and (3.13) constitute a set of $3N$ algebraic equations with $(3N+5)$ unknowns. Out of the five equations required to close this set, three can be readily obtained by discretizing the no flux and partial slip conditions on the inclined plate. However, due to the appearence of derivatives at the outermost mesh point, the central difference representation (eq (3.8)) described earlier can no longer be applied here. Instead, a simple polynomial fitting may be employed, which in turn leads to the difference form

$$A_o u_n^0 + B_o u_n^1 + C_o u_n^2 + D_o \phi_n^0 + E_o \phi_n^1 + F_o \phi_n^2 = G_o \tag{3.14}$$

and

$$u_n^0 = \frac{\hat{\zeta}}{2\Delta y}\left\{3.0 u_n^0 - 4.0 u_n^1 + u_n^2\right\} \quad \text{and} \quad v_n^0 = 0 \quad \text{for all } n \tag{3.15}$$

with a third order polynomial fitting. The remaining two boundary conditions, namely the jump condition and the zero shear condition, however, cannot be incorporated directly since they are defined on the interface instead of at the outermost node ($(N+1)^{th}$) and at the $(n+1)^{th}$ x location (c.f. figure 3.1). Therefore, in order to complete this set of algebraic equations it is necessary to formulate two conditions at the $(n+1, N+1)^{th}$ mesh point, based on the conditions at the interface. Clearly, the

first condition can be easily obtained by integrating the momentum balance equation from $y = \delta^n$ to $y = \delta^{n+1}$, which yields

$$\lambda(\phi)\left(\frac{\partial u}{\partial y}\right)_{\text{at the } (N+1)^{th} \text{ node}} = -\frac{9}{2}\sin\theta \int_{\delta^n}^{\delta^{n+1}} (\phi - \phi_*) dy \qquad (3.16)$$

in view of the zero-shear condition at the interface. Once again, equation (3.16) can be easily expresed in difference form involving variables at nodes $(N+1)$, N and $(N-1)$ by employing a simple third order polynomial fitting. In addition, the unknown δ^{n+1} appearing in the above expression can be determined from the jump conditions (2.21) and (2.23), which take the form

$$\delta^{n+1} = \delta^n + \text{Fn}(\text{ variables at the } n^{th} \text{ step}\,)\,\Delta x \qquad (3.17)$$

and

$$\phi\left(y = \delta^n\right) = \phi_\delta \quad \text{for all } n \qquad (3.18)$$

when the former is discretized in an explicit manner. Then with the particle volume fraction at the interface and the thickness of sediment layer known at the $(n+1)$ location, the second condition can be easily arrived at by means of a linear interpolation between the mesh point N and the interface $y = \delta^{n+1}$ to yield the expression

$$\phi_{N+1}^{\,n+1} = \phi_N^{\,n+1} + \left(\frac{\phi_\delta - \phi_N^{\,n+1}}{\Delta y + \delta^{n+1} - \delta^n}\right)\Delta y \qquad (3.19)$$

for the particle volume fraction at the $(n+1, N+1)^{th}$ node. Therefore, the above together with equations (3.11) - (3.16) constitute a complete set of linear algebraic equations for the variables u, v and ϕ at the $(n+1)^{th}$ location in x.

In general, this set of linear algebraic equations can be solved simultaneously. However, it was found convenient to solve them in a sequential manner with the implicit parameter, Θ, set equal to zero in the momentum equation (3.11) and equal to 0.5 in equations (3.12) & (3.13) which contain the partial derivatives with respect to

x. In order to perform this sequential procedure, these equations were first decoupled by replacing (ϕ_j^{n+1}), (u_j^{n+1}) and (u_j^{n+1} & v_j^{n+1}) with the corresponding variables with a hat in equations (3.11), (3.12) and (3.13) respectively. The marching procedure was then started at some small x, where the similarity solution developed in chapter 2 was expected to hold, using at this point the v and ϕ profiles as obtained from the small X similarity solution. The profile of u at the starting step ($x = x_0$), however, were evaluated using equation (3.11), in order to be consistent with the difference form. The next step consisted in solving the particle balance equation using these values of u_j^n & v_j^n as a first guess for $\hat{u}_j^{n+1}$ & $\hat{u}_j^{n+1}$ to obtain ϕ^{n+1}. The values of the ϕ's thus computed provided a second guess for $\hat{\phi}_j^{n+1}$ which was then substituted into the momentum balance equation for the next guess for $\hat{u}_j^{n+1}$. A new estimate for $\hat{v}_j^{n+1}$ was finally obtained from the continuity equation. This iterative procedure was repeated until convergence for the variables at the $(n+1)^{th}$ step was achieved. The criterion for this was the difference between the variables at two consecutive iterations divided by the variable itself was less than some specified small parameter, 10^{-8}. Once convergence was reached, the grid points were redistributed at the $(n+1)^{th}$ step, using an interpolation procedure in order to force the $(N+1)^{th}$ node onto the interface, as was the case for the n^{th} step, and the sequential procedure described above was repeated using the solution at the $(n+1)^{th}$ location to obtain the solution at the $(n+2)^{th}$ step. It should be pointed out, however that, according to this procedure, the use of a constant number of grid points implies a different Δy at each x location.

3.3 Results and Discussion

In the sequential solution procedure described earlier, the momentum balance equation is solved at each x given the known ϕ profile at that point. Thus, the parameter Θ is taken to be zero. On the other hand, the particle balance and continuity equations, which contain the derivatives with respect to x are solved implictly

with $\Theta = 0.5$. As mentioned earlier, the expression for the coefficient functions α, β, λ and f are given by (2.49)-(2.52) while, in view of (2.59), the slip coefficient $\hat{\zeta}$ becomes

$$\hat{\zeta} = \frac{\lambda(\phi_0)}{6} \tag{3.20}$$

independent of ϵ.

In order to test the convergence of the finite difference formulation, the special case of no-slip for all x (Nir & Acrivos, 1990) was solved first for $\alpha \neq 0$, since the similarity solution for this case applies everywhere. Thus, the numerical integration was started at some small x with initial conditions taken from the similarity solution given in subsection (2.2.2). The numerical solution thus obtained from the marching procedure was then compared, at some large x, with the same similarity solution used initially and was found to match within a few percent. Since, for this case the system of equations and boundary conditions has almost the same structure as that with partial slip, this test procedure gave an indication for the number of grid points, as well as for step size, necessary to achieve convergence.

Accordingly, fifty grid points along the y-direction were found to be sufficient, while the step size was chosen sufficiently small in order to satisfy the condition $(\delta_{n+1} - \delta_n) \ll \Delta y$. A typical result obtained by this numerical solution is shown in figure 3.2, which depicts the variation of the dimensionless sediment layer thickness δ with respect to x, for $\phi_s = 9.6\%$ and $\theta = 45^\circ$. The dashed lines in this figure refer to the asymptotic solutions at low as well as high x based on the analysis presented earlier in section 2.2. Clearly, the numerical solution is consistent with the results of the asymptotic analysis, and can be approximated by a simple interpolation formula

$$\frac{\delta_o \epsilon^{1/6} x^{1/2}}{\delta} = \left[1 + \left(\frac{\delta_o \epsilon^{1/6} x^{1/2}}{\delta^* x^{1/3}}\right)^m\right]^{1/m} \tag{3.21}$$

with $m = 2.5$, where the thickness parameters $\delta_o \epsilon^{1/6}$ and δ^* are defined earlier in chapter 2. In view of the predictions of chapter 2, this formula can be readily used to

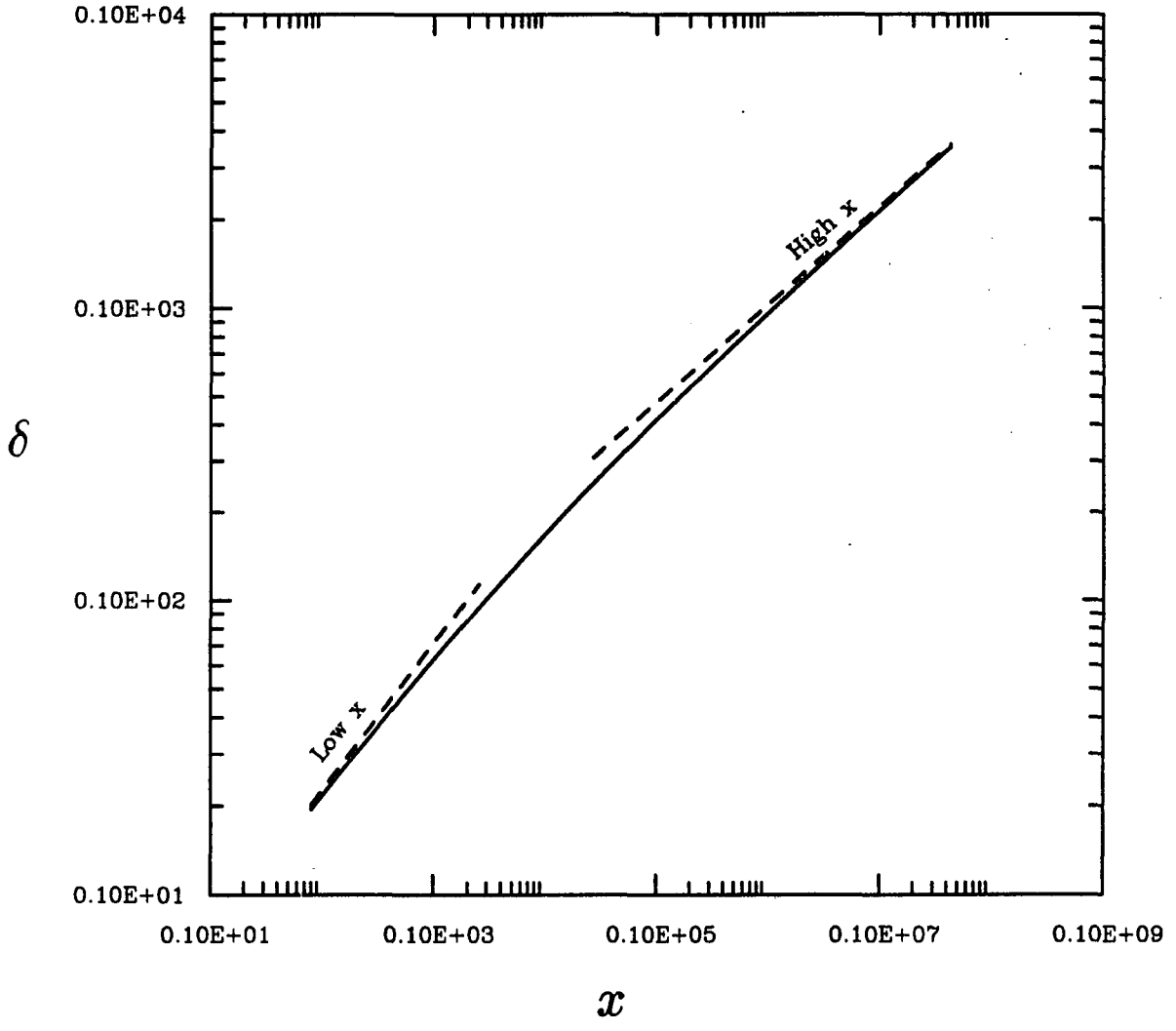

Figure 3.2: The sediment layer thickness δ, as a function of the distance (x) from the leading edge, both rendered dimensionless with the particle radius $\tilde{a}$, along with the corresponding asymptotic solutions for small x and for large x, for $\phi_* = 9.6\%$ and $\theta = 45°$.

obtain the sediment layer thickness δ for intermediate range of x. Moreover, close to the leading edge of the inclined plate the existence of partial slip at the plate exerts a dominant effect and the solution presented in section 2.2.1 can be taken as a good approximation. Far away from the leading edge, however, the slip velocity at the plate becomes small compared to the average bulk velocity within the sediment layer and this in turn leads to a no-slip like velocity profile. This can be seen in figure (3.3) where the scaled longitudinal velocity components, u/u_{max}, within the sediment layer for $x = 20$, 500 & 10^4 is shown plotted as a function of y/δ again for $\phi_s = 10.0\%$ and $\theta = 45^o$.

Another interesting feature of this numerical solution is seen in figures 3.4 and 3.5, which give a qualitative indication of the range of applicability of the small x solution. Clearly, this range in x increases with a decrease in the angle of inclination as well as with a decrease in the feed particle concentration. The reason for this is that, according to the present model, a large particle volume fraction close to the wall is predicted under these conditions, which in turn leads to a large slip coefficient and, consequently, a large slip velocity.

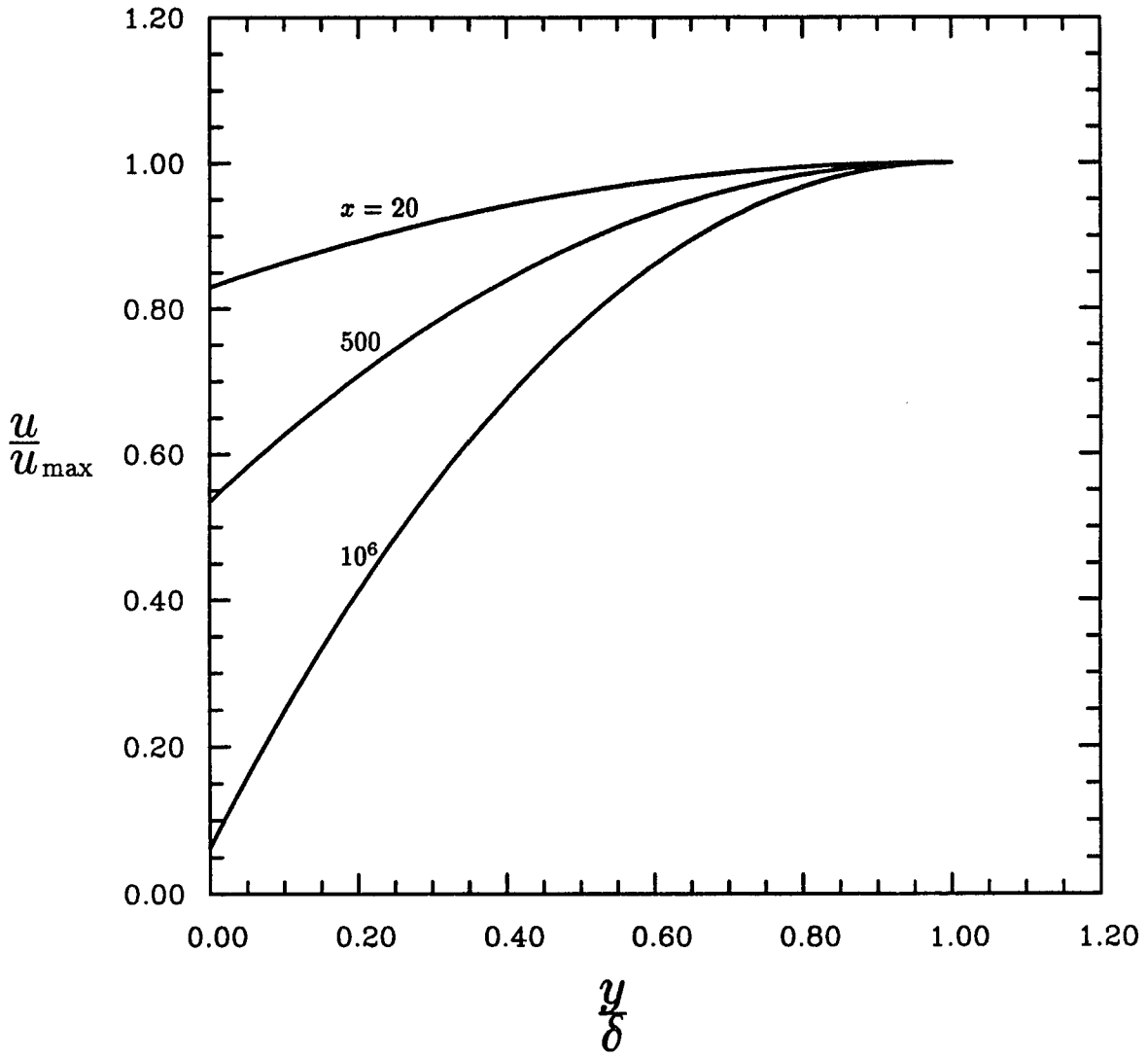

Figure 3.3: The scaled longitudinal velocity component, u/u_{max}, as a function of the scaled variable, y/δ, for $x = 20$, 500 & 10^6, $\phi_s = 0.10$ and $\theta = 45°$.

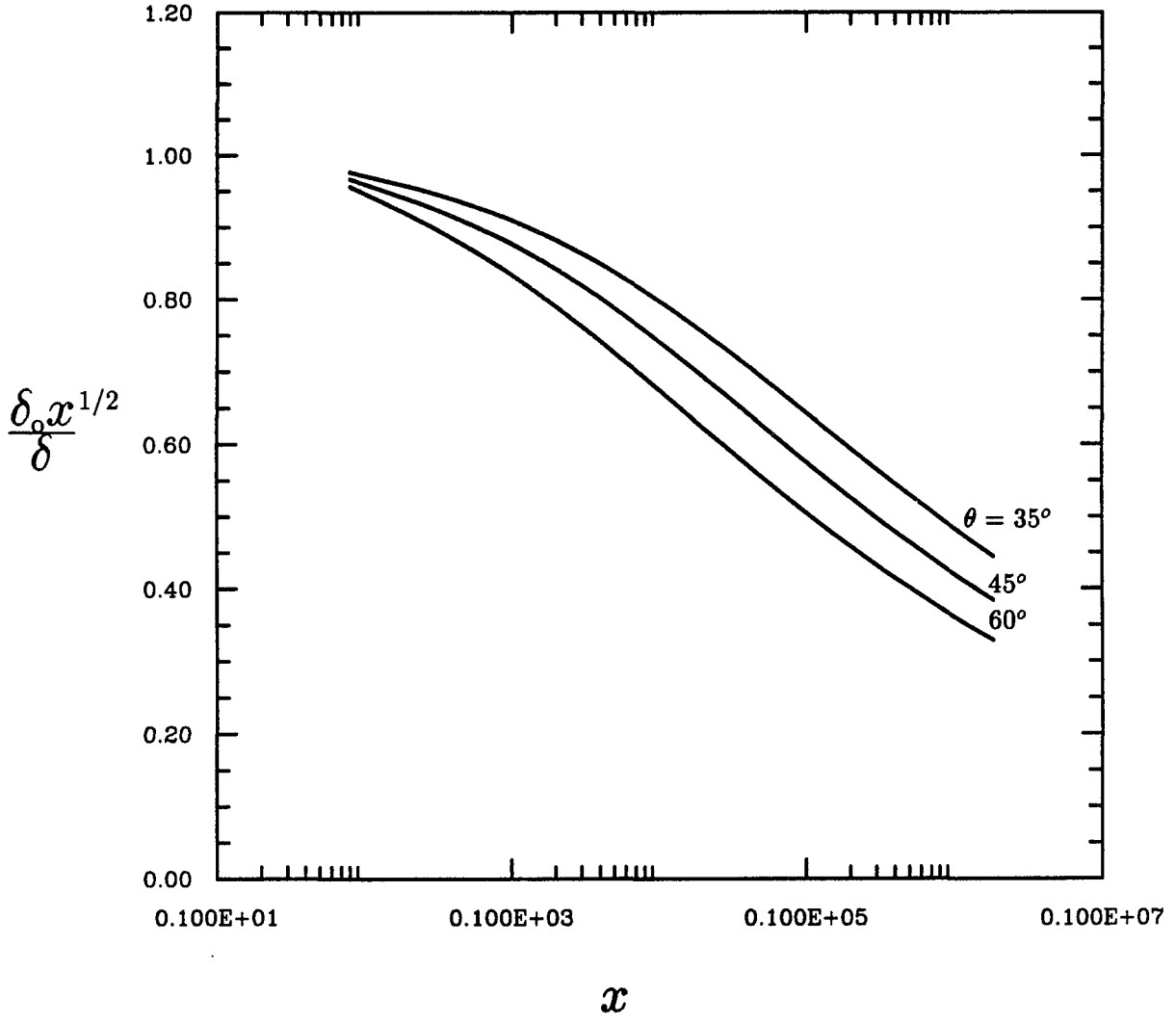

Figure 3.4: Ratio of the sediment layer thickness according to the small x asymptotic solution to the corresponding thickness computed from the numerical solution, as a function of x for $\phi_s = 0.10$ and for $\theta = 35°$, 45° and 60°.

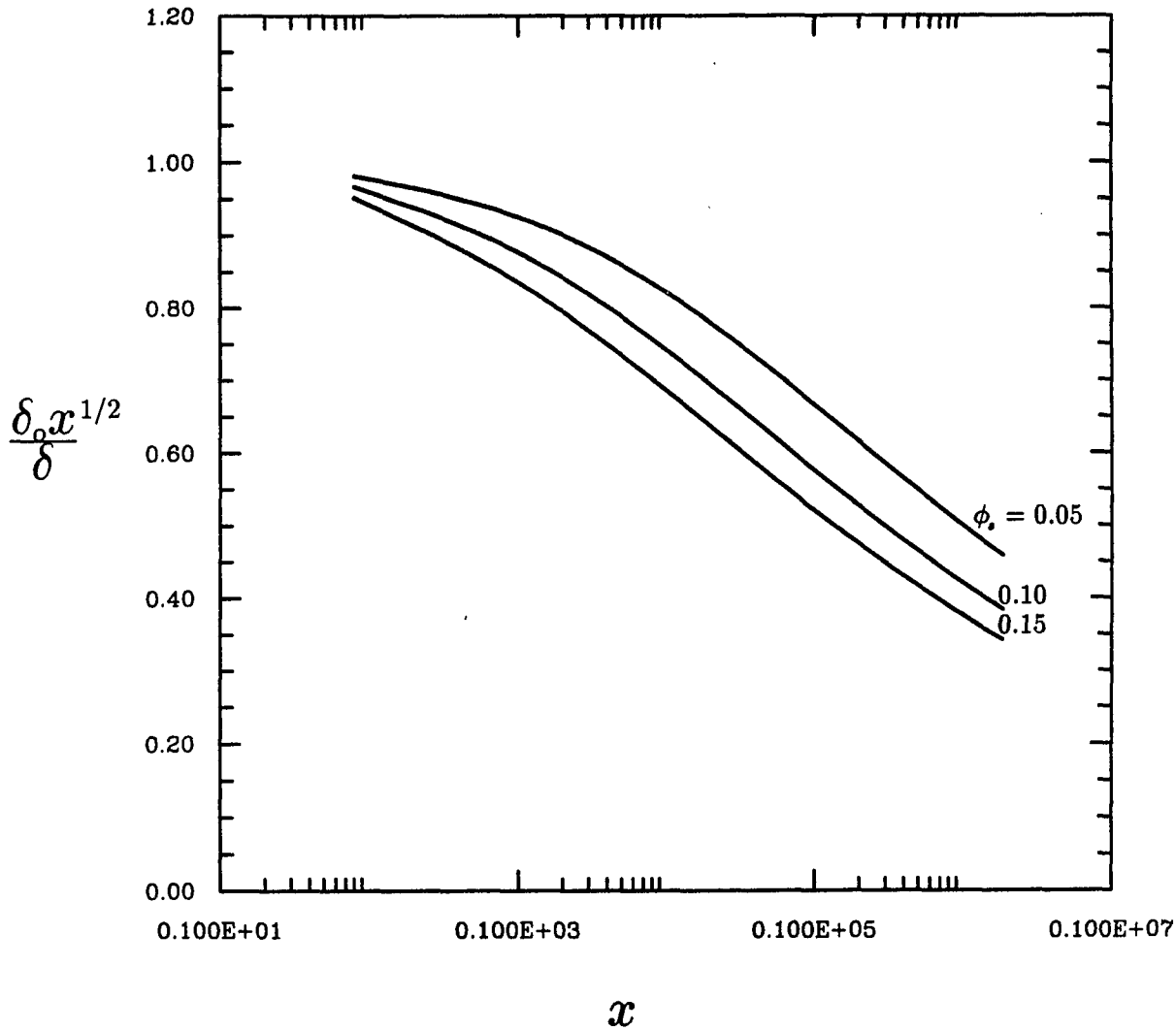

Figure 3.5: Ratio of the sediment layer thickness according to the small x asymptotic solution to the corresponding thickness computed from the exact numerical solution, as a function of x for $\theta = 45°$ and for $\phi_s = 0.05$, 0.1 and 0.15.

Chapter 4

Experimental Investigation

4.1 Introduction

An essential prerequisite for the continuous operation of supersettlers, i.e. settling vessels with inclined walls, is that the sediment layer that forms along an upward facing wall be able to flow freely under the action of gravity. Otherwise, the thickness of this layer will grow steadily in time until, eventually, a steady-state operation can no longer be maintained.

In the preceeding chapter, a theory containing no adjustable parameters was presented for modeling quantitatively the flow structure of this sediment layer which, *interalia*, delineated the conditions under which a steady flow of this sediment layer ccould be sustained. It is the purpose of the present chapter to describe the results of a series of experiments in a "low aspect ratio " vessel which were designed to test the predictions of the theoretical model and thereby asses its reliability for further use.

4.2 Experimental Technique

The complete characterization of the sediment layer requires the determination of its thickness profile, the particle velocity profile, and the corresponding

particle concentration profile. The former is relatively easy to measure experimentally by means of a cathetometer or by employing a video imaging technique. Clearly, such a technique is only applicable to cases in which a good optical contrast exists between the suspension and the sediment. Nevertheless, even if the contrast is weak, various image enhancement techniques have been developed which can be applied to a digitized video image in order to locate the position of the interface. For the fluid particle system used in the present experiments, however, such a refinement was not needed owing to the good visual contrast between the sediment and the suspension, and hence it was found possible to measure the sediment layer thickness manually from a video image within a accuracy of $\sim$0.03 mm.

Unlike the measurement of the sediment layer thickness, however, the determination of the particle velocity and concentration profiles within the flowing concentrated suspension presents a much more difficult challenge and various attempts were made over the years to develop, for this purpose, several non-intrusive experimental techniques. One of the earliest was described by Karnis *et al.* (1966), who employed cinematography to visualize the motion of tracer particles within the flow and thereby were able to estimate the particle velocity and the concentration profiles within concentrated suspensions flowing in a tube. Later on, more sophisticated techniques based on the Doppler effect phenomenon were developed by a number of investigators for measuring particle velocities within such suspensions. For example, McMahon and Parker (1975) used microwave Doppler Anemometry to determine particle velocity profiles in flowing suspensions but, owing to the relatively long wave length of the microwaves, their spatial resolution was extremely poor. This drawback was later overcome by Kowalewski (1980), who employed Ultrasound Doppler Anemometry by approximately matching the acoustic properties of both phases. Unfortunately, Kowalewski could not distinguish between the suspending fluid and particle velocities and thus, was unable to extend his technique in order to measure the local

particle volume fraction. The Laser Doppler Velocimeter was also used by number of researchers (Dybbs 1981; Nouri *etal.*, 1987) to measure particle velocities in suspensions, but, due to the difficulties arising from the presence of optical turbidity, its use was limited to relatively dilute suspensions with concentrations around 10% to 14%. Recently, Koh (1991) and Koh *et al.* (1993) have shown that this LDA technique can be extended to measure particle velocity and concentration profiles in flowing concentrated suspensions by matching the refractive index of the particles with that of the fluid. In this case, the Doppler burst is produced by the slight mismatch in the refractive indices and the non-uniformity present in the medium. This technique yields a relatively good spatial resolution and is easy to implement, however, its applicability to highly concentrated suspensions in the range usually encountered in a sediment layer was not demonstrated by these investigators. Since the limitation of LDA for measuring velocities within concentrated suspensions is due mainly to the optical turbidity of the medium, its use in a particular system strongly depends on the type of fluid and particles being employed and on the length of the traversing beam length within the suspension.

In addition, and in contrast to the case of a flowing pure fluid, the adaptation of LDA to the velocimetry in concentrated suspensions gives rise to several sources of error. First of all, as expected at high particle concentrations, the existence of many particles in the probe volume introduces noise into the scattered signal and may result in erroneous velocity measurements. This error can be reduced by making the measuring volume nearly the same as that of the particle and can also be minimized to some extent by employing an appropriate signal processing technique which discards signals from multiple particles. The second source of error in the measurement of the velocity is due to the changes in the refractive index of the medium encountered by the laser beam. Thus, the resulting wobble of the beam can introduce noise into the velocity signal akin to fictitious turbulence. This source of error, however, cannot

be removed completely since, in practice, a small amount of mismatch always exists even when the refractive indices of the fluid and of the particles are matched in a suspension. In order to obtain a quantitative estimate of this error, the centerline velocity in a suspension with average particle concentration 21% flowing through a rectangular channel was measured at different temperatures. It was found that, under the same flow conditions, the velocity fluctuations depended strongly on the temperature of the suspension and attained their minimum close to a temperature where the refractive indices of both the phases were closely matched. It is probable that the wide scatter reported by Koh (1991) in his velocity measurements can at least partly be attributed to this effect. At any rate, it is clear from what has been said above, that a detailed investigation is required to quantitatively determine the limitations of this technique and to obtain a reliable estimate of the uncertainty in the interpretation of the measurements due to these different sources of errors. Specifically, the error involved in estimating this fictitous turbulent intensity plays a significant role when the measurements are used in studies of turbulent flows or of flows where a very accurate value of the particle velocity fluctuations is desired.

4.3 Experimental Setup

The flow system in which the sedimentation experiment was performed was similar to that one used earlier by Borhan (1987) to study the flow stability in super settlers.

The experimental set up used, shown schematically in figure 4.1, consisted of a settling vessel connected to the flow system mounted on a pivoting stand so that it could be rotated to the desired angle of inclination. A Laser Doppler Anemometer and a video camera for measuring the particle velocities and the sediment layer thickness respectively, was attached to a $x - y - z$ table, which was fixed to the same pivoting shaft that was holding the settling vessel. The table had the maximum travel range

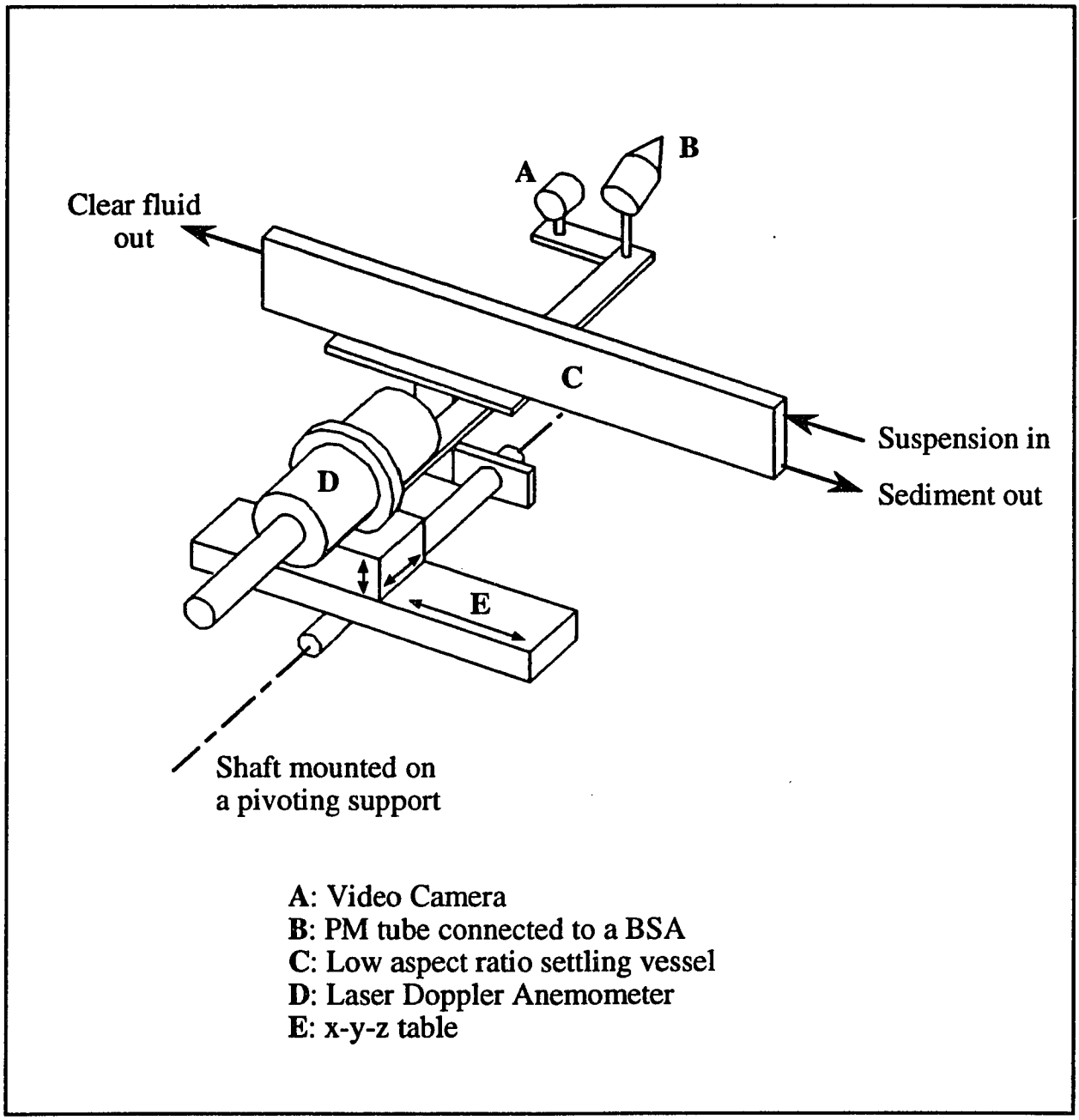

Figure 4.1: Schematic description of the experimental setup.

of 12", 4" and 2.5" in the x, y and z directions respectively with a resolution of 10 microns in all the three directions. Figure 4.2 shows the detailed dimensions of the settling vessel, made of a colorless anodized aluminium frame on which a clear glass window was glued on both of its sides. Of the two ports located on the lower side of the vessel, the top was connected to a centrifugal pump for feeding the suspension while the other was used to withdraw the sediment by means of a Cole-Parmer peristaltic pump. Near the top of the vessel, one of the two ports was connected to the mixing tank and was used to remove the overflow product while the other was kept plugged during the experiments and was opened only when the vessel was being cleaned.

The details of the flow system are shown schematically in figure 4.3. Due to the corrosive nature of the fluid mixture employed in our experiments, Viton tubing (3/8" I.D.) was used for all connections involving the transport of the suspension and the suspending fluid. In addition, in order to minimize the pulsation caused by the peristaltic pump at the sediment withdrawal port, an expansion chamber was placed before the inlet to the pump. The overflow product and the sediment that were withdrawn from the vessel were eventually remixed in the mixing chamber which was equipped with a mechanical stirrer and with cooling coils to maintain a constant temperature. The temperature of the suspension in the mixing tank was monitored by means of a thermistor probe and was controlled manually by changing the set point of the temperature of the water within the circulator bath which circulated through the cooling coils of the mixing tank. The rate of the overflow product at the top of the vessel was measured using a Cole-Parmer flowmeter.

The volumetric concentration of the particles in the feed was determined by measuring, using a photodiode, the intensity of a laser beam passing through the suspension flowing in a cell. The laser employed for this purpose was a 1mW He-Ne laser. The particle concentration was then calculated from the well known Beer's law which, in this case, takes the form

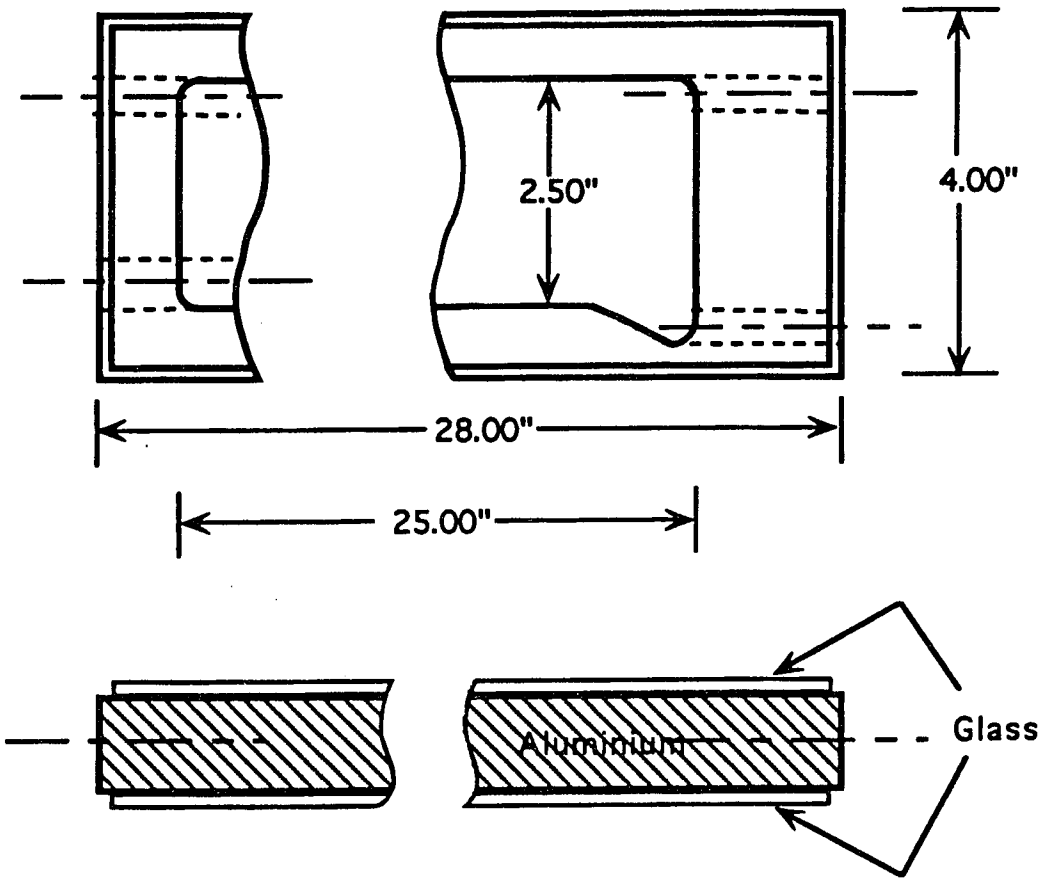

Figure 4.2: Schematic diagram of the settling vessel (not to scale).

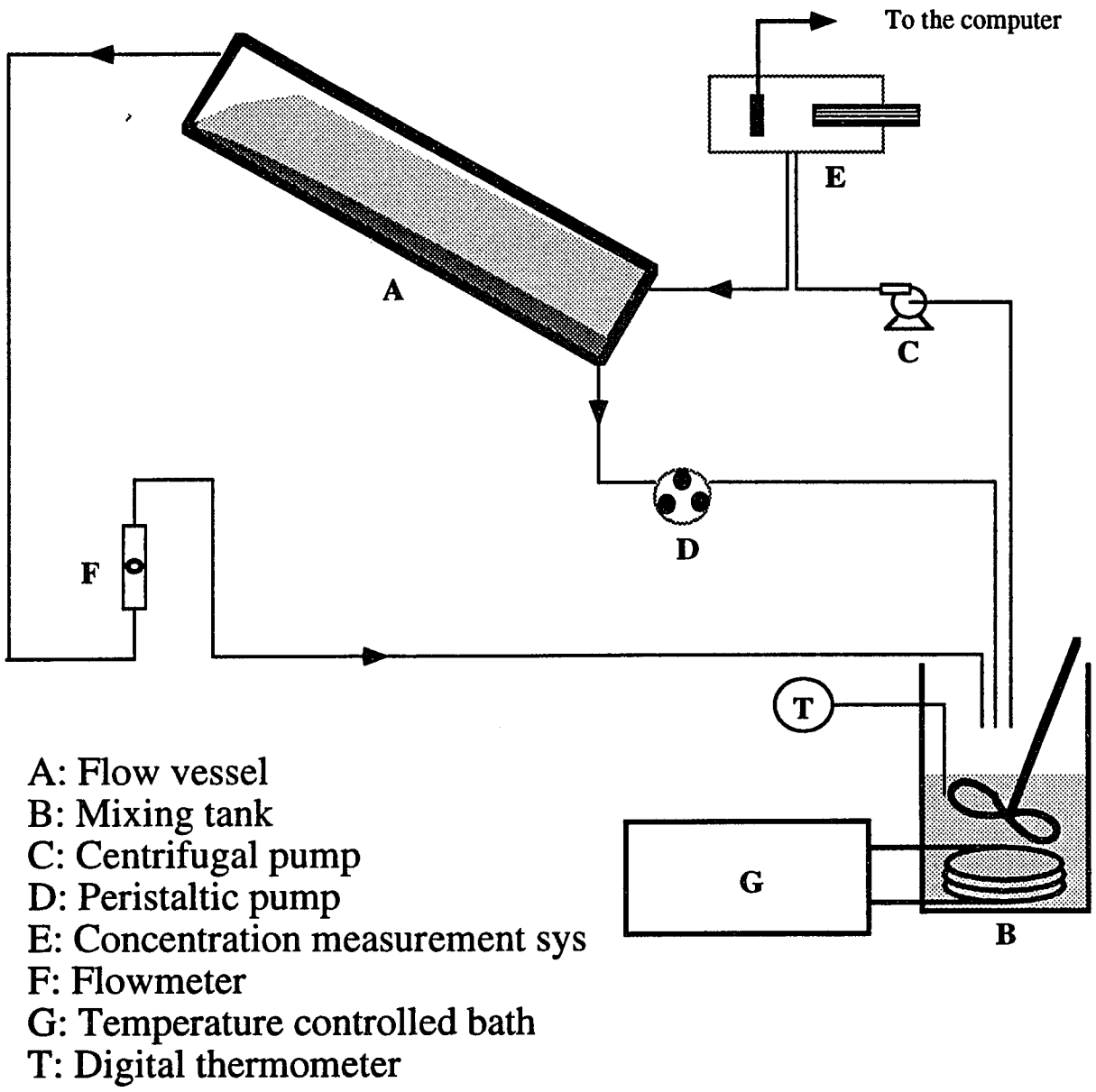

Figure 4.3: Schematic representation of the flow system.

$$I_T = I_0 \exp(-k\phi_s L) \tag{4.1}$$

where I_T is the intensity of the laser beam being transmitted through the cell, I_0 is the transmitted intensity in the absence of particles, k is the so-called extinction coefficient, and L is the length of the optical path inside the suspension of particle concentration ϕ_s. The value of the coefficient, k, was determined by a calibration experiment which was performed in the same cell with a suspension of known particle concentration. The Laser Doppler Anemometer used for the particle velocity measurements was a one dimensional system equipped with a 15 mw He-Ne laser. It was used in the off-axis forward scatterring mode in order to maximize the signal to noise ratio of the scattered signal. The optics for this system were obtained from Dantec and are shown schematically in figure 4.4 where each of its major components is described in the accompanying legend. As shown in this figure, the incoming laser beam was first directed through a beam splitter where it was divided into two beams of equal intensity. One of the beams was then made to pass through a Bragg cell, which shifted its frequency by 40 MHz. The exit beams then entered the Beam Translator module which was used to adjust the separation between the beams. In order to render the size of the measuring volume close to that of the particles, a Beam Expander was placed after the Beam Translator module. The final element before the beams entered the flow system consisted of a plano-convex lens (also referred to as a front lens) with a focal length of 80 mm, which served to focus the two beams onto the same point in space, thereby, forming the measuring volume. During the experiments, the beam separation was 40.5 mm, which created a measuring volume of size $d_x = 41$ μm, $d_y = 41$ μm and $d_z = 249$ μm. A set of close-up lenses connected to a photo multiplier tube termed PM optics by Dantec, was placed in the forward direction as shown in the figure and was used for focusing the collected light into a PM tube through a pinhole. In addition, the PM optics also had an adjustable

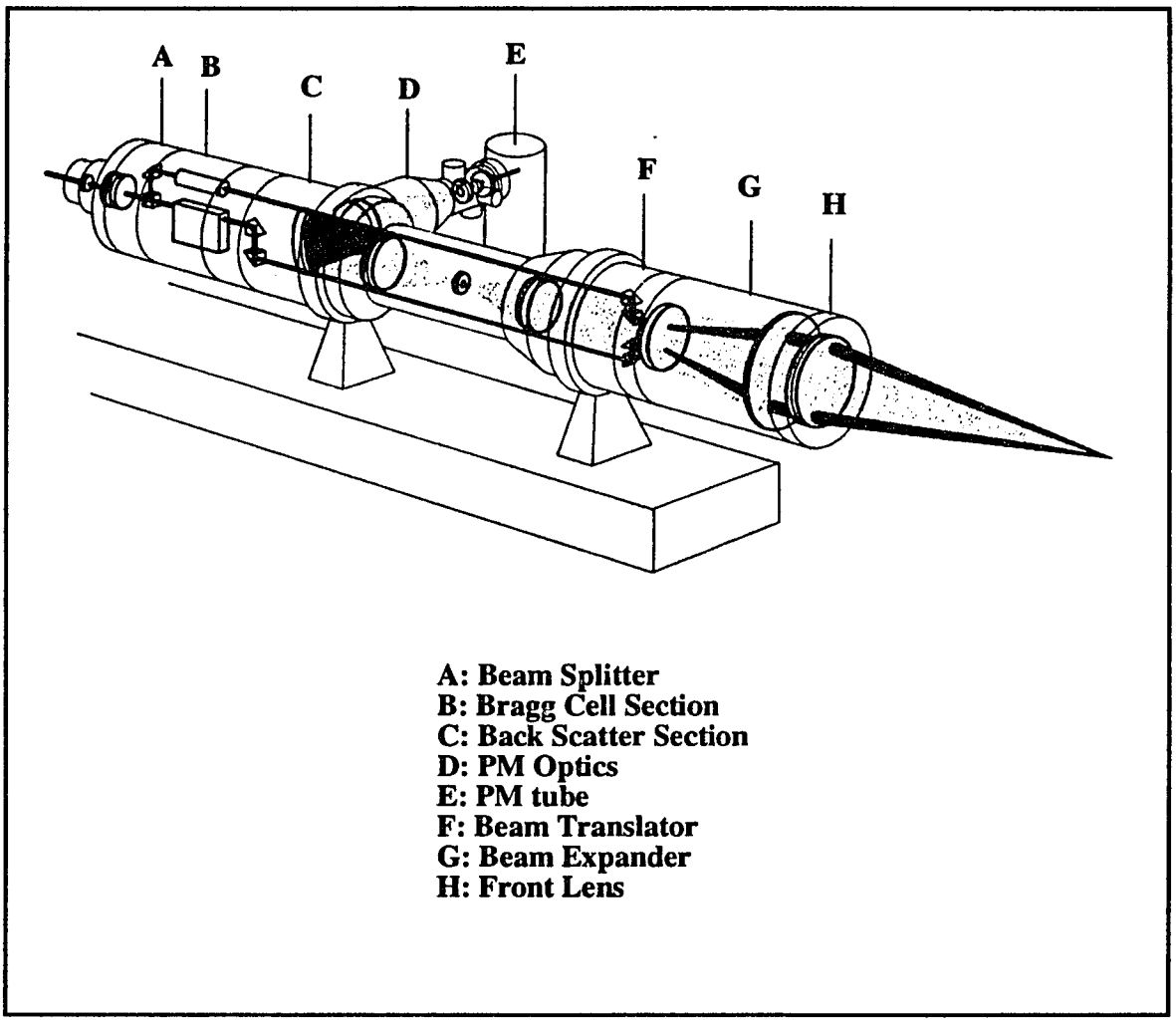

Figure 4.4: The optical layout of a typical Dantec Laser Doppler Anemometer.

pinhole disc on which the image of an object placed at a distance of 80 mm to infinity could be observed and focused via an eye piece.

The output of the PM tube was connected to an on-line processor with a built-in FFT chip, developed by Dantec Electronics and called Burst Spectrum Analyzer (BSA). This BSA employed an advanced burst detection scheme to accurately find and validate the burst and was capable of processing signals with a signal-to-noise ratio as low as -6 dB. A personal computer was interfaced by IEEE488 with the BSA to obtain the data, which consisted of the velocity, the transit time and the arrival time of each burst processed. The data were stored in the computer and were analyzed at the end of an experiment to obtain the particle velocity distribution at each point.

In addition, a video system, consisting of a video camera (Sony XC77RR) along with a VCR (Panasonic AG1960) and a Sony monitor, was attached to the experimental system in order to visually observe and measure the thickness of the steady flowing sediment layer. The latter was done manually from the monitor which reproduced the image of the sediment layer magnified 35 times its actual size.

4.4 Experimental Procedure

This section, which can be divided into the following sub-sections, describes the details of the experimental operation.

4.4.1 Refractive Index Matching

There are several factors which affect the optical quality of the suspensions viz. the refractive indices of the two phases, the optical quality of the particles and the impurities and non uniformity present in the solid phase. Furthermore, the proposed theoretical model also requires that the particles be spherical and monodisperse.

These restrictions posed a major constraint in choosing the appropriate fluid-particle system for the experiments. However, in the present case, a careful inspection of the variety of polymer and resin samples from different manufacturers led us to choose a class of PMMA beads (CA603) manufactured by ICI, which were found to contain only a very small number of air bubbles and hence, were most suited for our applications. These particles were spherical but, owing to their wide size distribution, had to be sieved. Figure 4.5 shows a typical particle size distribution that was achieved after the sieving process. The density of these particles was found to be 1.178 gm/cm^3. For PMMA the refractive index is approximately 1.491, however, the actual RI of the particles used in our experiments, an important parameter for the refractive index matching, was not available from the manufacturer. Following Koh (1991), who presented a number of methods available to date for RI matching, a systematic procedure was adopted for matching the refractive index of the particles with that of the suspending fluid which did not require that the RI of the particles prior to matching be known precisely. Essentially, this method was based on the principle that, for a given wave length, the maximum transmittance of the suspension is reached when the refractive indices of both the phases are closely matched. Clearly, this is possible in practice only where the suspending fluid is prepared by mixing two or more fluids so that its refractive index can be changed by varying its composition. A mixture of turpentine and tetralin was therefore chosen and its proper composition was arrived at by maximizing the transmittance of the suspension. The physical properties of the fluid-particle system used is given in table 4.1.

Figure 4.6 shows the schematic diagram of the experiment that was used to measure the transmittance of the suspensions. It involved a suspension being circulated through a glass cell (optical path length= 25.5 mm) and kept in a tempering beaker equipped with a magnetic stirrer. The flow rate of the circulating pump was adjusted to prevent any settling of the particles in the tube or in the glass

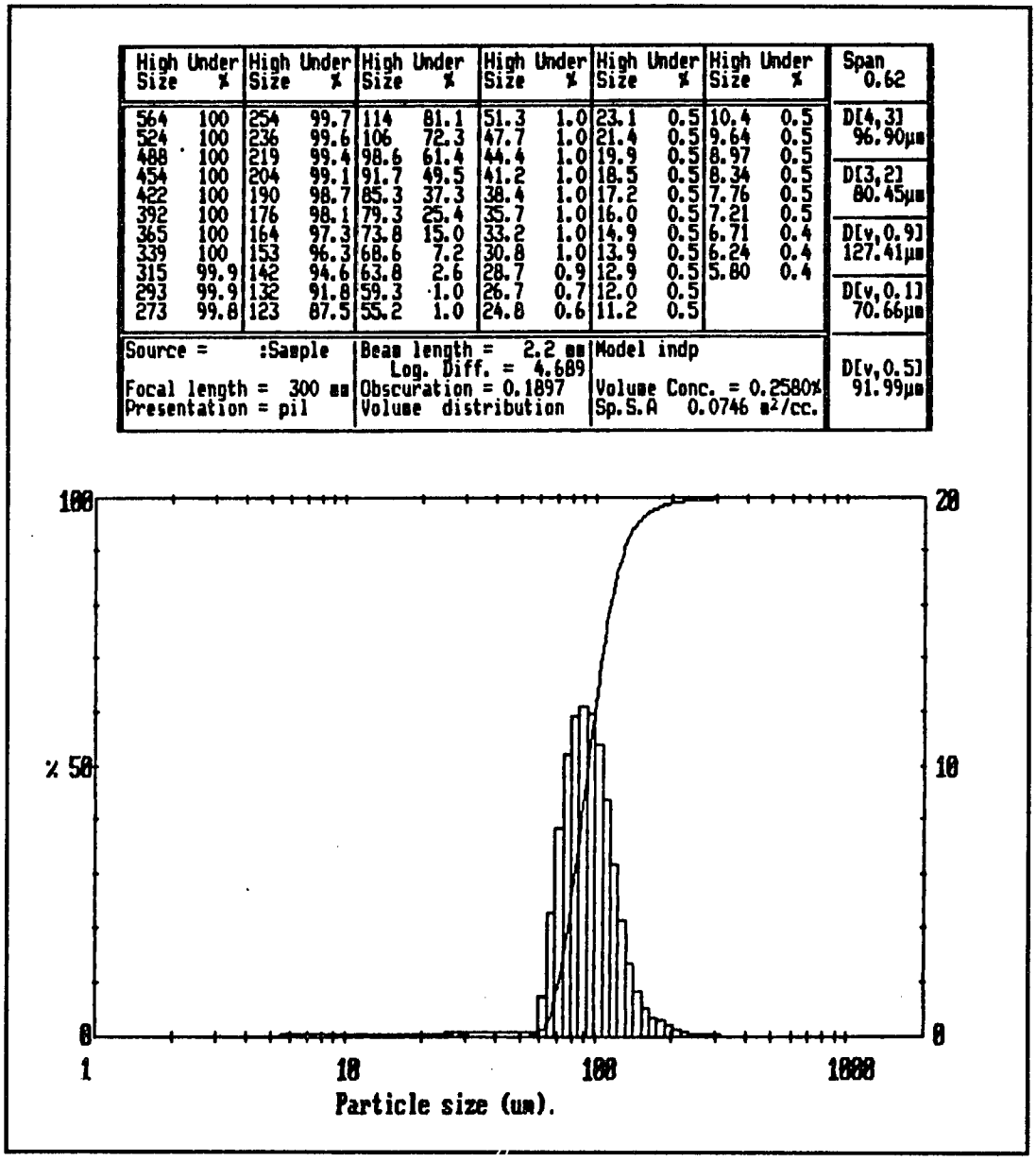

Figure 4.5: A typical particle size distribution curve for the particles used.

	Density (gm/cm^3)	Viscosity (cp)	Refractive Index at $24°C$
Turpentine	0.85	1.43	1.4636
Tetraline	0.97	2.01	1.5388
Suspending fluid, mixture of 62.9 % turpentine and 37.1 % tetralin	0.89	1.47	1.4908
Particles, Acrylic, average diameter 90 μm	1.18	-	1.491

Table 4.1: Physical properties of the fluid and particles used.

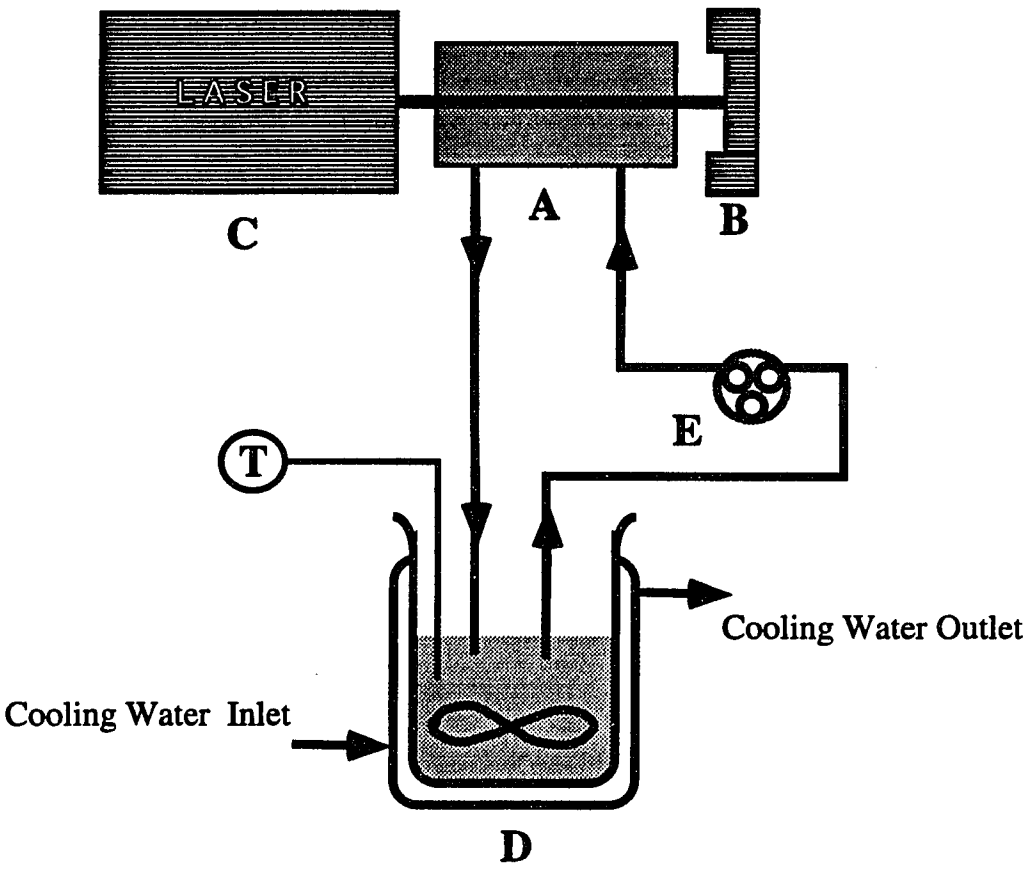

A- Flow Cell
B- Photodiode (Detector)
C- He-Ne Laser
D- Tempering beaker with magnetic stirrer
E- Cole-Parmer peristaltic pump
T- Digital thermometer

Figure 4.6: Schematic representation of the transmittance measurement system.

cell. Moreover, since the refractive indices of both phases depend strongly on the temperature, it was necessary that the RI matching experiment as well as all the other experiments be performed at the same temperature. The measured transmittance for the suspension containing 2.0% particles by volume is shown in figure 4.7 plotted against the refractive index of the suspending solution. It is clear from this figure that the maximum value of the transmittance occurs at a refractive index equal to 1.4908 which is close to the RI of the PMMA polymer. As pointed out by Koh (1991) and also found out during our experiments, it is essential that temperature control be maintained; however, in practice, control to within 1°C was found to be sufficient for our purposes.

4.4.2 Concentration Measurement System

Since the experiments were performed in a closed system, even a slight change in the pump flow rate affected the feed particle concentration. Thus, it was imperative to develop a system which could provide an on line measurement of the particle concentration in the feed. In our experiments, this was realized by measuring the transmittance of the suspension flowing into the vessel and then determining the particle concentration by means of Beer's law, eq (4.1). The flow system used to obtain the constant k was similar to that employed for the refractive index matching. Figure 4.8 shows the experimentally measured transmittance for various suspensions having known particle concentrations. The slope of the straight line in this figure gives the constant k which results in the following relation for the particle concentration

$$\ln\left(\frac{I}{I_0}\right) = -0.27\phi - 1.03 \times 10^{-2} \quad \text{for} \quad 0.03 \leq \phi \leq 0.16 \tag{4.2}$$

It should be added here that, because of the requirement that the indices of refraction be matched, the above expression holds only at the temperature at which the

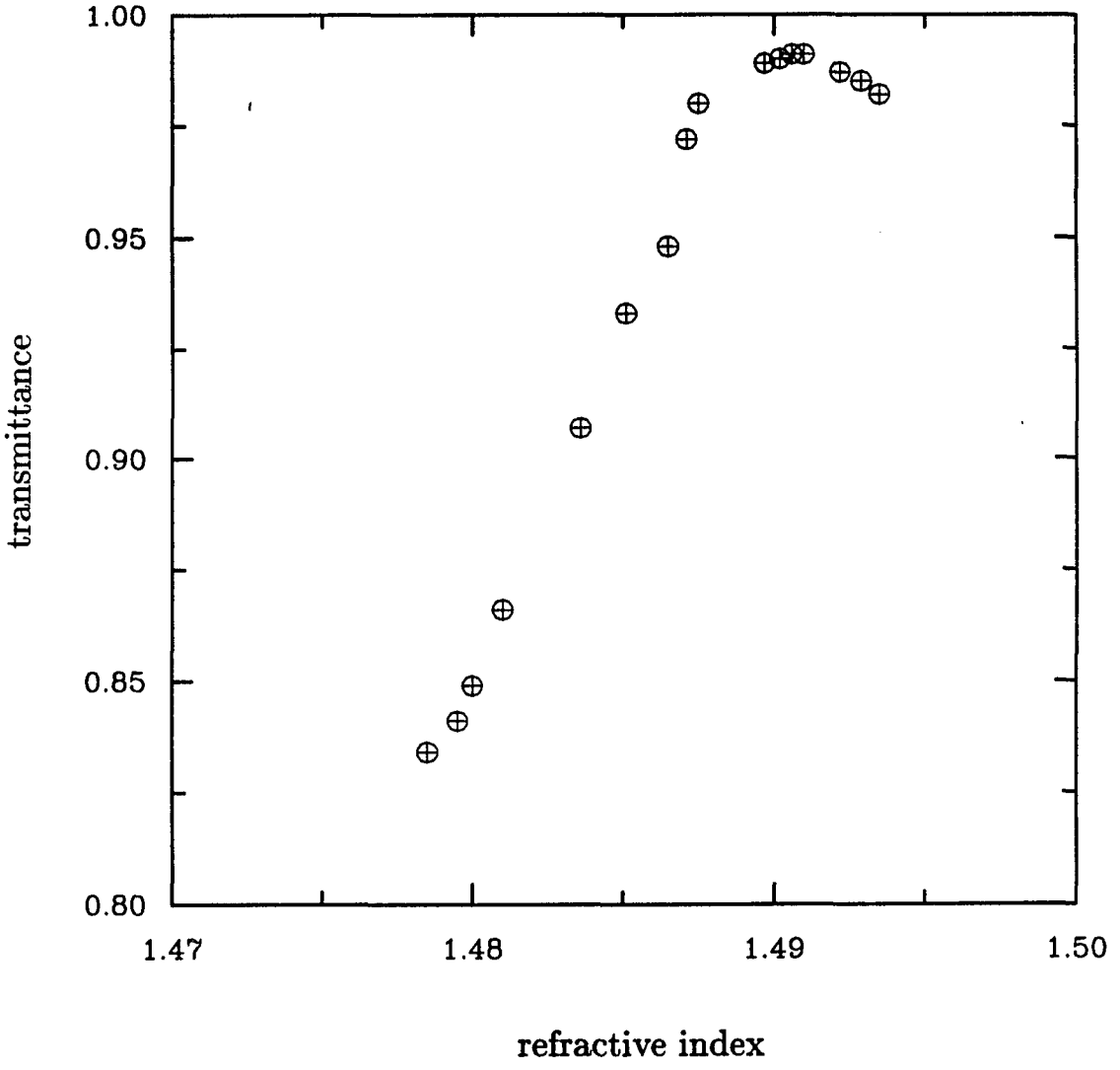

Figure 4.7: Experimental data showing the transmittance curve for a suspension containing 2% particles by volume.

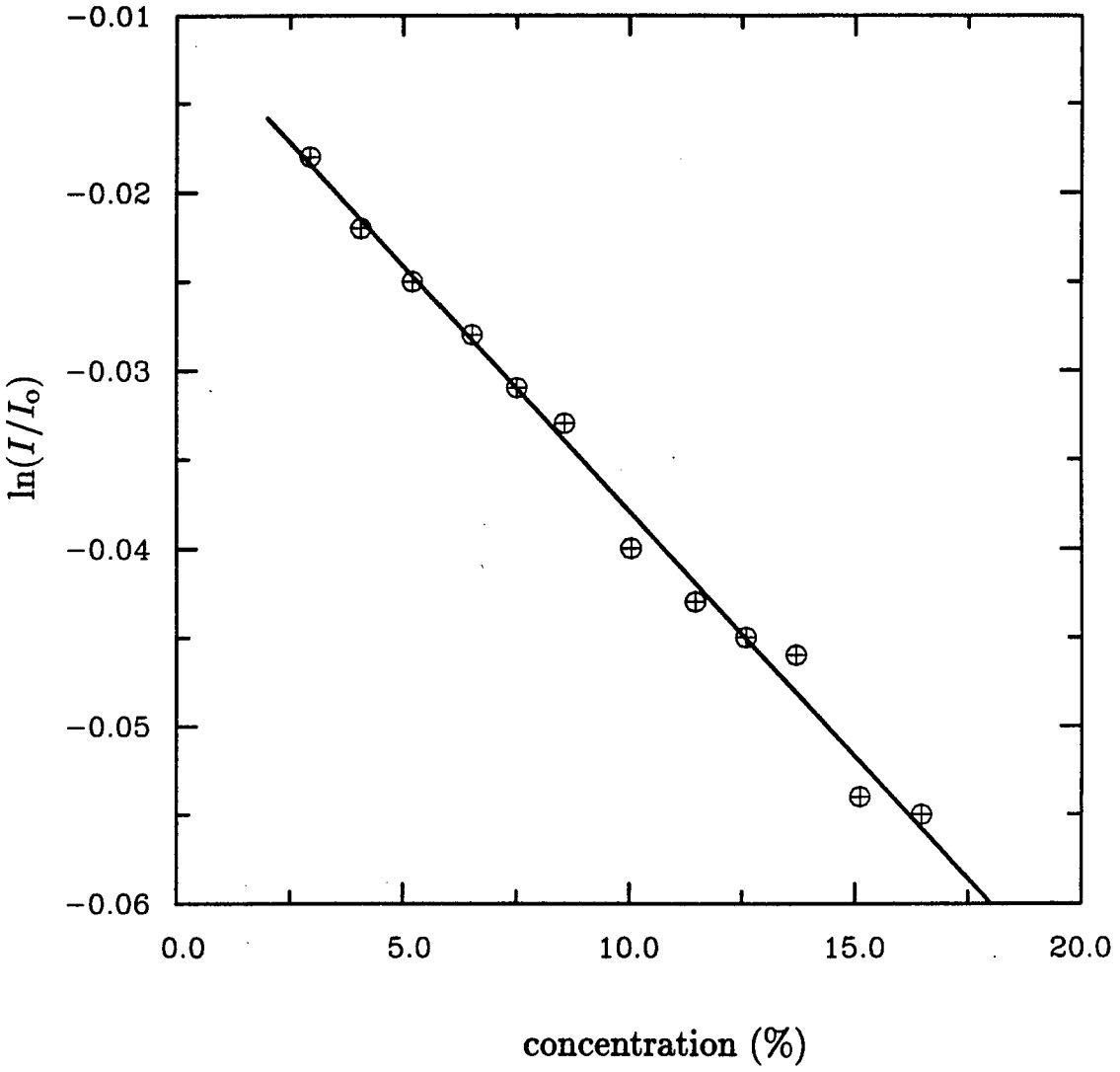

Figure 4.8: Experimentally measured transmittance data for various particle concentrations at 24°C. The solid line represents the best line fit given by equation (4.2).

calibration experiment was performed i.e. at 24°C.

4.4.3 The Flow System

As described earlier in section 3.2, a steady flow of a sediment layer was created by performing a Boycott effect experiment on a low aspect ratio vessel in a continuous mode. First of all, before starting the experiment, the whole system, shown schematically in figure 4.1, was tilted to the desired angle of inclination. The flow channel and the $x-y-z$ table was then aligned in a way such that the co-ordinate system of the table and of the vessel coincided. The set-screw mounted on the LDA was also adjusted to render the axis of the beam perpendicular to the direction of the flow. For a typical experiment, a fluid of refractive index 1.4908 at 24°C was first prepared by mixing 62.9% by volume of turpentine with 37.1% by volume of tetralin. Our flow system required approximately 3.0 liters of suspending fluid for the experiment. The fluid thus prepared was then transferred to the mixing tank of the flow system (shown in fig 4.3). At first, only the pure fluid was circulated through the flow system using the centrifugal pump. Also, the temperature of the cooling water circulating through the coils in the mixing tank was adjusted manually to maintain a constant temperature of 24°C in the suspending fluid. Due to the fact that, during the experiments, the temperature was controlled only manually, it was essential that a constant temperature be maintained inside the laboratory.

A measured amount of particles was then added slowly to the mixing tank and the flow rate of the sediment withdrawal pump was regulated so as to avoid any accumulation of the sediment in the collection bank of the vessel. Finally, the flow rate of the feed pump was adjusted in order that the leading edge of the sediment layer be made to coincide with the uppermost boundary of the upward facing surface of the vessel. This step was extremely difficult to perform as it was not easy to see the suspension-clear fluid interface. After the flow rates were set, the system was

found to reach its steady state within a few minutes, as verified by measuring the sediment layer thickness and the average particle velocity at some fixed location. Also, during the course of the experiments, the flow rate of the clear fluid was monitored continuously and, if found to be constant, this provided further evidence that the system had reached steady state.

4.4.4 Measurements and Data Acquisition

Once steady state was established, measurements at different points in the flow field were performed by sliding the $x-y-z$ table, on which the LDA equipment was mounted, to the desired location, and 1000 doppler bursts were processed. The processed information, which contained the velocity, the transit time and the arrival time of each burst, was next transferred to a personal computer for storage. A simple computer program was then used to calculate the average velocity using the expression

$$< u >= \frac{\sum_{i=1}^{N} u_i}{N} \tag{4.3}$$

where N is the total number of bursts processed and u_i denotes the velocity evaluated from the i^{th} burst. In turn, the number of scattering centers per unit length can easily be evaluated from

$$B = \frac{N}{< u > T} \tag{4.4}$$

where B is the number of bursts or scattering centers per unit length and T represents the total time taken by N scattering centers (or number of bursts) to cross the measuring volume. On the other hand, in order to measure the sediment layer thickness, the camera mounted on the $x-y-z$ table was made to translate in the x direction from 0 to approximately 250 mm along the upward facing wall and, points on the sediment-suspension interface corresponding to 10 mm intervals on the upward

facing wall were marked manually on a transparency from the television monitor. The distances between these points from the edge of the upward facing wall which was marked on the transparency as a straight line were then measured and divided by the appropriate magnification factor of the system, which was close to 35 for the set up used in our experiments.

In the present work, the experiments were perfomed for four feed particles concentrations and two angles of inclinations. The results of these eight set of experiments along with the corresponding theoretical predictions are presented in the following chapter.

Chapter 5

Comparison with the Theory

As was described earlier, the sediment layer thickness was measured both visually as well as by means of a Laser Doppler Anemometer. Figure 5.1 depicts a section of the sediment layer taken by the video camera. The markings on this photograph show the number of bursts per unit length, B, as defined by expression (4.4), and measured independently by the LDA, which qualitatively give some indication of the particle concentration. Unfortunately, the expression quantitatively relating B to the actual local volume fraction of the particles is unavailable and needs to be derived. It is clear from this figure, however, that the measured particle velocity attains its maximum value close to the point which corresponds to the visually observed sediment-suspension interface. Also, seen in this figure is a sharp change in the light intensity at the interface, thereby suggesting that the particle concentration also undergoes an abrupt change in this region.

In the present work, experiments were performed for four feed particle concentrations and for two angles of inclination and the measured sediment layer thickness profiles and some typical particle velocity profiles for each of these cases were compared with the corresponding theoretical predictions based on the theory presented in chapters two & three. Figures 5.2 to 5.6 show the experimentally measured

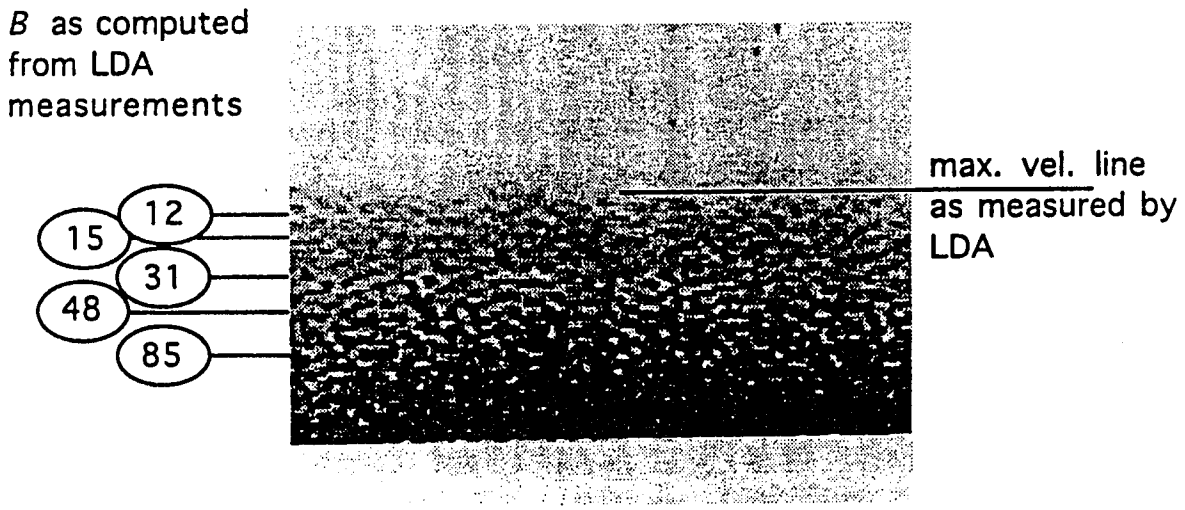

Figure 5.1: A video image of a section of the sediment layer depicting the sharp change in the particle volume fraction across the sediment-suspension interface.

sediment layer thickness profiles along with the corresponding theoretical predictions based on the solution presented in the chapter three which are depicted as solid lines. Clearly, there is a good agreement between the theory and experiments for most of these cases. It should be noted that most of the experiment data shown here are for $x < 230$ mm, primarily because the visual identification of the interface became difficult at large x due to the high velocity of the particles. The corresponding predictions of the no-slip theory by Nir and Acrivos (1990) are not shown in these figures, however, as they exceed the measured thicknesses by more than 150%.

The particle velocity profiles for various feed particle concentrations and x - locations are shown in figures 5.7 to 5.18 which also contain plots of the corresponding theoretical predictions for the particle concentration profile. Unfortunately, due to our inability to measure particle concentrations, the latter could not be compared with experiments. A solid line in these plots represents the theoretically predicted velocity profiles, while the dashed line refers the corresponding predictions based on the no-slip theory of Nir and Acrivos (1990) modified to include the effects of shear induced diffusion due to shear stress gradients. By comparing the two sets of figures 5.2-5.6 and 5.7-5.18, it seems that, as predicted theoretically, the location of the maximum in the measured velocity profile almost coincides with the location of the sediment-suspension interface as determined optically. Also, the velocity profiles in these figures clearly point to the existence of a slip velocity close to the inclined plate, which is consistent with the visual observations made during the preliminary experiments reported earlier in chapter 1. It was not possible, however, to measure the particle velocities any closer than 0.25 mm from the plate due to the saturation of the PM tube current caused by the presence of excessive reflections from the wall. In fact, this is one of the reasons which contributed to the large scatter in the particle velocities measured close to the wall. Furthermore, the low values of these velocities also made it difficult to separate the actual signal from the noise that might have been

present due to external vibrations and the optical turbidity of the medium. Therefore, in order to avoid these spurious signals, most of the velocity profiles were measured at a distance far away from the origin i.e. $x > 180$ mm, where the sediment layer was relatively thick and the particle velocities relatively high. It should be noted at this point that, although all the velocity data shown in figures 5.7 - 5.18 correspond to particle velocities measured within the sediment layer, owing to the relatively small magnitude of the settling velocity and therefore of the slip velocity of the particles relative to the bulk,the data also depict, for all practical purposes, the bulk velocities within the sediment layer.

Figures 5.7 - 5.18 contain a complete summary of all the velocity measurements that were performed within the sediment layer and clearly show that a strong velocity gradient exists within the sediment layer, especially, for higher values of the feed particle concentration and large angles of inclination (c.f figs 5.11 & 5.18, fig 5.15 & fig 5.16). Another interesting feature of these profiles is that almost all the plots are linear over the entire range of the sediment layer except for a small region close to the interface where the velocity attains its maximum value. In view of the momentum balance equation (2.29), this implies the existence of a nonuniform particle concentration distribution within the sediment layer with concentration gradients of the order $\left(\frac{d\lambda}{d\phi}\right)^{-1}$. Clearly, in view of (2.49), this is very small for most of the cases shown in these figures since ϕ is close to ϕ_m under these conditions.

The main conclusion to be drawn from this comparison is that there is surprisingly close agreement between the experiments and the theory, especially considering that the latter did not entail the use of any adjustable parameters.

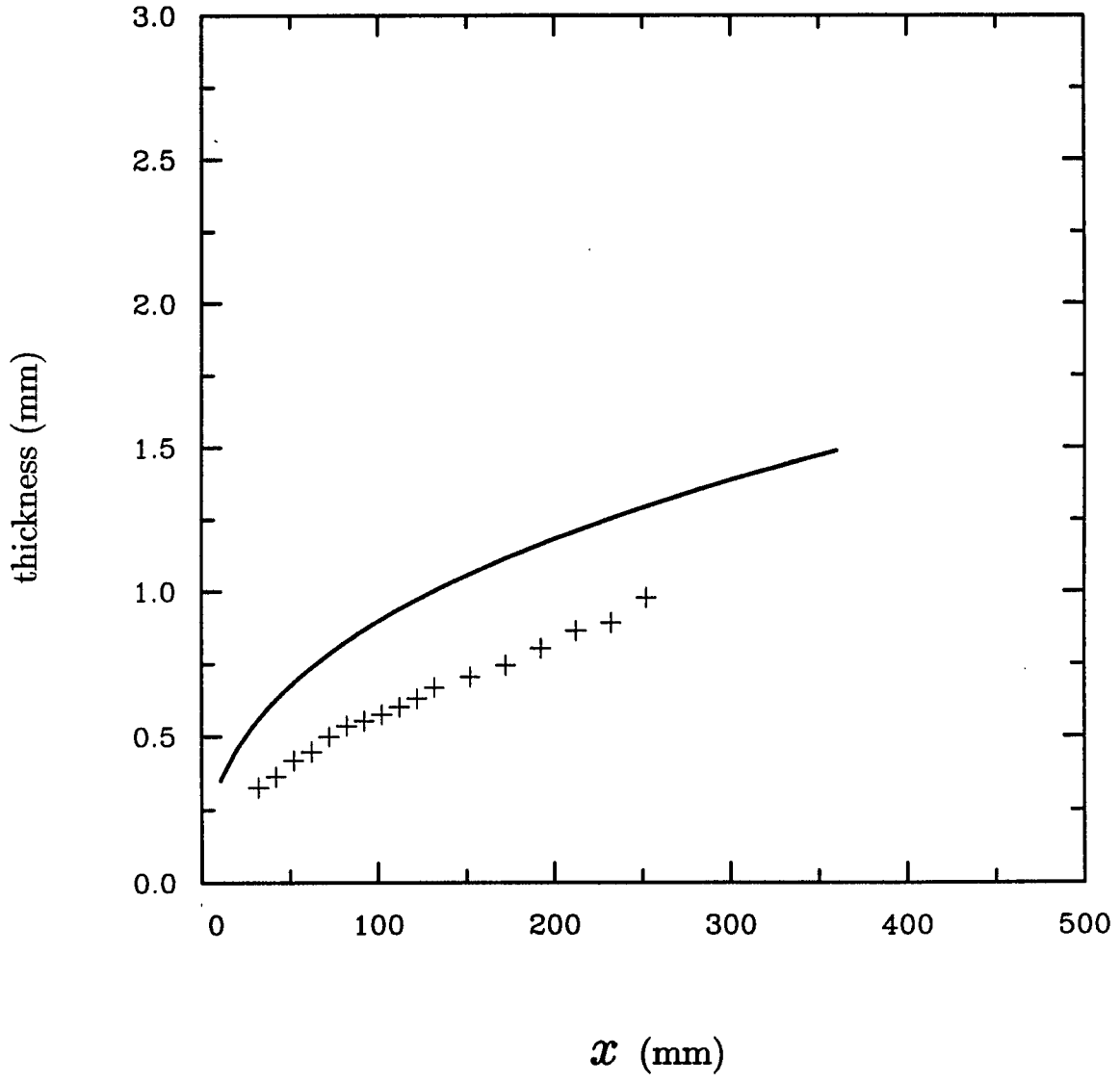

Figure 5.2: Sediment layer thickness profile for $\phi_s = 6.5\%$ and $\theta = 45°$. —— theory; + - experimental points.

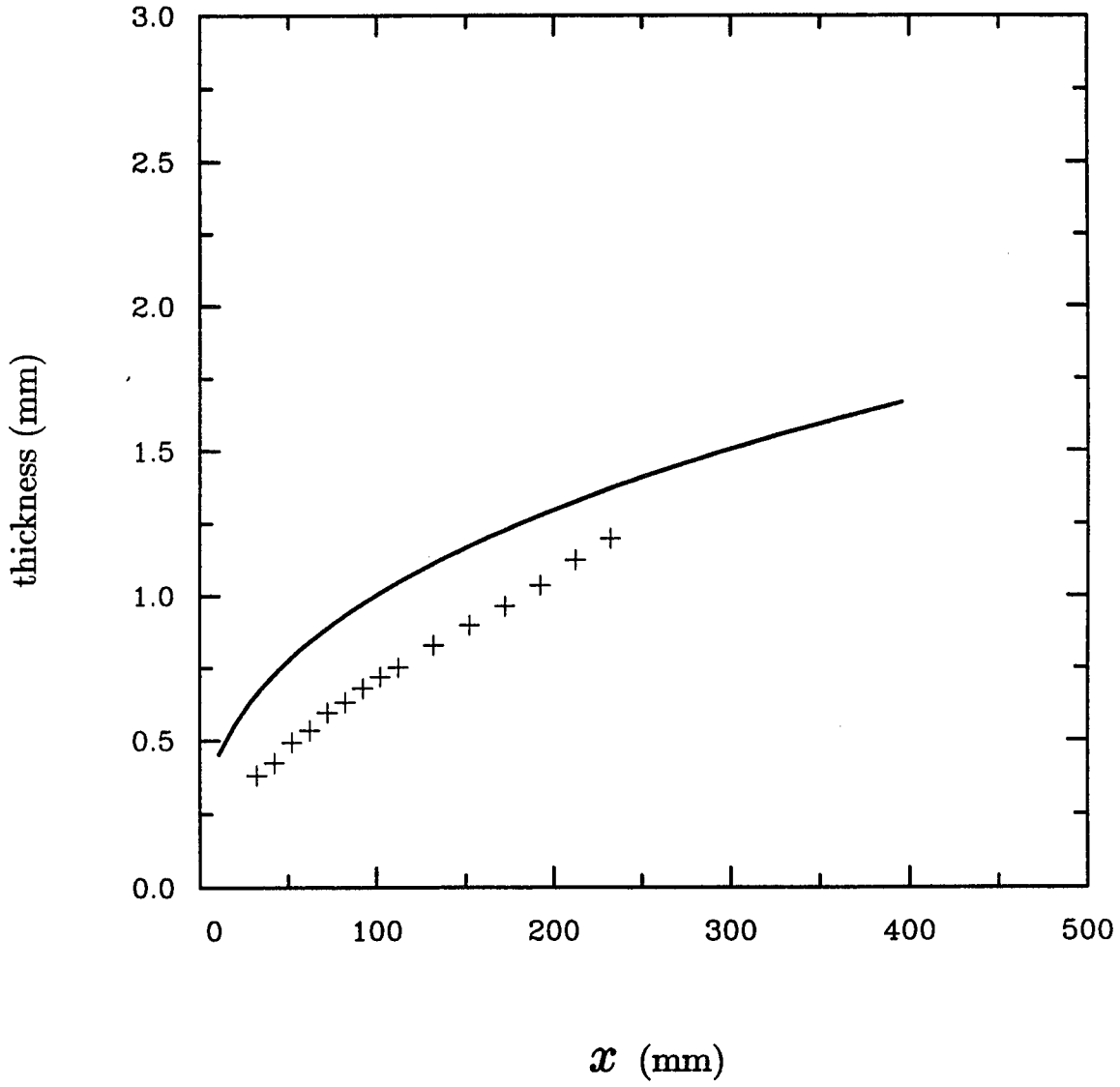

Figure 5.3: Sediment layer thickness profile for $\phi_s = 9.6$ % and $\theta = 45°$. —— theory; + - experimental points.

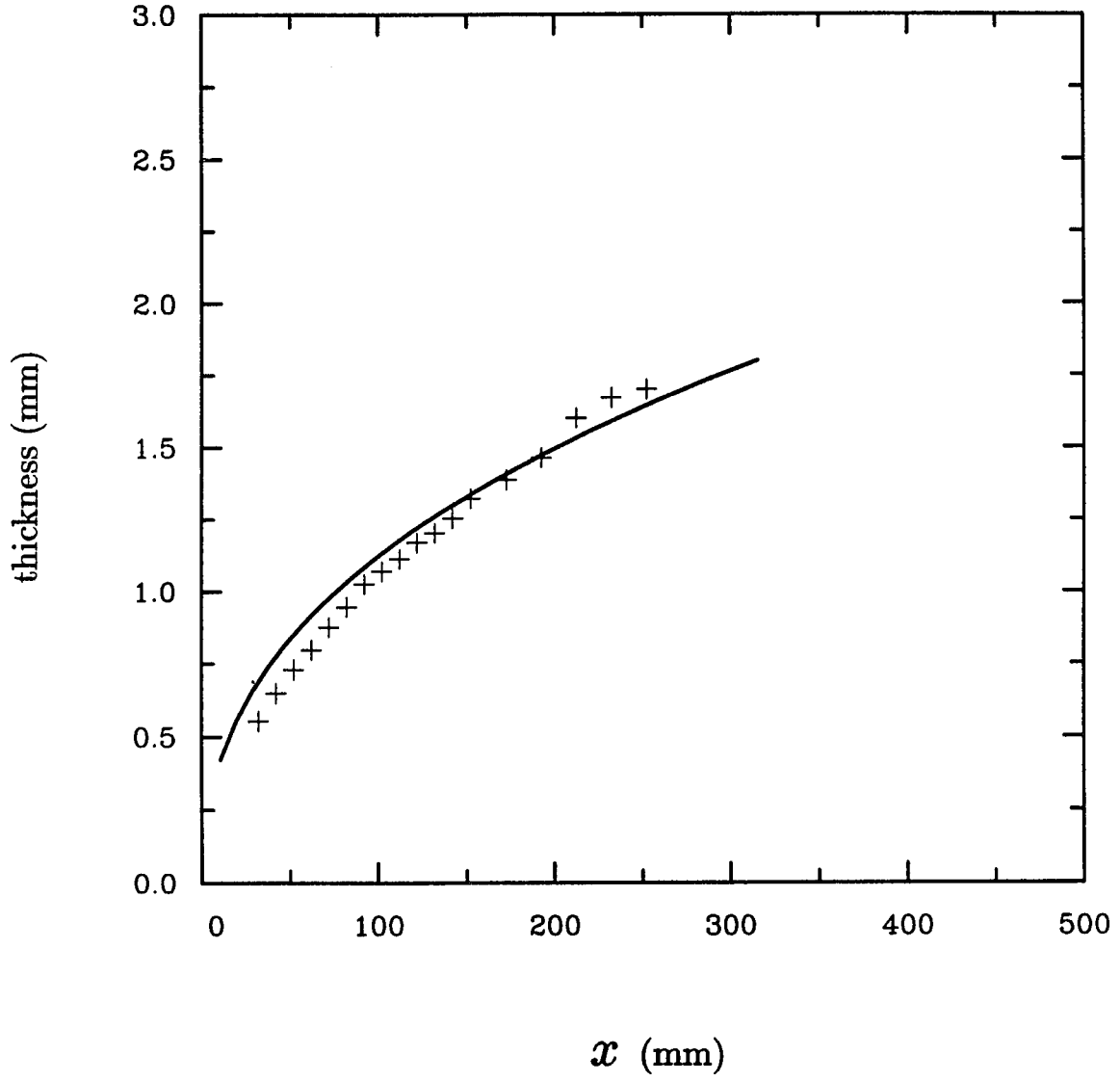

Figure 5.4: Sediment layer thickness profile for $\phi_s = 6.5$ % and $\theta = 35°$. —— theory; + - experimental points.

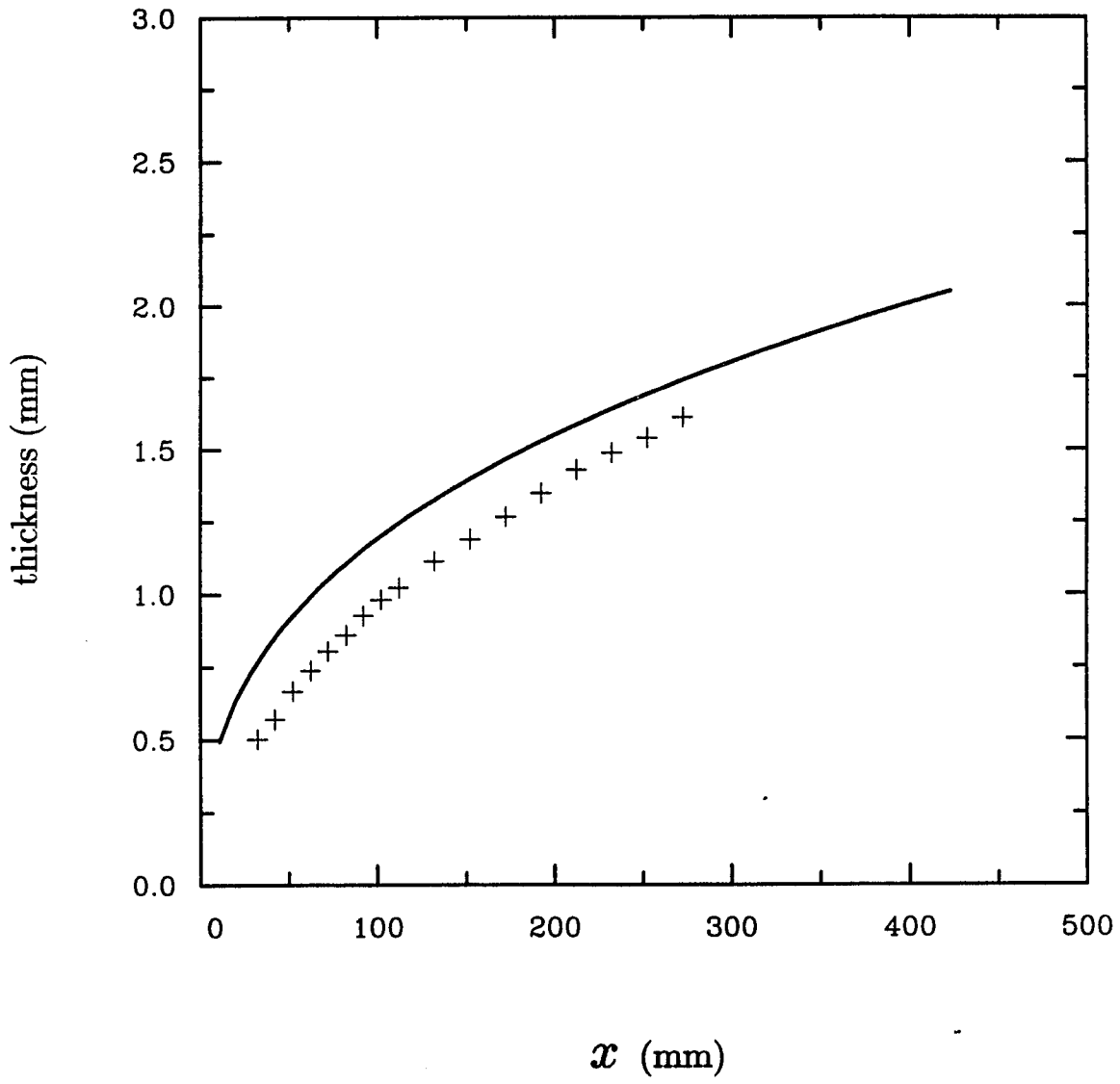

Figure 5.5: Sediment layer thickness profile for $\phi_s = 14.0\%$ and $\theta = 45°$. —— theory; + - experimental points.

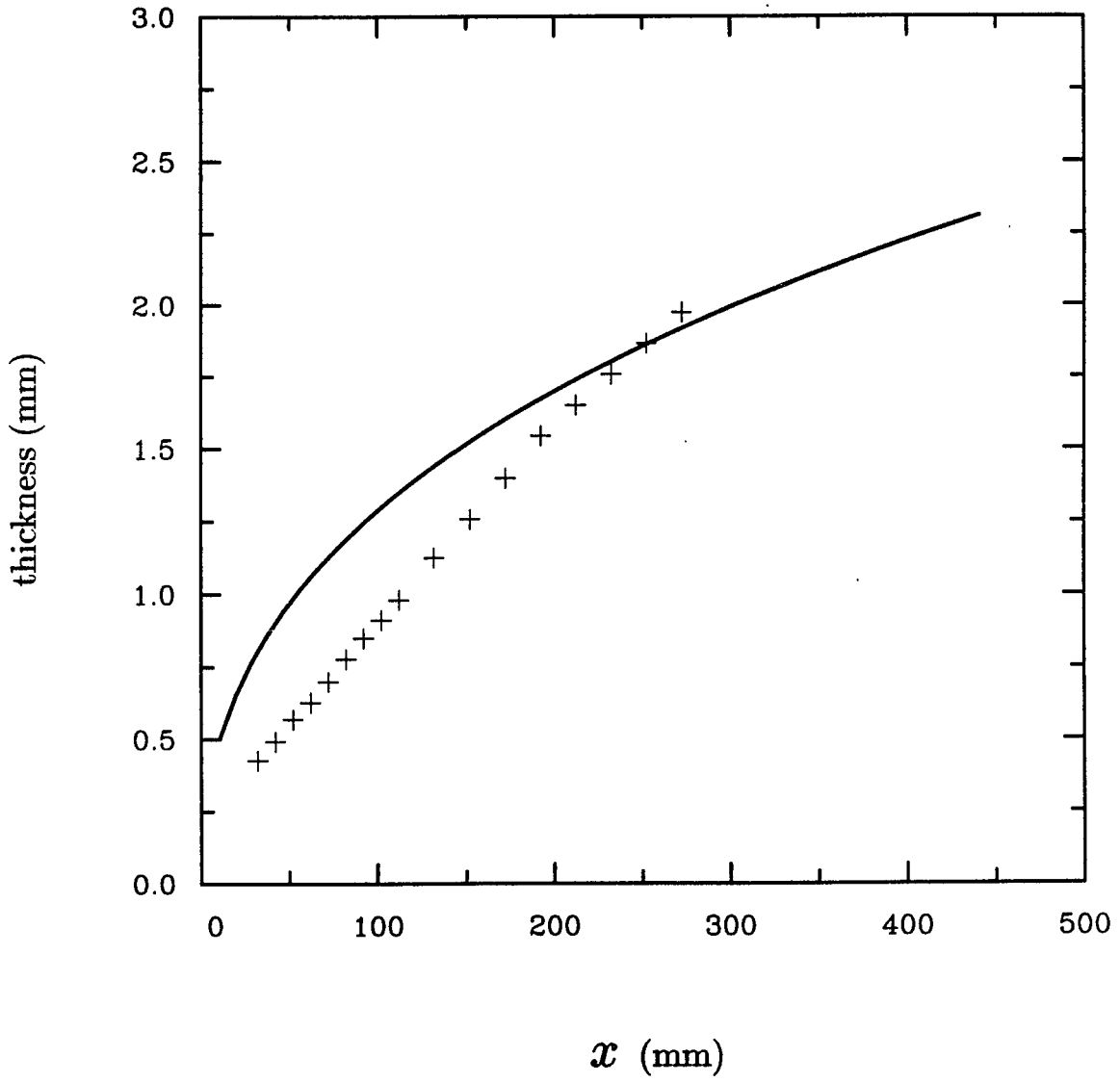

Figure 5.6: Sediment layer thickness profile for $\phi_s = 14.0$ % and $\theta = 35^o$. —— theory; + - experimental points.

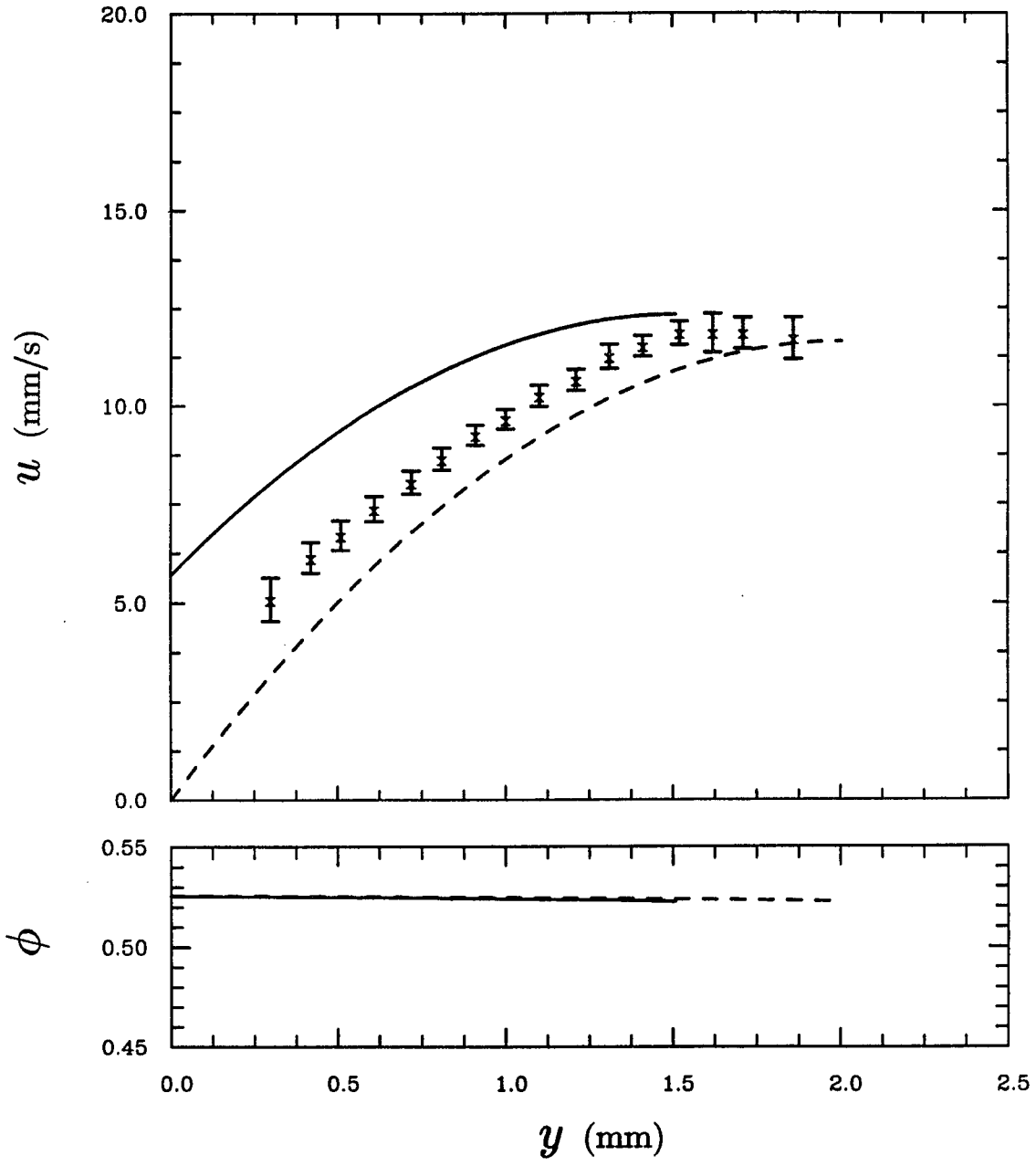

Figure 5.7: Experimentally measured and theoretically predicted velocity profiles within a sediment layer and calculated particle concentration profiles at x=204 mm, for ϕ_*=6.5% and $\theta = 35°$. Solid curve —— theory with slip; dashed curve – – – theory without slip.

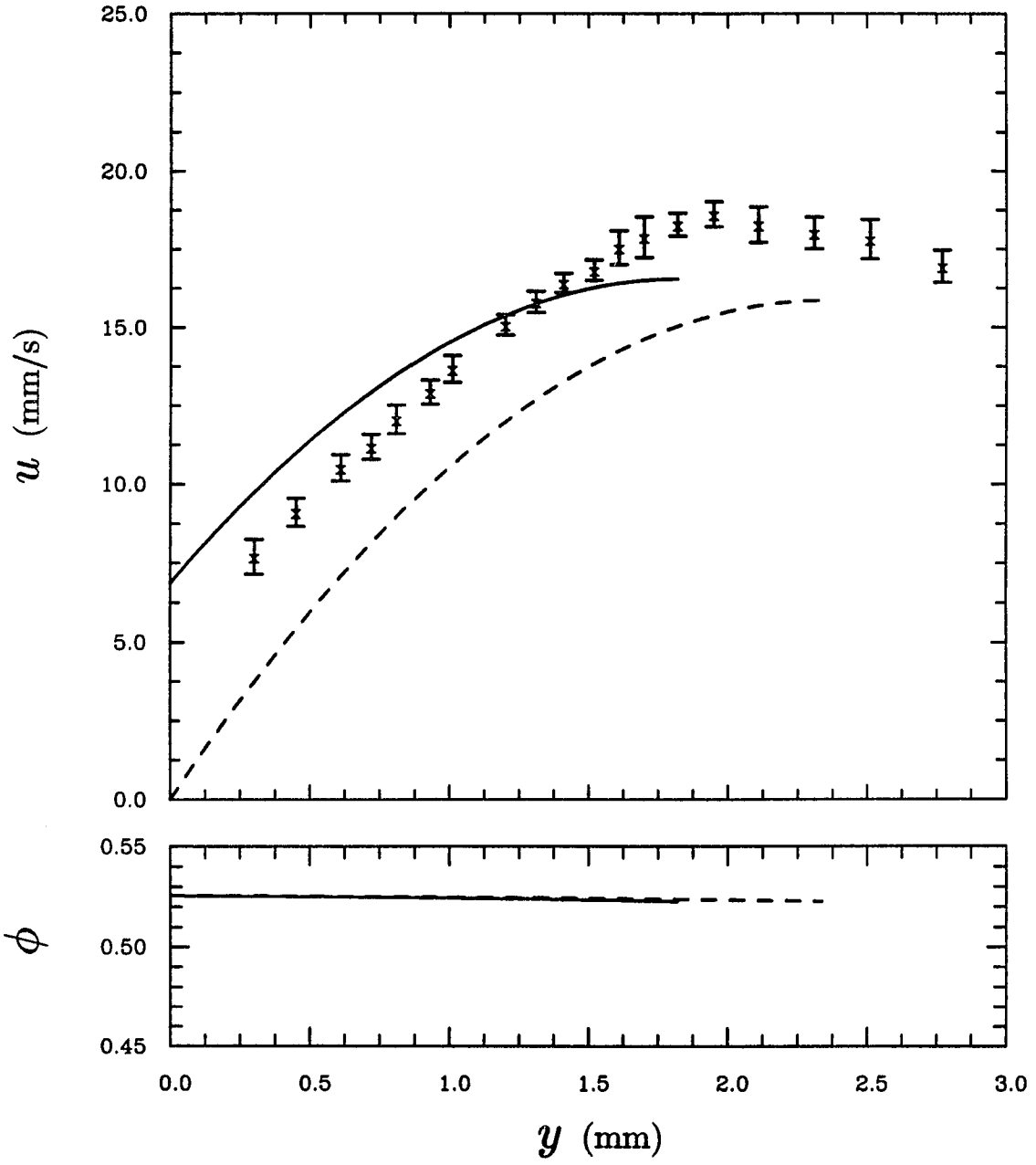

Figure 5.8: Experimentally measured and theoretically predicted velocity profiles within a sediment layer and calculated particle concentration profiles at x=324 mm, for ϕ_s=6.5% and $\theta = 35°$. Solid curve —— theory with slip; dashed curve – – – theory without slip.

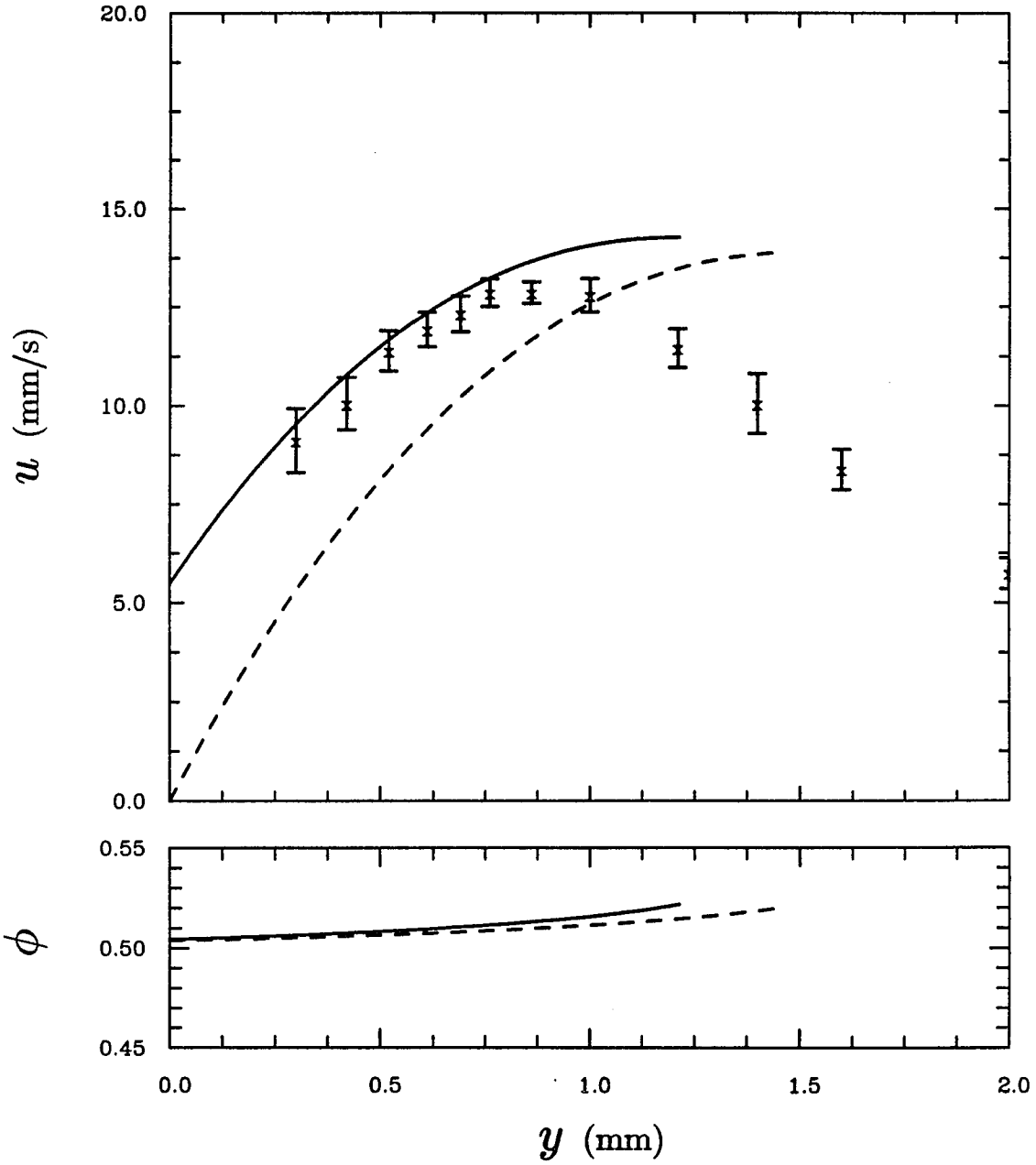

Figure 5.9: Experimentally measured and theoretically predicted velocity profiles within a sediment layer and calculated particle concentration profiles at x=214 mm, for ϕ_*=6.5% and $\theta = 45°$. Solid curve —— theory with slip; dashed curve – – – theory without slip.

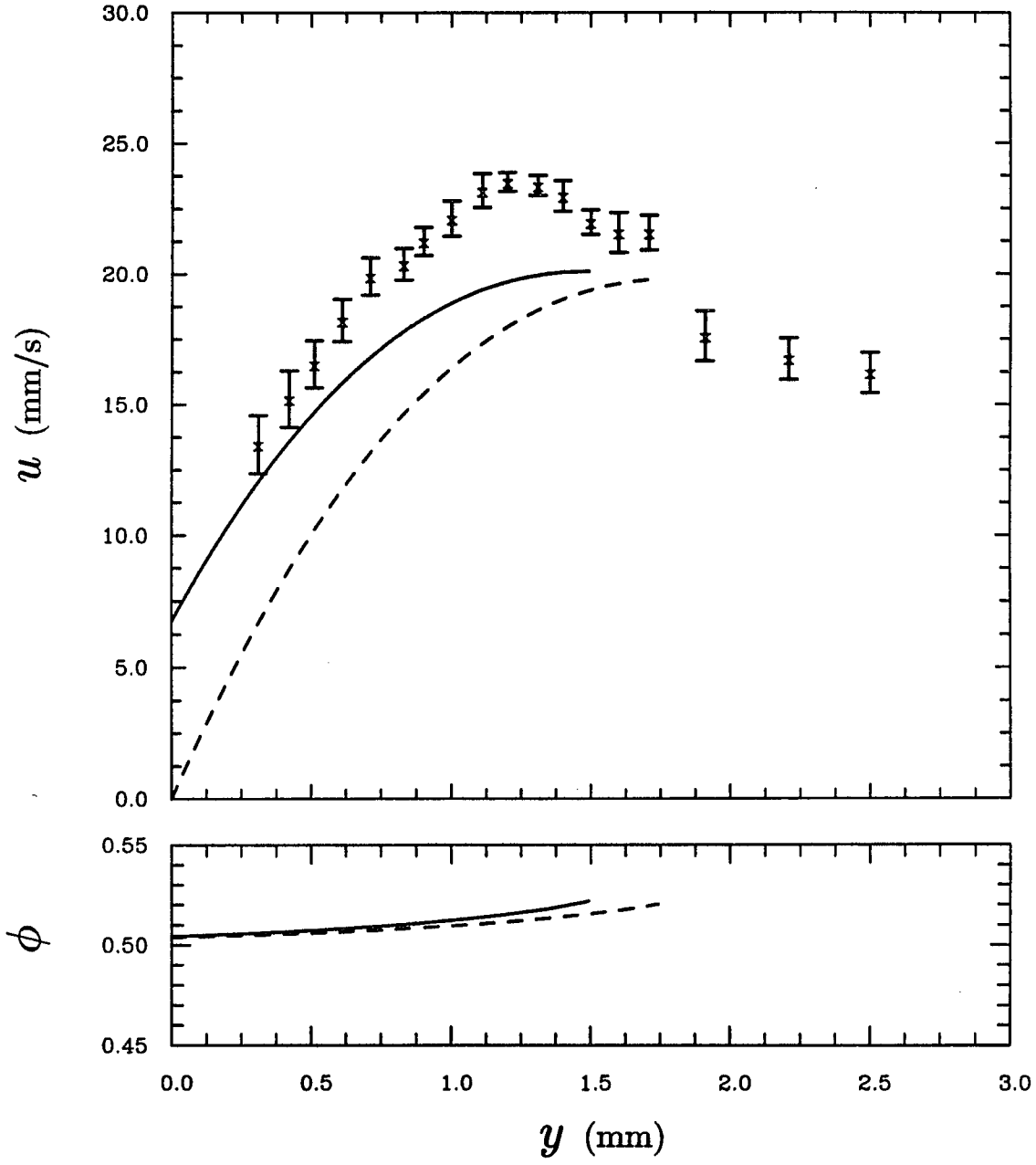

Figure 5.10: Experimentally measured and theoretically predicted velocity profiles within a sediment layer and calculated particle concentration profiles at x=364 mm, for ϕ_s=6.5% and $\theta = 45°$. Solid curve —— theory with slip; dashed curve – – – theory without slip.

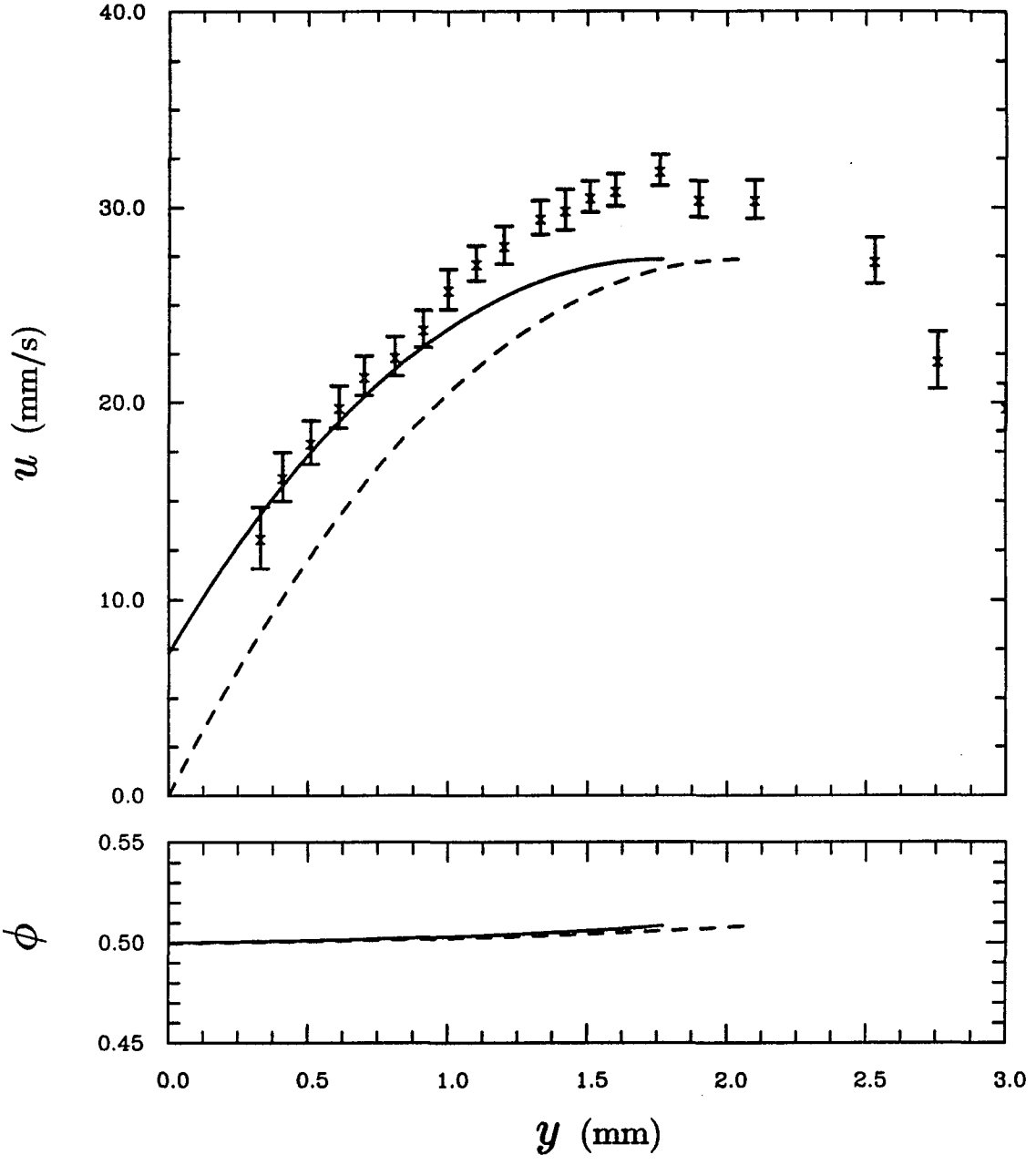

Figure 5.11: Experimentally measured and theoretically predicted velocity profiles within a sediment layer and calculated particle concentration profiles at x=404 mm, for ϕ_s=9.6% and $\theta = 45°$. Solid curve —— theory with slip; dashed curve – – – theory without slip.

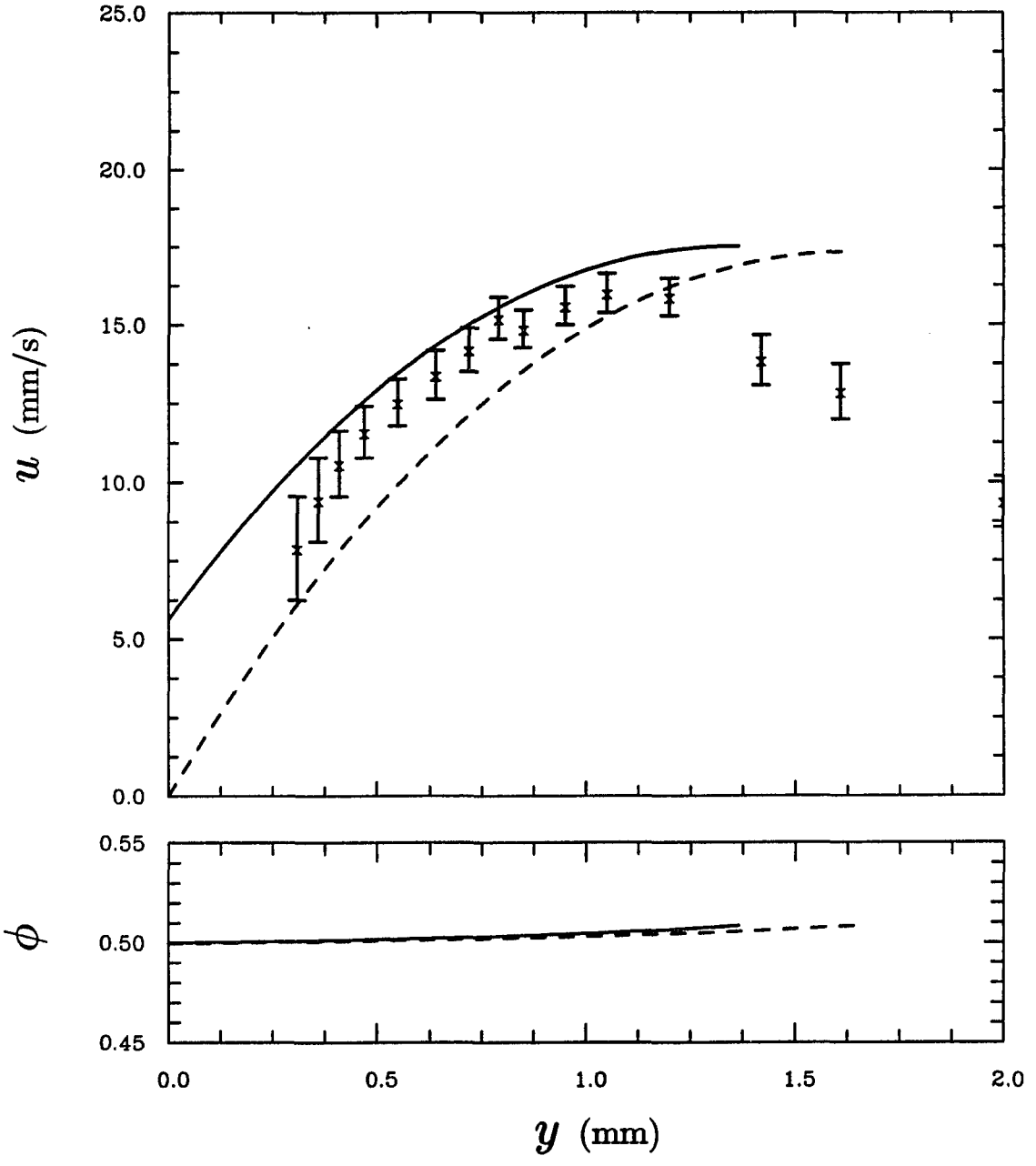

Figure 5.12: Experimentally measured and theoretically predicted velocity profiles within a sediment layer and calculated particle concentration profiles at x=204 mm, for ϕ_s=9.6% and $\theta = 45°$. Solid curve —— theory with slip; dashed curve – – – theory without slip.

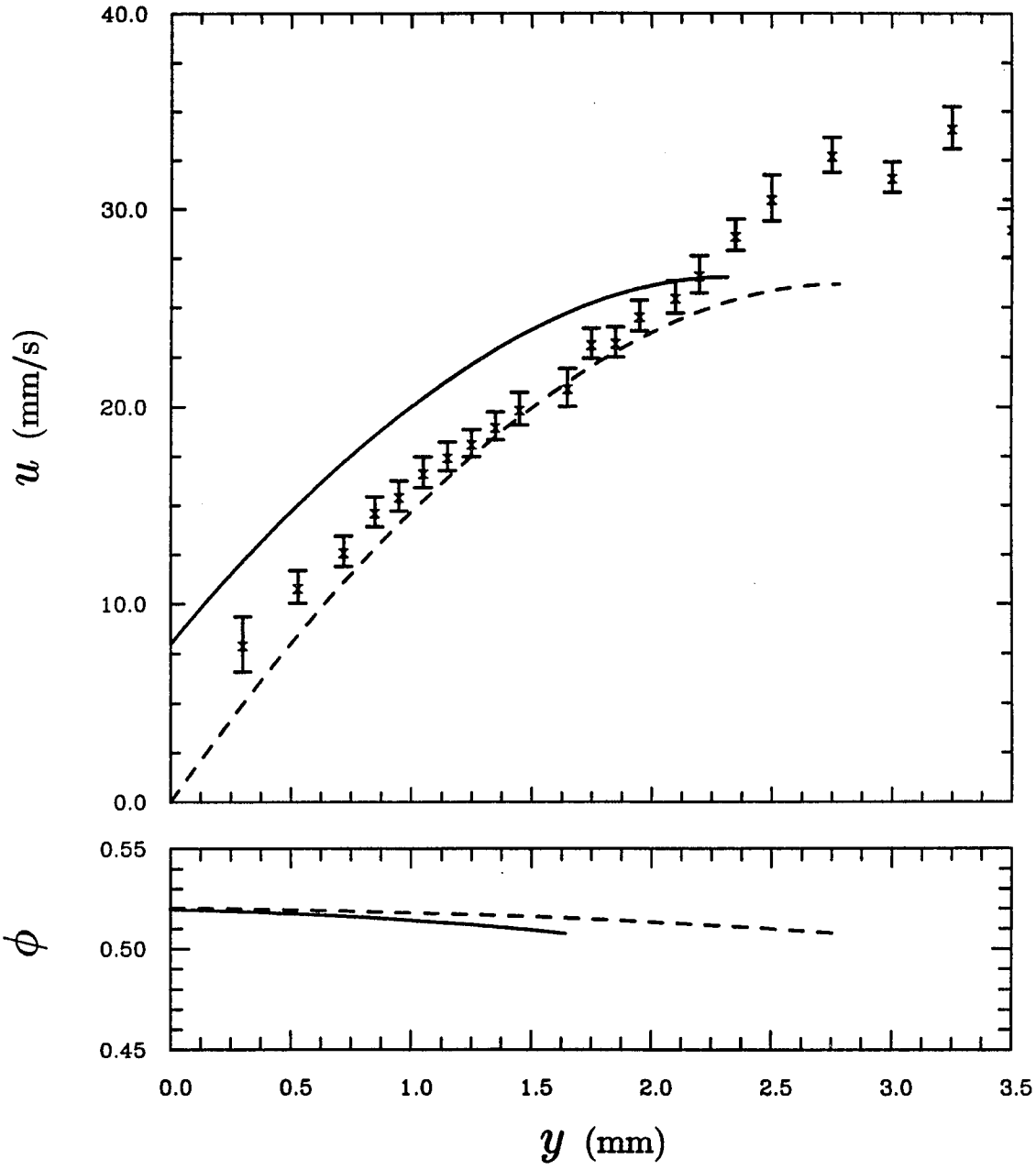

Figure 5.13: Experimentally measured and theoretically predicted velocity profiles within a sediment layer and calculated particle concentration profiles at x=444 mm, for ϕ_s=9.6% and $\theta = 35°$. Solid curve —— theory with slip; dashed curve – – – theory without slip.

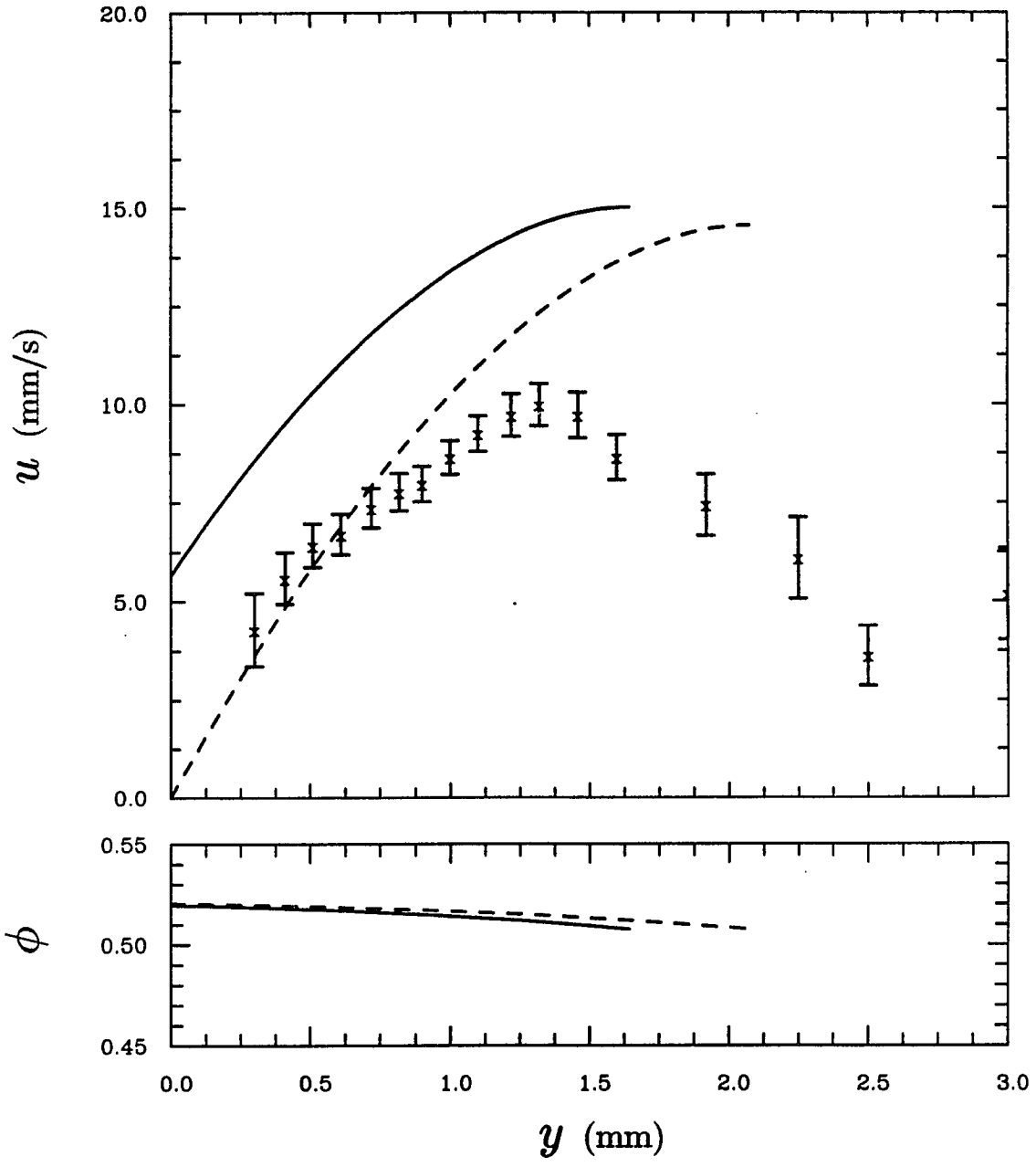

Figure 5.14: Experimentally measured and theoretically predicted velocity profiles within a sediment layer and calculated particle concentration profiles at x=184 mm, for ϕ_s=9.6% and $\theta = 35°$. Solid curve —— theory with slip; dashed curve – – – theory without slip.

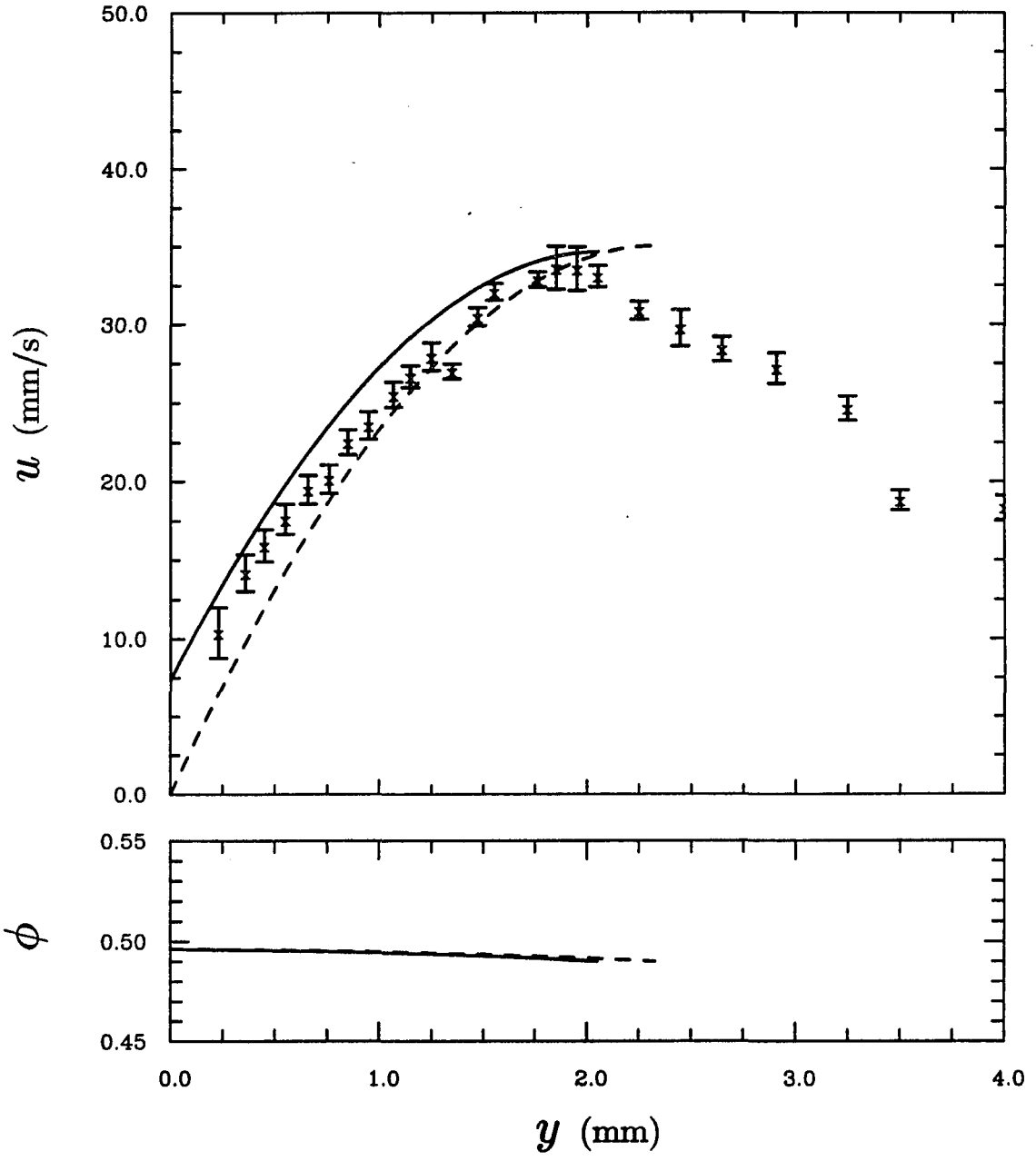

Figure 5.15: Experimentally measured and theoretically predicted velocity profiles within a sediment layer and calculated particle concentration profiles at x=424 mm, for ϕ_*=14.0% and $\theta = 45°$. Solid curve —— theory with slip; dashed curve – – – theory without slip.

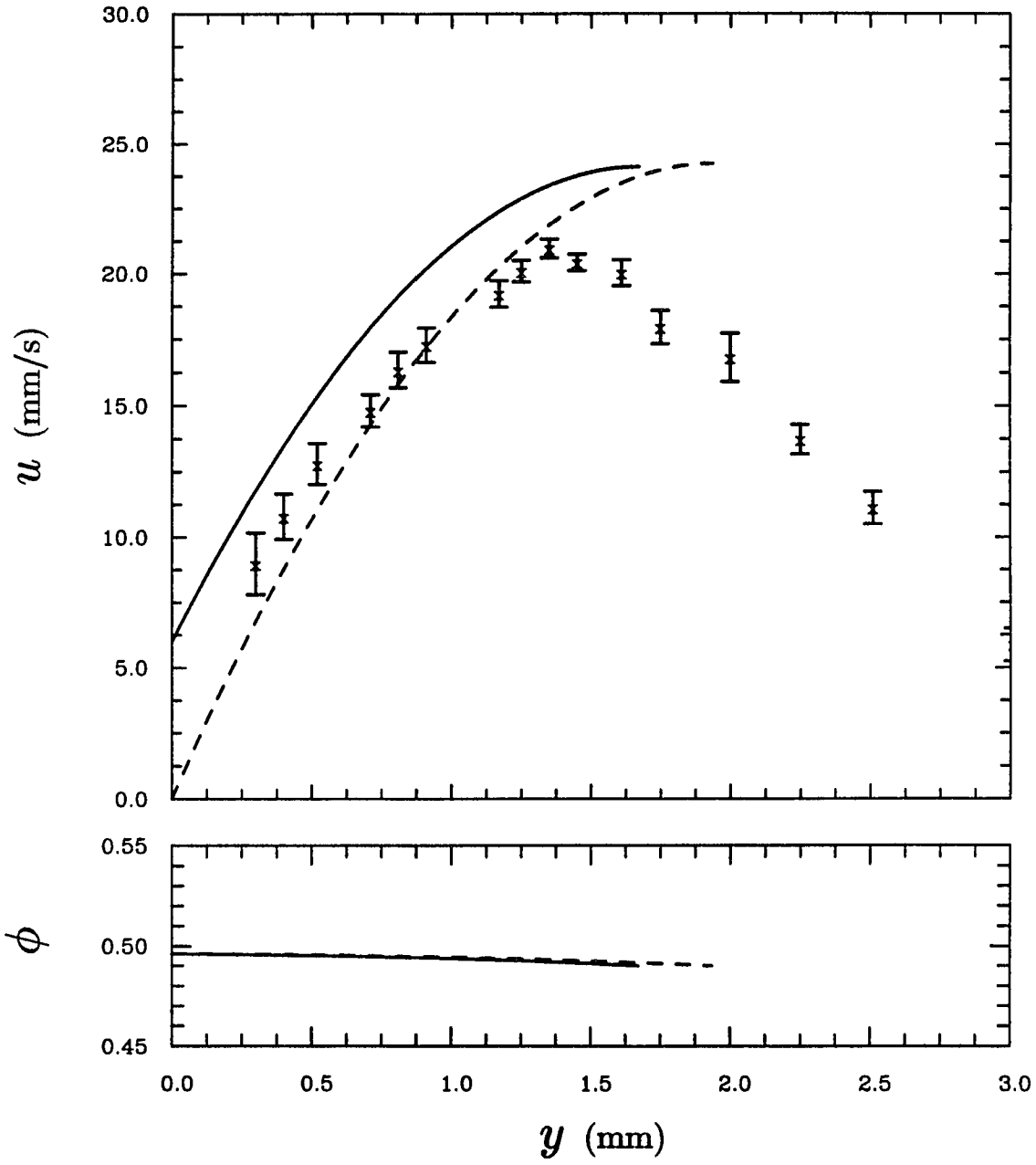

Figure 5.16: Experimentally measured and theoretically predicted velocity profiles within a sediment layer and calculated particle concentration profiles at x=244 mm, for ϕ_*=14.0% and $\theta = 45°$. Solid curve —— theory with slip; dashed curve – – – theory without slip.

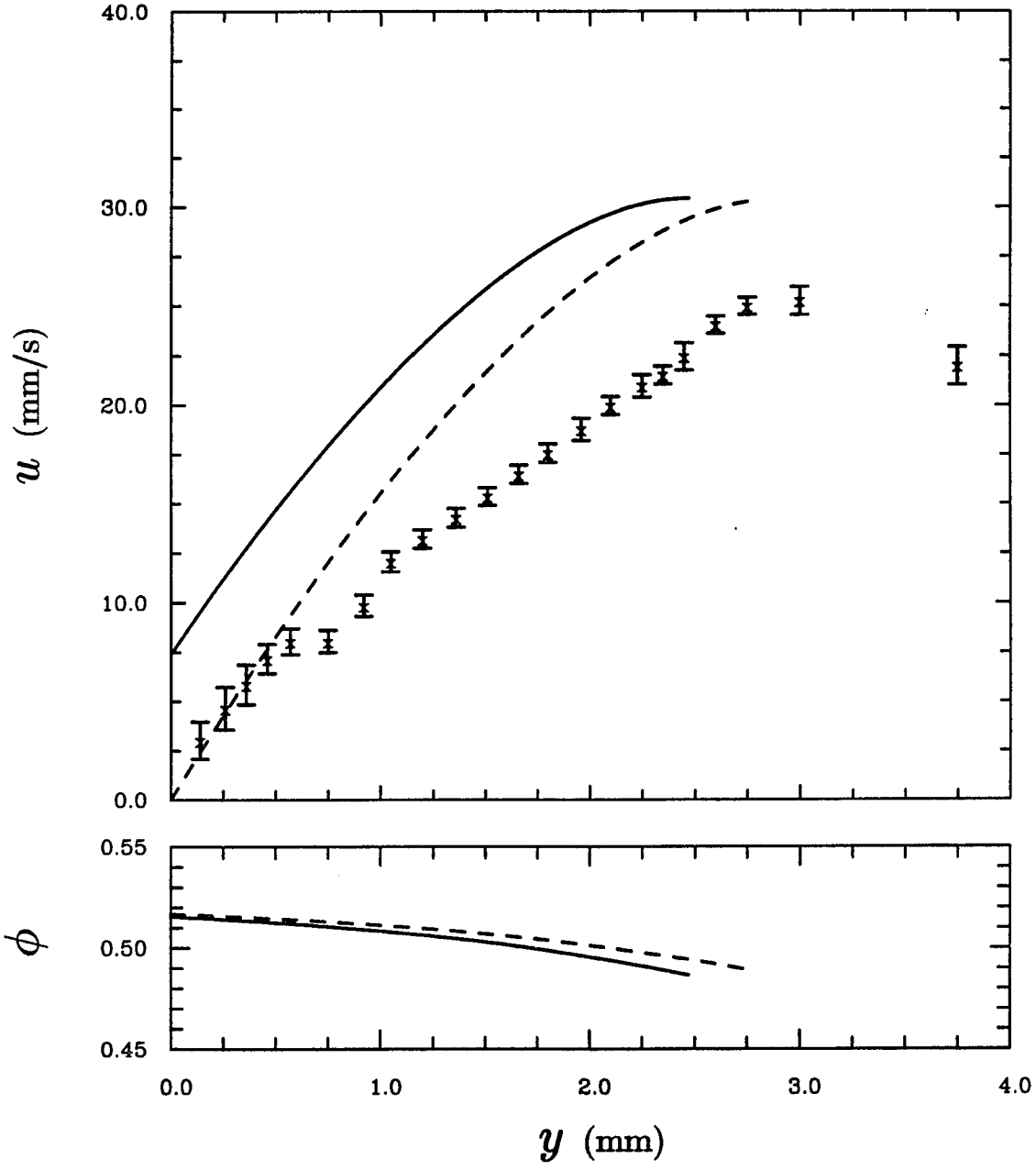

Figure 5.17: Experimentally measured and theoretically predicted velocity profiles within a sediment layer and calculated particle concentration profiles at x=384 mm, for ϕ_s=14.0% and $\theta = 35^o$. Solid curve —— theory with slip; dashed curve – – – theory without slip.

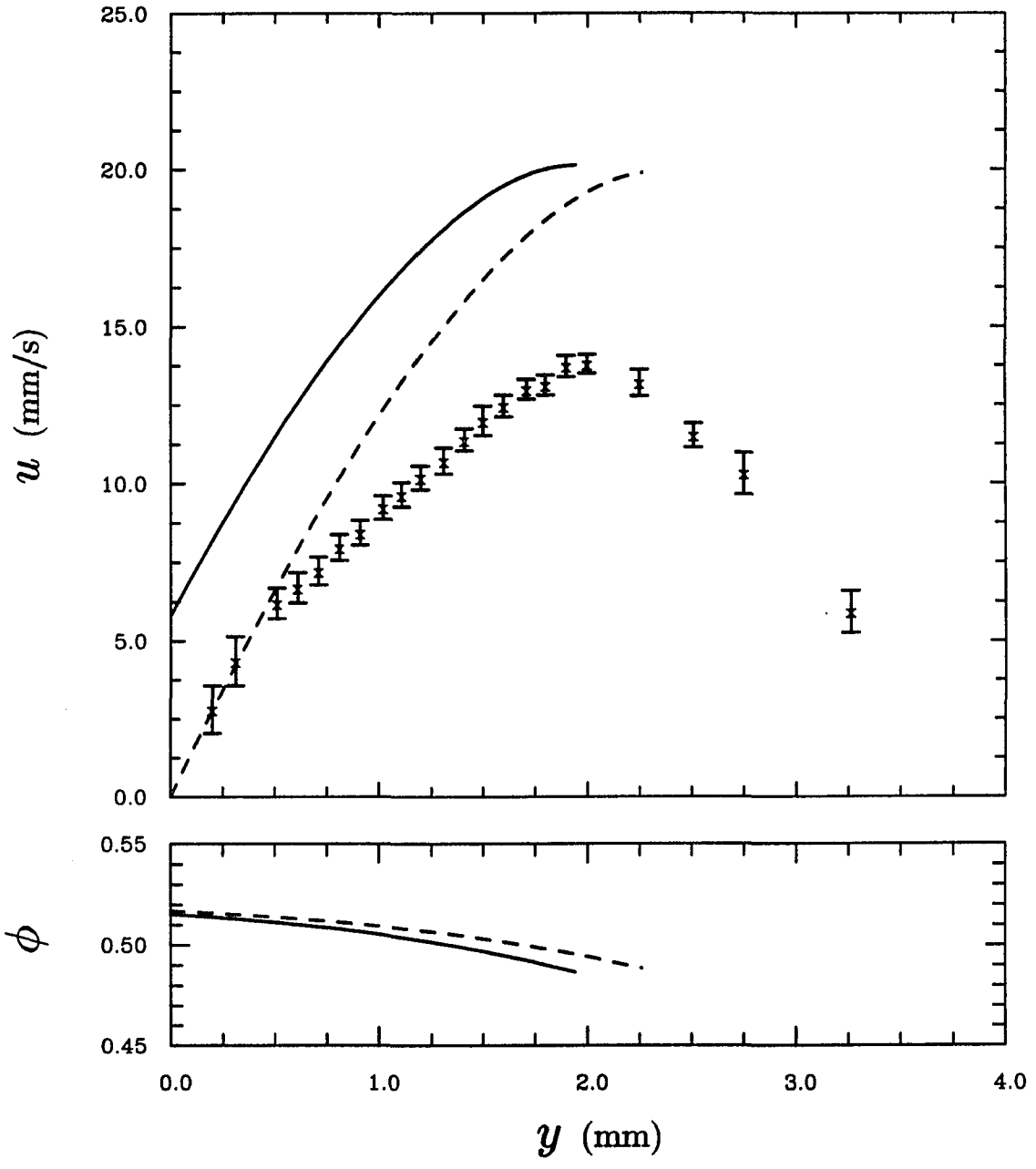

Figure 5.18: Experimentally measured and theoretically predicted velocity profiles within a sediment layer and calculated particle concentration profiles at x=204 mm, for ϕ_*=14.0% and $\theta = 35°$. Solid curve —— theory with slip; dashed curve – – – theory without slip.

Chapter 6

Conclusions and Recommondations for Future Work

This section briefly summarizes the findings of this work and, also identifies, the areas which remain for future study. In this study, we examined the flow of highly concentrated sediment layer encountered in a low aspect ratio inclined settlers by means of theoretical as well as experimental tools.

As discussed in chapters 2 & 3, in our theoretical work we have modified the model of Nir and Acrivos (1990) by introducing the effect of partial slip at the wall and also by including the effect of particle migration due to shear stress gradient. The latter was accomplished by introducing an additional term in the particle balance equation, while the former was achieved by replacing the no-slip boundary condition at the inclined plate with the one involving the effective slip velocity proportional to the local shear rate. The approximate form of this constant of proportionality was then obtained using an effective continuum method proposed by Chang and Acrivos (1982) and, was shown to be a function of the effective viscosity of the suspension

at the plate thereby indicating a large slip velocity for the suspensions containing large volume fraction of particles. As was shown in appendix A, this form of the slip coefficient was then correlated with experiments for particles volume fractions close to 50%.

Furthermore, the modified set of governing equations along with the boundary conditions were shown to follow a leading edge similarity solution with sediment layer thickness growing as $X^{1/2}$. In contrast, the similarity solution proposed by Nir & Acrivos (1990) was shown to describe a large X asymptotic solution. Thus, far down stream the thickness of the sediment layer was shown to scale as $X^{1/3}$. As discussed in chapter 2, introduction of slip as well as diffusion due to shear stress gradient significantly affect the predictions at low values of the sedimenting suspension concentration ϕ_s, as well as at high angles of inclinations. More specifically, unlike the predictions of Nir and Acrivos (1990), the sediment layer thickness was now found to vanish as $\phi_s \rightarrow 0$. In order to have a meaningful comparison with the experiments, the solution for the entire range of X was also constructed by integrating the governing equations using a finite difference scheme, in which the integration was started at some small X where the leading edge solution provided the appropriate initial condition. At far down stream, this solution was then shown to follow a large X asymptotic solution, which was obtained by replacing the partial slip boundary condition at the wall to a one with no-slip.

The theoretical predictions based on this effective continuum model which, although approximate, captures most of the qualitative as well as quantitative features of the flowing sediment layer. In addition, it also shows the applicability of this model far beyond the range for which the various diffusion coefficients were estimated. Finally, for future work, it provides a basis to study the flowing sediment layer in physically similar but industrially more relevant problem of high aspect ratio settlers in which, the interaction of flowing sediment layer with the clear fluid layer at the

downward facing surface may pose a more stringent condition on the steady state operation of these settlers.

In the course of our experimental study of flowing sediment layer, we have demonstrated the applicability of the well known LDA technique to measure the particle velocity in highly concentrated suspensions in which the refractive indices of the fluid and the particles were closely matched. As discussed earlier, the adaptation of LDA to concentrated suspensions is severly restricted owing to the problems encountered due to the optical turbidity and therefore, depends strongly on the fluid-particle system chosen and the traversing length of the beams inside the suspension. In addition, a small amount of mismatch in the refractive indices of fluid and particles give rise to a scattering in the velocity measurements, which in turn make the determination of the actual particle velocity fluctuations extremely difficult. In our measurements, however, we found these scatterings to be reasonably small except in the region adjacent to the inclined plate where the combined effect of small particle velocity and excessive reflections from the wall contributed to large scattering in the measured velocity signals. We also note that the measurement of the particle concentration using this technique requires a careful study of the effect of the optical turbidity arising due to the slight mismatch in the refractive indices on the Doppler bursts. More specifically, the one to one correspondence between the particles crossing the measuring volume and the signals received at the PM tube need to be established. One possible approach would be to mark a small fraction of particles and selectively process the signals received from them. Clearly, this technique depends strongly on the way particles are tagged. A common method used by some investigators in the past (Hookham, 1986) was to dye these particles with a fluorescent dye and identify the signals from these particles by means of an optical filter. Due to the week and incoherent nature of these fluorescent signals, however, this method failed to provide any meaningful concentration measurements. In contrast, we suggest here to employ

this technique with some reflecting particles and, use the Phase Doppler Anemometer along with the LDA to identify the scattering signals produced by these marked particles. This method, obviously, has an advantage as the strong signals produced by the reflecting particles would be easy to process. In addition, it would also yield the size of the particles crossing the measuring volume, thereby eliminating the error in the measurement of concentration due to polydispersity.

Appendix A

Estimation of the Slip Coefficient

The effects of an apparent wall slip in the flow behavior of suspensions and polymeric solutions has received much attention in the recent past by a number of researchers (Cohen & Metzner 1985; Yoshimura & Prud'homme 1988; Yilmazer & Kalyon 1989), particularly in the field of viscometry, where it often leads to a misinterpretation of the experimental data. Most of these investigators inferred this velocity slip by performing more than one viscometric measurement on different size systems having the same geometry, reminiscent of the classic analysis of Mooney (1931). Here, in contrast, the slip coefficient was determined by measuring the particle velocity profile in a suspension being sheared in a narrow-gap Couette device, using a technique described earlier in chapter three.

Consider then the Couette geometry consisting of an inner cup of radius $\tilde{R}_1(= 7.575cm)$ and a stationary outer cup of radius $\tilde{R}_2(= 8.214cm)$, as shown in figure A.1. For a Newtonian fluid in the absence of slip, the velocity decreases linearly across the gap with a slope equal to the applied shear rate $\dot{\gamma}_a$ given by

$$\dot{\gamma}_a = \frac{\tilde{R}_1\tilde{\Omega}}{(\tilde{R}_2 - \tilde{R}_1)} \tag{A.1}$$

On the other hand, when the fluid velocity differs from that at an adjacent surface by an amount equal to $\tilde{u}_s$, the corresponding shear rate within the gap is, in lieu of

(A.1)

$$\dot{\gamma}_s = \frac{\tilde{R}_1\tilde{\Omega} - 2\tilde{u}_s}{(\tilde{R}_2 - \tilde{R}_1)} \tag{A.2}$$

Therefore, in view of the definition of the slip coefficient $\hat{\zeta}$ for a suspension c.f. (2.19) & (3.5),

$$\tilde{u}_s \equiv \tilde{a}\hat{\zeta}\dot{\gamma}_s \tag{A.3}$$

it follows that

$$\hat{\zeta}(\phi) = \frac{(\dot{\gamma}_a - \dot{\gamma}_s)}{2\tilde{a}\dot{\gamma}_s(\tilde{R}_2 - \tilde{R}_1)} \tag{A.4}$$

It should be noted that the expression given above presupposes that the particle concentration profile remains uniform along the radial direction at steady state, which requires that the shear stress be constant across the gap. This condition is of course satisfied in a narrow-gap Couette device.

Ideally, it would be desirable to use in such experiments a suspension of neutrally buoyant particles since the particle concentration ϕ would then be uniform everywhere at steady state and equal to ϕ_i, the well mixed suspension added initially. Since our technique for measuring particle velocities required, however, that the refractive indices of the particles and of the fluid be closely matched, it proved almost impossible to find another combination of particles and fluid which, in addition, had equal densities. Hence the experiments were performed in a sedimenting suspension consisting of the same particles ($\rho = 1.18gm/cm^3$) used earlier for the inclined plate experiment and in a mixture of silicone fluids ($\rho = 1.05\ gm/cm^3$, $\mu = 86cp$ and $RI = 1.491@23^oC$). As will be seen presently, however, the interpretation of the experimental results requires knowledge of the vertical particle concentration profile $\phi(z)$.

In a recent paper, Acrivos *et al* (1993) studied the shear induced resuspension of heavy particles in a Couette device and showed that the ϕ profile along the axial direction in this geometry at steady state is governed by the particle balance

equation

$$\tilde{N}_g + \tilde{D}_{||}\frac{d\phi}{d\tilde{z}} = 0 \tag{A.5}$$

where $\tilde{N}_g$ represents the gravitational flux of particles while the second term on the left refers to the dimensional shear induced diffusive flux in the direction normal to the plane of shear (Leighton and Acrivos, 1987b). The above equation can be easily integrated, subject to the condition

$$\tilde{h}_o\phi_m = \int_0^{\tilde{h}} \phi d\tilde{z} \tag{A.6}$$

where $\tilde{h}_o$ & ϕ_m denote the height and the concentration of the settled layer of particles in absence of shear and $\tilde{h}$ represents the height of the resuspended layer at steady state. Thus, the solution of equations (A.5) and (A.6) yields the ϕ profile within the resuspended layer $0 \leq z \leq \tilde{h}$, which was used to determine the concentration, ϕ, at the axial location where the particle velocity measurements were made before computing the slip coefficient as a function of ϕ from (A.4).

The experimental procedure began by loading the gap with a well mixed suspension of known quantity and concentration. This initial concentration was kept close to 50% in order to avoid the appearance of a clear fluid layer at the top of the gap, which would have complicated the analysis by rendering $\tilde{h}$ unknown, and to ensure a fairly uniform concentration along the axial direction. The suspension was then sheared until steady state was reached. The velocity profile at this applied shear rate was then measured at several z-locations and the corresponding slip coefficients were calculated using (A.4). The particle concentrations at these values of z were then computed by solving equations (A.5) and (A.6), as done by Acrivos *et al.* (1993).

Figure A.2 depicts a typical particle velocity profile within the gap for $\phi =$ 50%, which, as seen, is clearly linear over most of the domain with the solid line giving the best straight line fit. Most of the slip coefficient measurements performed during the course of this study were limited to concentrations close to or less than 50%,

primarily because, at higher concentrations the slip coefficient was found to show a strong dependence on the magnitude of applied shear rate. This can be clearly seen in figures A.3 and A.4, in which the experimentally estimated slip coefficients are plotted with respect to the shear rate for 50% and 53.5% concentrations respectively. Finally, shown in figure A.5 is the slip coefficient as a function of the particle volume fraction. In this figure, the data point at a 53.5% concentration was measured at a shear rate of $4s^{-1}$. The solid line in this figure represents the curve $(\lambda(\phi)/6)$, which tends to fit the experimental data well provide ϕ is below 51%.

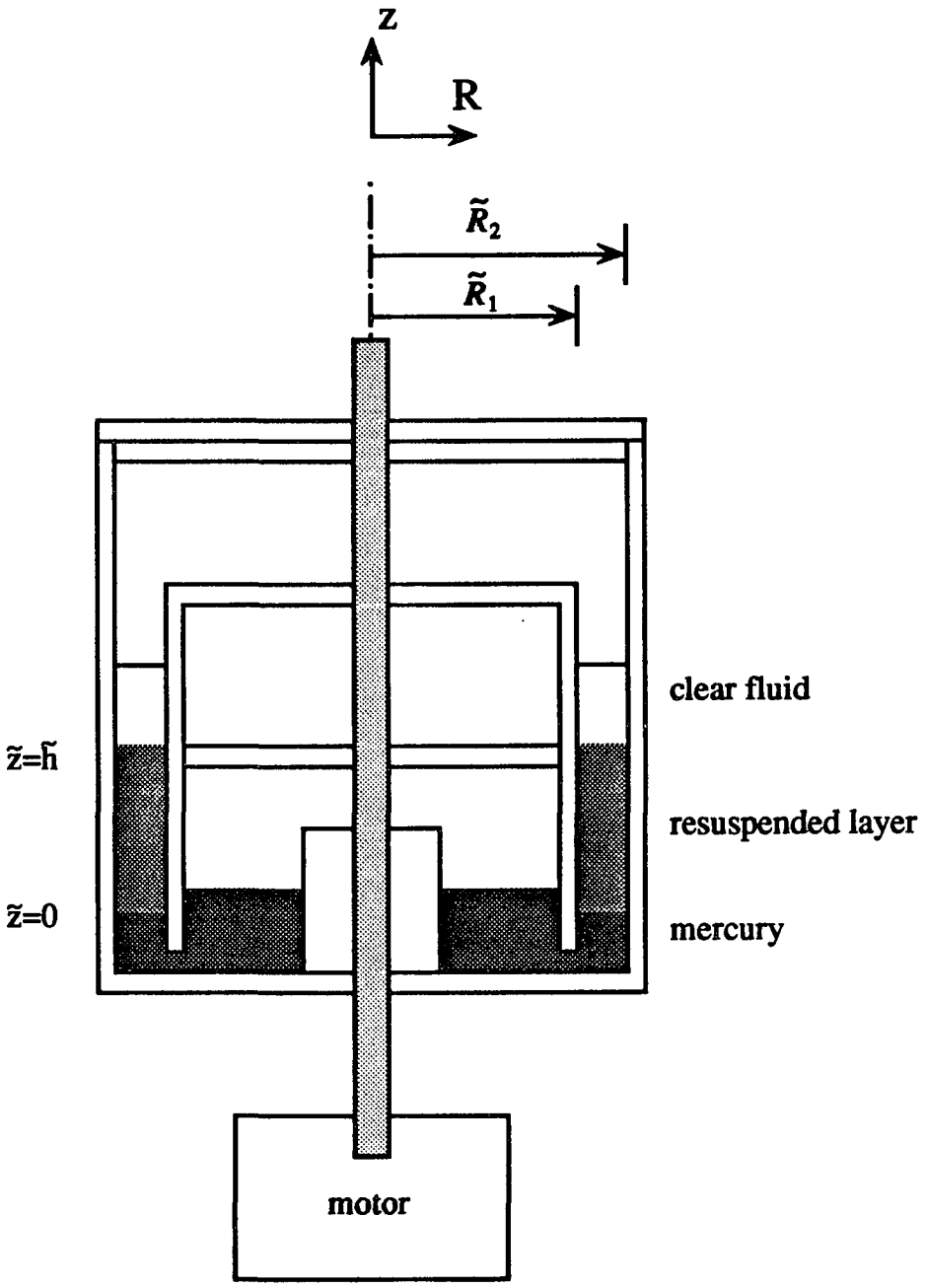

Figure A.1: A schematic description of the Couette device used.

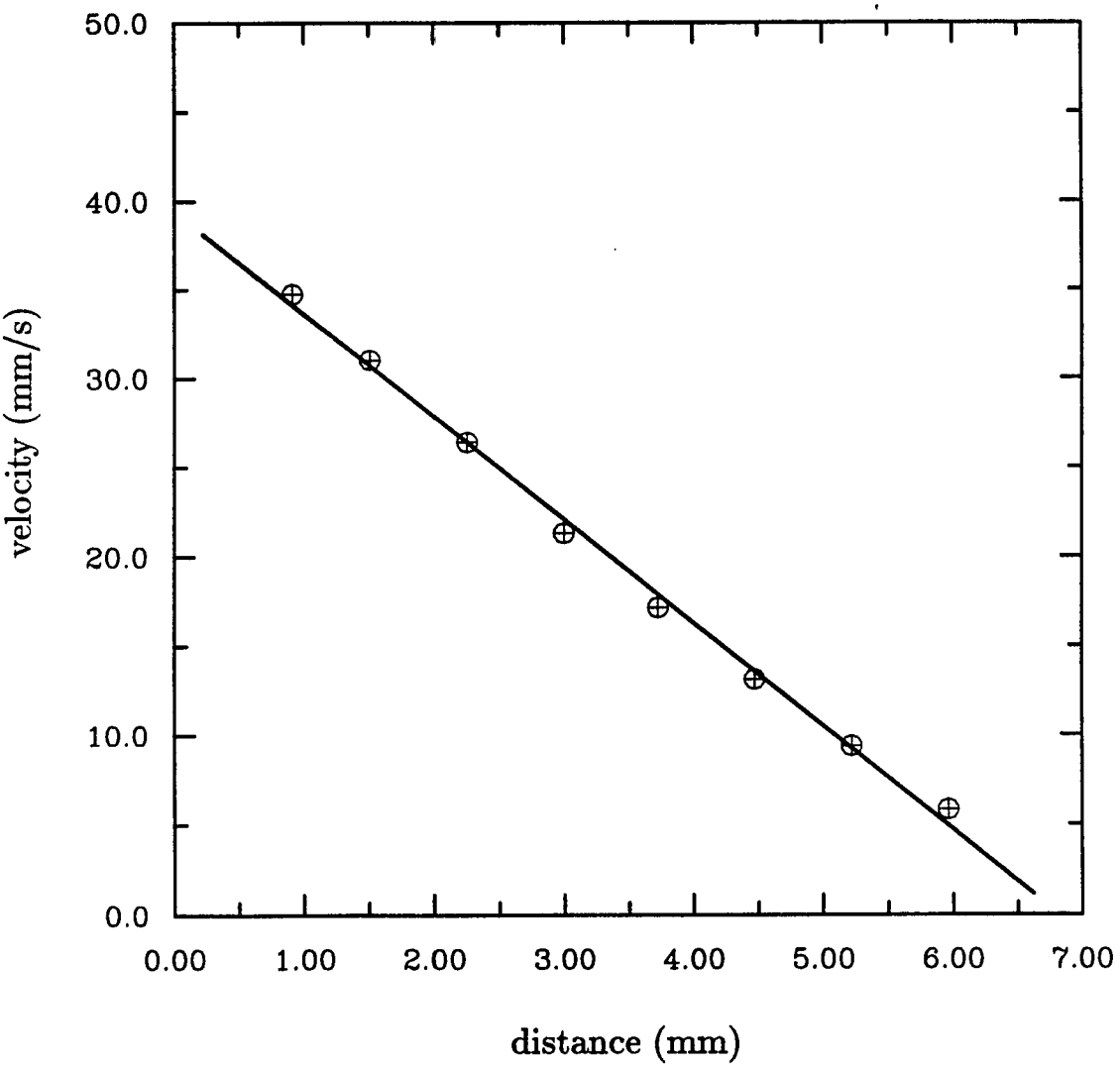

Figure A.2: The measured velocity profile within the gap, at an applied shear rate of $6.36s^{-1}$ and with $\phi = 50.5\%$. The solid line represents the best straight line fit.

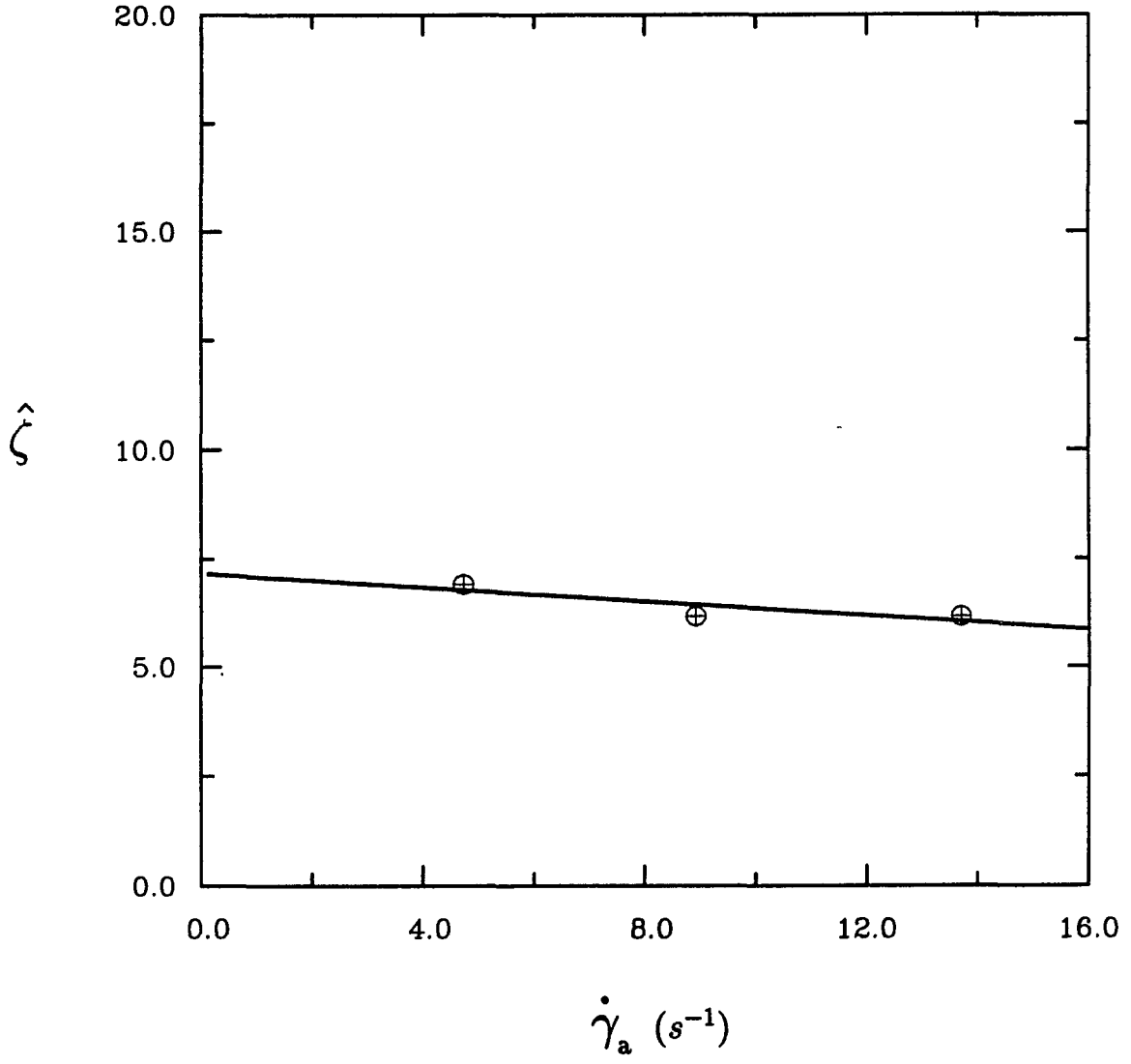

Figure A.3: The slip coefficient as a function of the shear rate for $\phi = 50\%$.

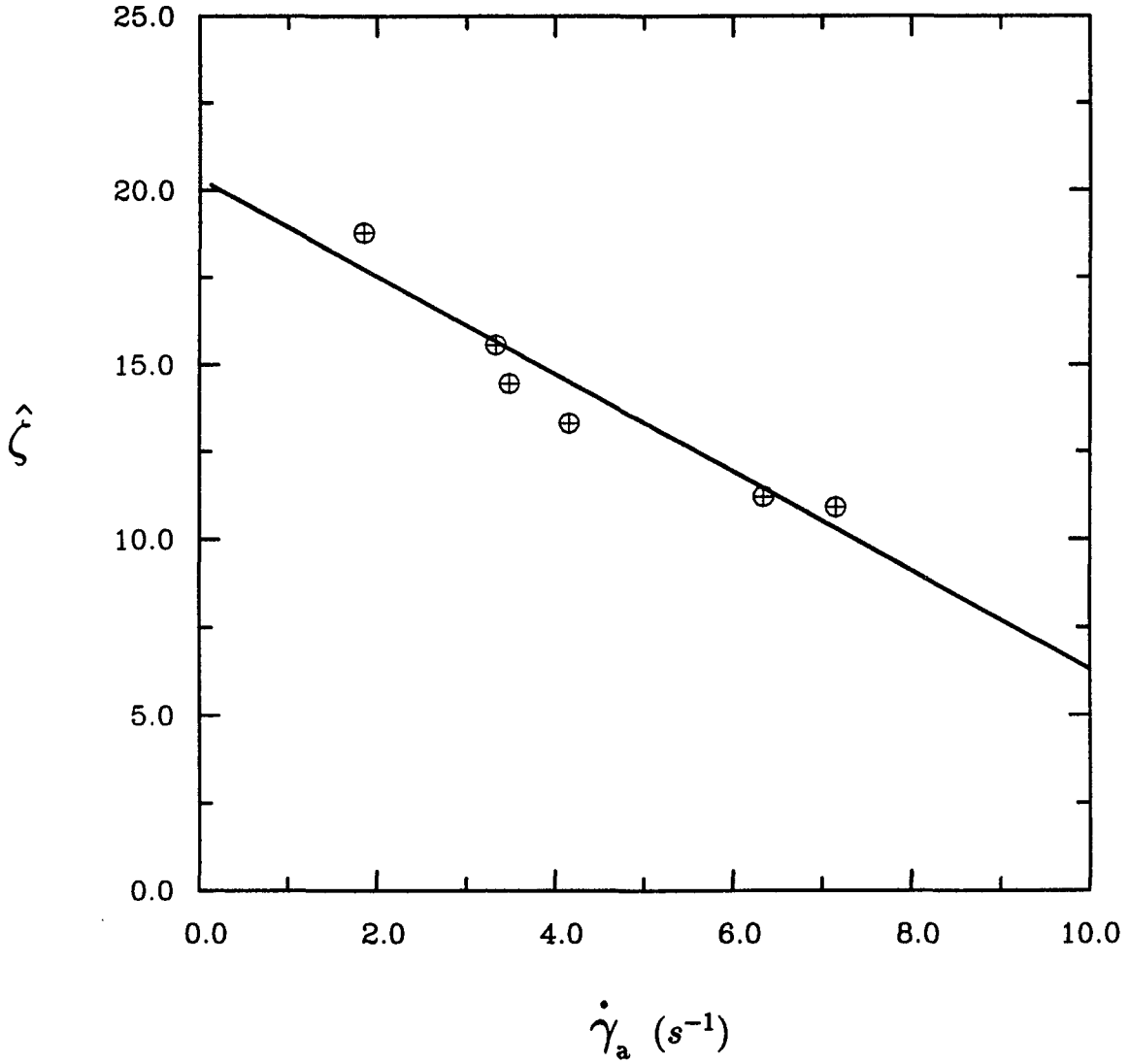

Figure A.4: The slip coefficient as a function of the shear rate for $\phi = 53.5\%$.

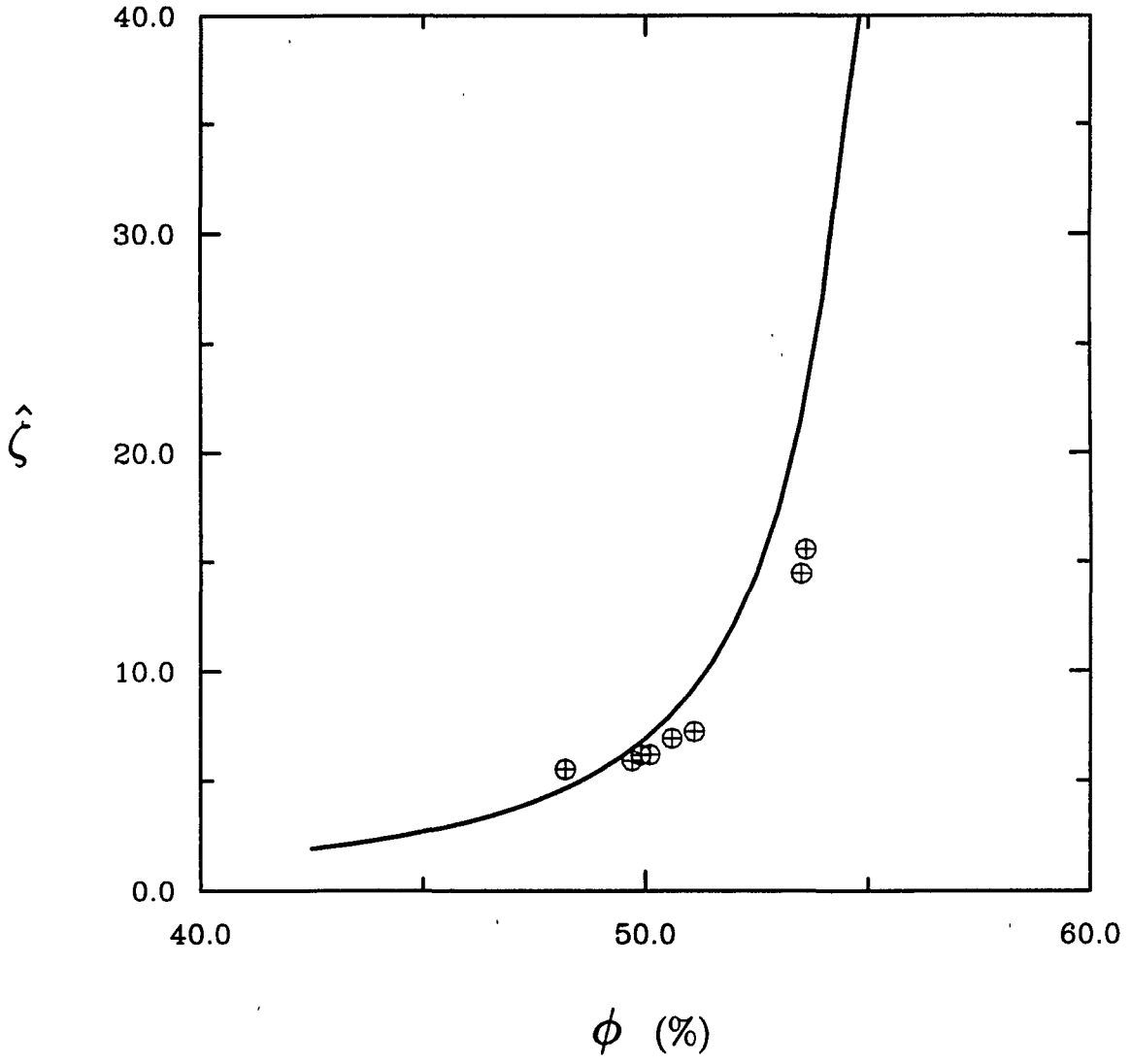

Figure A.5: The slip coefficient as a function of ϕ, for a shear rate $\sim 4s^{-1}$. The solid line represents the function $\lambda(\phi)/6$.

References

Acrivos, A. & Chang, E. 1986 A model for estimating transport quantities in two-phase materials. *Phys. Fluids* **29**, 3-4.

Acrivos, A. & Herbolzheimer, E. 1979 Enhanced sedimentation in settling tanks with inclined walls. *J. Fluid Mech.* **92**, 435-457.

Acrivos, A., Mauri, R. & Fan, X. 1993 Shear induced resuspension in Couette device. *To appear in Int. J. Multiphase Flow.*

Benenati, R. F. & Brosilow, C. B. 1962 Void fraction distribution in beds of spheres. *A. I. Ch. E. J.* **8**, 359-361.

Borhan, A. 1989 An experimental study of the effect of suspension concentration on the stability and efficiency of the inclined settlers. *Phys. Fluids A* **1**, 108-123.

Brady, J. F. & Bossis, G. 1988 Stokesian dynamics. *Ann. Rev. Fluid Mech.* **20**, 111-157.

Chang, E. Y. & Acrivos, A. 1987 Conduction of heat from a planar wall with uniform surface temerature to a monodisperse suspension of spheres. *J. Appl. Phys.* **62**, 771-776.

Cohen, Y. & Metzner, A. B. 1985 Apparent slip flow of polymer solutions. *J. Rheol.*, **29**, 67-102.

Durlofsky, L. J. & Brady, J. F. 1989 Dynamic simulation of bounded suspensions of hydrodynamically interacting paticles. *J. Fluid Mech.* **200**, 39-67.

Henderson, D. & Smith, W. R. 1978 Exact analytical formulas for the distribution functions of charged hard spheres in the mean spherical approximation. *J. Stat. Phys.* **19**, 191-200.

Herbolzheimer, E. 1983 Stability of the flow during sedimentation in inclined channels. *Phys. Fluids* **26**, 2043.

Herbolzheimer, E. & Acrivos, A. 1981 Enhanced sedimentation in narrow tilted channels. *J. Fluid Mech.* **108**, 485-499.

Hill, W. D., Rothfus, R. R. & Li, K. 1977 Boundary enhanced sedimentation due to settling convection. *Int. J. Multiphase Flow* **3**, 561-583.

Hookham, P. A. 1986 Velocity and concentration measurements in suspension flowing in a rectangular channel. *Ph.D Dissertation*, California Inst. of Tech.

Karnis, A., Goldsmith, H. L. & Mason, S. G. 1966 The Kinetics of Flowing Dispersions: I. Concentrated Suspensions. *J. Colloid Sci.,* **22**, 531-553.

Koh, C. J. 1991 Experimental and Theoretical Studies on Two Phase Flows. *Ph.D Dissertation*, California Inst. of Tech.

Koh, C. J., Hookham, P. & Leal, L. G. 1994 Submitted to *J. Fluid Mech.*.

Kowalewski, T. A. 1980 Velocity profiles of suspensions flowing through a tube. *Arch. Mech.,* **32**, 857-865.

Lebowitz, J. L. 1964 *Phys. Rev.* **133**, A895.

Leighton, D. & Acrivos, A. 1986 Viscous resuspension. *Chem. Eng. Sci.* **41**, 1377-1384.

Leighton, D. & Acrivos, A. 1987 Measurement of shear-induced self-diffusion in concentrated suspensions of spheres. *J. Fluid Mech.* **177**, 109-131.

Leighton, D. & Acrivos, A. 1987 The shear-induced migration of particles in concentrated suspensions. *J. Fluid Mech.* **181**, 415-439.

Leung, W. F. & Probstein, R. F. 1983 Lamella and tube settlers 1. Model and operation. *Ind. Engng Chem. Proc. Des. Rev.* **22**, 58-67.

McMahon, T. A. & Parker, R. R. 1975 Particles in tube flow at moderate Reynolds number. *Trans. Soc. Rheol.,* **19**, 445.

Mooney, M. 1931 Explicit formulas for slip and fluidity. *J. Rheol.,* **2**, 210-222.

Nakamura, N. & Kuroda, K. 1937 La cause de l'acceleration de la vitesse de sedimentation des suspensions dans les recipients inclines. *Keijo J. Med.* **8**, 256-296.

Nir, A. & Acrivos, A. 1990 Sedimentation and sediment flow on inclined surfaces. *J. Fluid Mech.* **212**, 139-153.

Nouri, J. M., Whitelaw, J. H. & Yianneskis, M. 1987 Particle motion and turbulence in dense two-phase flows. *Int. J. Multiphase Flow* **13**, 729-739.

Phillips, R. J., Armstrong, R. C. & Brown, R. A. 1992 A constitutive equation for concentrated suspensions that accounts for shear-induced particle migration. *Phys. Fluids A* **4**, 30-40.

Ponder, E. 1925 On sedimentation and rouleaux formations -I. *Q. J. Expt'l Physiol.* **15**, 235-252.

Probstein, R. F., Yung, R. & Hicks, R. 1981 In *Physical Separations* (ed. M. P. Freeman & J. A. Fitzpatrick, New York : Engineering Foundation), pp. 53-92.

Rubinstein, I. 1980 A steady laminar flow of a suspension in a channel. *Int. J. Multiphase Flow.* **6**, 473-490.

Schneider, W. 1982 Kinematic-wave theory of sedimentation beneath inclined walls. *J. Fluid Mech.* **120**, 323-346.

Shaqfeh, E. S. G. & Acrivos, A. 1986 The effect of inertia on the buoyancy driven convection flow in settling vessels having inclined walls. *Phys. Fluids* **29**, 3935-3948.

Shaqfeh, E. S. G. & Acrivos, A. 1987 The effects of inertia on the stability of the convective flow in inclined particle settlers. *Phys. Fluids* **30**, 960-973.

Yilmazer, U. & Kalyon, D. M. 1989 Slip effects in capillary and parallel disk torsional flows of highly filled suspensions. *J. Rheol.,* **33**, 1197-1212.

Yoshimura, A. & Prud'homme, R. K. 1988 Wall slip corrections for Couette and parallel disk viscometers. *J. Rheol.,* **32**, 53-67.

Zhang, K., Acrivos, A. & Schaflinger, U. 1992 Stability in a two dimensional Ha gen-Poiseuille resuspension flow. *Int. J. Multiphase Flow* **18**, 51.